Rochester Institute of Technology

RIT Digital Institutional Repository

Theses

12-7-2023

Demonstration of a Hybrid Electroabsorption Modulator/ Photovoltaic Device for Space-based Free Space Optical Communication and Power Generation

Emily Kessler-Lewis
esk7191@g.rit.edu

Follow this and additional works at: https://repository.rit.edu/theses

Recommended Citation

Kessler-Lewis, Emily, "Demonstration of a Hybrid Electroabsorption Modulator/Photovoltaic Device for Space-based Free Space Optical Communication and Power Generation" (2023). Thesis. Rochester Institute of Technology. Accessed from

This Dissertation is brought to you for free and open access by the RIT Libraries. For more information, please contact repository@rit.edu.

RIT

Demonstration of a Hybrid Electroabsorption Modulator/Photovoltaic Device for Space-based Free Space Optical Communication and Power Generation

by

Emily Kessler-Lewis

A dissertation submitted in partial fulfillment of the requirements
for the degree of Doctorate of Philosophy in Microsystems Engineering

Microsystems Engineering Program
Kate Gleason College of Engineering

Rochester Institute of Technology

Rochester, New York
December 7, 2023

Demonstration of a Hybrid Electroabsorption Modulator/Photovoltaic Device for Space-based Free Space Optical Communication and Power Generation

by

Emily Kessler-Lewis

Committee Approval:

We, the undersigned committee members, certify that we have advised and/or supervised the candidate on the work described in this dissertation. We further certify that we have reviewed the dissertation manuscript and approve it in partial fulfillment of the requirements of the degree of Doctorate of Philosophy in Microsystems Engineering.

Dr. Seth M. Hubbard — Date
Professor, Microsystems Engineering and Physics

Dr. Stephen J. Polly — Date
Research Scientist, NanoPower Research Laboratory

Dr. Raymond Hoheisel — Date
Owner, BlackSky Aerospace, LLC

Dr. Stefan Preble — Date
Professor, Microsystems Engineering and Electrical and Microelectronic Engineering

---

Dr. Michael S. Pierce — Date
Associate Professor, Physics

Certified by:

Dr. Stefan Preble — Date
Director, Microsystems Engineering Program

Thesis Release Permission Form

Rochester Institute of Technology
Kate Gleason College of Engineering

Title:

Demonstration of a Hybrid Electroabsorption Modulator/Photovoltaic Device for Space-based Free Space Optical Communication and Power Generation

I, Emily Kessler-Lewis, hereby grant permission to the Wallace Memorial Library to reproduce my thesis in whole or part.

Emily Kessler-Lewis — Date

Date — Date

ABSTRACT

Kate Gleason College of Engineering
Rochester Institute of Technology

Degree: Doctorate of Philosophy **Program:** Microsystems Engineering
Author's Name: Emily Kessler-Lewis
Advisor's Name: Dr. Seth M. Hubbard
Dissertation Title: Demonstration of a Hybrid Electroabsorption Modulator/Photovoltaic Device for Space-based Free Space Optical Communication and Power Generation

The emergence of proliferated low-Earth orbit (pLEO) constellations using small satellites has resulted in significant interest in lowering the size, weight, and power (SWaP) of mission critical subsystems. III-V semiconductors are the class of materials typically used for photovoltaic (PV) arrays for satellites due to their exceptional efficiencies of upwards of 35 % and ability to be made thin, flexible, and lightweight. This is contrasted with the high SWaP communication system, which utilizes a radio frequency (RF) transceiver in order to communicate with a ground station. A lower SWaP alternative to the RF transceiver is to transmit data using free space optical (FSO) communication. FSO communication at 1.55 µm is of particular interest due to the wavelength being inherently eye safe and existing infrastructure from the telecommunications industry. This research presents on a hybrid power generation/data communication device using III-V PV as the power generating component and an InP-based multiple quantum well (MQW) electroabsorption modulator (EAM) targeted for operation at 1.55 µm as the data communication component.

A MQW EAM utilizes the quantum confined Stark effect (QCSE) to shift the absorption coefficient of the material; using the QCSE amplitude modulation of a signal is possible over FSO communication. To be hybridized with a PV device, a surface normal EAM is required. While it

is advantageous to have a large area to aid pointing accuracy with FSO communication, the EAM suffers from decreased bandwidth due to area-dominated capacitive effects. These capacitive effects were extensively studied, and data rates ranging from 0.25 to 1 Mbps were demonstrated. Additionally, in order to accurately target device operation at 1.55 µm, the thickness of the InGaAs quantum well region and the InAlAs barriers were investigated through both simulation and experimental work.

Two device architectures were investigated; a four-terminal, mechanically bonded hybrid device and a three-terminal, monolithically integrated device. The four-terminal, mechanically bonded device allows growth of the PV device to be conducted on a GaAs substrate, enabling higher power conversion efficiencies compared to growth on InP. A dual junction InGaP/GaAs photovoltaic device with an AM0 power conversion efficiency of 23 % was mechanically bonded to an InP-based EAM in a 0.5 U form factor module. Using a segmented modulator design, a data rate for the module of 0.5 Mbps was demonstrated. The three-terminal device, all grown monolithically on InP, has the advantage of only requiring one growth and one fabrication. In addition, the monolithically integrated device further reduces the SWAP of the hybrid device by 50 % as only one substrate is required. This design required careful consideration of the shared contact layer between the PV device and EAM, needing to balance fractional power loss in the PV device and parasitic absorption of 1.55 µm light. A single junction InP PV device was grown a top of an InGaAs/InAlAs EAM, demonstrating simultaneous power generation and data transmission, and to our best knowledge demonstrated the first hybrid, monolithically integrated device to be successfully fabricated. These hybrid devices have applications that extend beyond satellites, such as unmanned aerial vehicles, orbital debris tagging, and implantable medical devices.

To my husband, James.

Acknowledgments

They say it takes a village - the support I have received from colleagues, friends, teammates, and family are what made this journey possible.

First and foremost I would like to acknowledge my advisor, Dr. Seth Hubbard. Between undergraduate internships and now through the conclusion of my academic career you have pushed me to become a better scientist and engineer, and for that I am forever grateful.

I would also like to acknowledge my other committee members. Dr. Steve Polly for being my first phone call when I decided I wanted to pursue this degree (and for always helping when it seems like the whole world is falling apart because Hall measurements on p-type InP are nebulous), Dr. Raymond Hoheisel for all of the technical discussions, support, and enthusiasm during this multi-year project, Dr. Stefan Preble for assistance with simulations, and Dr. Michael Pierce for valuable discussions.

I have been fortunate enough to have been able to work with some amazing colleagues over the years:

- Dr. Elisabeth McClure, for being my first NPRL friend back in 2015 who, over the next 8 years, became my closest confidant, favorite food explorer, and best friend. Thank you for always reminding me that there is a light at the end of the tunnel, and I'm looking forward to all of our adventures in the future!
- Dr. Julia D'Rozario for her enthusiasm about the work we get to do and for always being excited about fun research results.
- Dr. Anastasiia Fedorenko for the many lively discussions we had in our office.
- Dr. George Nelson for being my first mentor in III-V semiconductors, and for explaining what dark current is to me multiple times as an undergrad.
- Elijah Sacchitella for being an incredible intern, being my extra set of hands in the lab, and for all of your help (and sass) over the years. I am so excited to see what you do next!
- Brandon ”Record Breaking Solar Cells” Bogner, for help calibrating the QE system over and over again, the many coffee walks, the football games (Go Jets), the troubleshooting of both of our device problems, and so much more. Your friendship has been invaluable to me.

I would also like to acknowledge support from the staff from NPRL and Microsystems Engineering. Thank you Elaine Lewis and Lisa Zimmerman for administrative help. I would also like to thank Ross Hisert for always helping with tools in the lab, for helping fix them when they don't want to behave, and for assisting with some of my *fun* test setups. Many thanks to MOCVD Engineers Salwan Omar and Tony Mazur, who kept the reactor happy and running and for never letting me cut apples in the glovebox.

None of this work would have been possible without the help from the RIT NanoFab/SMFL, and I would like to acknowledge Tom Grimsley, John Nash, Rich Battaglia, Bruce Tolleson, and Sean O'Brien. Thank you all so much for the assistance with tools over the years, sorry for breaking some of them, and double sorry for yelling at the spin coaters so much.

RIT has been my home for the past decade, and I would like to acknowledge my undergraduate department of Microelectronic Engineering. Specifically, I would like to thank Dr. Robert Pearson, who welcomed me into the program back in 2013.

Friends and teammates outside of RIT helped remind me that there is, in fact, life outside of the lab. I would like to acknowledge my coach Steve Titus, who believed in my ability to balance both an academic and athletic career. I would also like to acknowledge my teammates of Team Western NY Weightlifting for enthusiastically asking about my research, and for the many check-ins over the years. I would also like to acknowledge my friend Claire Hannon, for helping me figure out what colors go together for figures and the mini-graphic design lessons (and for the many times that working in a coffee shop on this dissertation was absolutely the right move).

Penultimately, I would like to thank NASA for sponsoring the work in this dissertation through the Small Business Innovative Research Initiative.

And finally, I would like to acknowledge my husband, James Lewis, who this work is dedicated to. You have provided a space for me to pursue my goals. You have believed in me every single day, even when I didn't believe in myself. You always know when I need a coffee, a snack, or to be told be tough and get it together. Thank you for always making me feel safe, loved, and supported. I love you x ∞

Contents

Abstract . . . . **v**

List of Tables Captions . . . . **xiii**

List of Figures Captions . . . . **xiv**

1 Motivation **1**

1.1 Reduction of SWaP 1

1.2 Proposed Solution 4

1.3 Outline of Dissertation 5

2 Introduction **7**

2.1 Solar Cell Theory of Operation 7

2.2 III-V Photovoltaics 11

2.2.1 Multijunction Solar Cells 11

2.3 Free Space Optical Communication 13

2.4 Electroabsorption Modulators 17

2.4.1 Quantum Confined Stark Effect 18

2.4.2 EAM Figures of Merit 21

2.4.3 Surface Normal EAMs 22

2.5 Conclusion 23

3 Electroabsorption Modulator Development **25**

3.1 Material Selection and Epitaxial Design 25

3.1.1 EAM Quantum Well and Barrier Material Selection 25

3.1.2 Lateral Conduction Layer Design 28

3.2 EAM Growth and Fabrication 35

3.2.1 MOVPE Growth of EAMs 35

3.2.2 Fabrication of EAMs 38

3.3 Quantum Well Thickness Study 40

3.3.1 Lumerical Workflow 40
3.3.2 Simulated Well/Barrier Ratio Study 43
3.3.3 Experimental Well Thickness Study 47
3.3.4 Coupled Quantum Well Design 52
3.4 Bandwidth and Cutoff Frequency 55
3.5 Summary of Section 59

4 Mechanically Stacked Hybrid Device 62
4.1 Single Cell Integration 63
4.1.1 Growth and Fabrication of Single Cell Hybrid Device 63
4.1.2 Discrete Device Testing 65
4.1.3 Hybrid Device Bonding and Testing 70
4.1.4 Simultaneous Modulation and Power Generation . . 71
4.2 0.5 U Module Integration 72
4.2.1 Mask Design 74
4.2.2 Dual Junction Solar Cell Design 75
4.2.3 EAM Design 85
4.2.4 Device Bonding and Packaging 88
4.3 Summary of Section 92

5 Monolithically Integrated Device 95
5.1 Monolithic Design Advantages 95
5.2 InP Solar Cell Development 97
5.2.1 Fabrication Procedure 98
5.2.2 Front Surface Field Thickness Study 99
5.2.3 Emitter Thickness Study 101
5.3 Monolithic Device Mask Design 102
5.4 p-Common Contact Development 103
5.5 Monolithically Integrated Device Epitaxy and Fabrication 107
5.6 Discrete Junction Testing 111
5.6.1 InP PV Testing 111

5.6.2 EAM Testing . . . 114
5.7 Simultaneous Power Generation and Data Transmission Testing . . . 116
5.8 Summary of Section . . . 118

6 Conclusions . . . 120
6.1 Conclusions and Outlook . . . 120
6.1.1 EAM Development . . . 120
6.1.2 Mechanically Stacked Device . . . 122
6.1.3 Monolithically Integrated Device . . . 123
6.2 Accomplishments and Awards . . . 124
6.2.1 Awards . . . 124
6.2.2 Service . . . 124
6.3 Curriculum Vitae . . . 125

A Modulator Testing . . . 127
A.1 ON/OFF Ratio Testing . . . 127
A.2 Optical Cutoff Frequency Testing . . . 127

References . . . 130

List of Tables

2.1 Table of literature reported EAM figures of merit for operation at and around 1.55 μm.
NR = Not Reported
InGaAs = $In_{0.53}Ga_{0.47}As$
InAlAs = $In_{0.52}Al_{0.48}As$
Compositions for quaternary alloys were not reported. 24

3.1 Epitaxial layer structure for an EAM with optimized free carrier absorption and cutoff frequency. 36

4.1 InGaP/GaAs dual junction PV device for integration with an EAM. 77
4.2 2J JV figures of merit for the modeled top-bottom device and the measured top-top device. 84

5.1 Literature results for MOVPE grown InP solar cells. 97
5.2 InP solar cell layer structure for investigating the effect of the front surface field thickness 100
5.3 Proposed monolithic PV/EAM epitaxial layer structure. . . 109
5.4 Figures of merit for the InP PV junction for AM0 and 808 nm. 114

List of Figures

1.1 Launch cost to Low Earth Orbit per kilogram of mass over time. Adapted from Jones [1]. 2
1.2 High level overview of proposed hybrid photovoltaic/data communication system that utilizes free space optical communication. 6

2.1 Equivalent circuit single diode model of a solar cell. 8
2.2 Double diode model equivalent circuit for a solar cell. . . . 10
2.3 Left: Illustration of a single junction GaAs solar cell with a bandgap of 1.4 eV, corresponding to 885 nm.
Right: Plot of the AM0 solar spectrum with the wavelength range in which GaAs optimally collects highlighted in green, with shorter wavelength photons resulting in thermalization loss and longer wavelength photons resulting in transmission loss. 13
2.4 Left: Illustration of a current state of the art triple junction solar cell with an InGaAs bottom junction, GaAs. middle junction, and an InGaP top junction.
Right: Plot of the AM0 solar spectrum with the collection ranges for each subcell highlighted in blue for the InGaP junction, green for the GaAs junction, and red for the InGaAs junction. 14
2.5 Overview of different types of optical modulators. 16
2.6 The effect of an applied voltage on a confined energy state with 0 V (left) and an applied voltage (right) showing the decrease in the transition energy in the case of an applied bias. 18

2.7 *nextnano* simulation of transition energy intensity for the bound states of ten repeats of $In_{0.53}Ga_{.47}As$ quantum wells and $In_{0.52}Al_{0.48}As$ barriers with no applied electric field (left) and a 100 kV/cm electric field (right) for various energy transition levels. 20

3.1 Lattice constant versus bandgap for commonly grown III-V semiconductors. A line is drawn at 1.55 μm to denote the desired laser communication wavelength. The region above the line represents materials that are optically transparent to 1.55 μm and can be used for collection of solar energy. . 26
3.2 Top Left: Illustration of a test structure of 50 repeats of InGaAs/InAlAs
Bottom Left: InGaAs/InAlAs test structure etched in 1:1:38 H_2O:H_2O_2:H_3PO_4
Top Right: Illustration of a test structure of 50 repeats of InGaAs/InP
Bottom Right: InGaAs/InP test structure etched in concentrated HCl. 27
3.3 Percent absorbed light through 50 nm of material for InGaAs, InAlAs, and InP by wavelength. 29
3.4 Transmission versus wavelength for various thicknesses of InP with doping levels of 8 x 10^{19} cm^{-3}. 31
3.5 Transmission versus wavelength for various thicknesses of InP with doping levels of 7 x 10^{18} cm^{-3}. 31
3.6 Dual-layer LCL model used to determine the resistive components of the LCL for calculating cutoff frequency, showing the cell area for a 1 cm^2 EAM. 32
3.7 Parameter space for cutoff frequency of a 1 cm^2 EAM for varied LCL bulk and capping layer thicknesses. 33

3.8 Simulated cutoff frequency versus contact resistivity for a 0.25 cm x 0.25 cm device. 35
3.9 Contact resistivity versus anneal temperature for various metal stacks for contact to n-InP. 36
3.10 Left: Mask design of the EAMs.
Right: Photograph of fully fabricated EAMs. 39
3.11 Fabrication procedure for the EAM. 40
3.12 Illustration of the structure used for simulations in Lumerical. 42
3.13 Extracted electric field for 0 V (blue) and -10.25 V (green) using the CHARGE solver. 43
3.14 Absorption coefficient versus wavelength for the simulated Lumerical structure. 44
3.15 Contrast ratio versus wavelength for the simulated Lumerical structure. 45
3.16 Simulated contrast ratio for varying InGaAs quantum well and InAlAs barrier thicknesses for an applied bias of -5 V . 46
3.17 Simulated contrast ratio for varying InGaAs quantum well and InAlAs barrier thicknesses for an applied bias of -10 V 46
3.18 Peak contrast ratio location in nanometers for varying InGaAs quantum well and InAlAs barrier thicknesses for an applied bias of -5 V. The wavelength range of 1545-1555 nm is cross hatched. 47
3.19 Peak contrast ratio location in nanometers for varying InGaAs quantum well and InAlAs barrier thicknesses for an applied bias of -10 V. The wavelength range of 1545-1555 nm is cross hatched. 48
3.20 QW regions for the QW thickness study. 49
3.21 Measured ON/OFF ratio for EAMs with QW thicknesses of 6, 8, and 10 nm. All barrier thicknesses are 10 nm, and the applied bias is -5 V. 50

3.22 Peak contrast ratio location versus quantum well thickness for different well thicknesses via simulation and measured experimentally. The barrier thickness for 10 nm for all cases. 50
3.23 Epitaxial layer structure for PL test structures. 52
3.24 Photoluminescence and ON/OFF ratio for measured EAMs and PL test structures. The EAMs had both PL and ON/OFF ratio measured, with ON/OFF ratios being measured at voltages from -2 V to -15 V. 53
3.25 Device structures and simulated optical transition intensities for 50x MQW structures at 0 V and -5V bias, along with the change in transmission for the two designs. Top: Square QW (SQW) design. Bottom: Coupled QW (CQW) design. 54
3.26 Square quantum well and coupled quantum well modulators. 55
3.27 Voltage biased IQE of a SQW EAM. 56
3.28 Voltage biased IQE of a CQW EAM. 56
3.29 Cutoff frequency versus device area for EAMs 57
3.30 Capacitance versus area for EAMs of varied size. 58
3.31 ON/OFF ratio comparison to literature reported values. . 60
3.32 QW region thickness normalized ON/OFF ratio comparison to literature reported values. 60

4.1 Left: Mask design of the GaAs PV devices for integration. The red is the mesa isolation, the blue is the top metal, and the green is the back contact.
Right: Photograph of a fully fabricated GaAs PV. 64
4.2 a: Process flow for the GaAs PV device for the mechanically stacked hybrid device.
b: Process flow for the InGaAs/InAlAs EAM for the mechanically stacked hybrid device.
c: Illustration of mechanically stacked hybrid device. . . . 66

4.3 AM0 illuminated current density-voltage measurement of the GaAs PV device. 67
4.4 Fractional power loss versus AlGaAs LCL thickness for a 1 cm^2 GaAs PV device. 68
4.5 Dark current density-voltage measurement and single-diode model fit of a fabricated EAM. 69
4.6 ON/OFF contrast measured at 3 V and 5 V reverse bias. . 70
4.7 Photograph of a completed, mechanically stacked hybrid EAM/PV device with a 1 cm x 1 cm EAM and a 1 cm x 0.75 cm PV cell. 71
4.8 J-V characteristics of a modulator and PV device pre-bond and post-bond showing identical performance. 72
4.9 Top: Oscilloscope capture of on-off-keying of a hybrid, mechanically bonded PV/EAM device while simultaneously harvesting solar energy.
Bottom: Photograph of a bonded PV/EAM atop a planar retroreflector for reflection mode testing. 73
4.10 Left: Full wafer mask design for 6, 2J PV devices for integration in a PCB.
Right: Schematic of PV devices. 74
4.11 Left: Full wafer mask design for 12, segmented EAMs for integration in a PCB.
Right: Schematic of segmented EAMs. 75
4.12 Epitaxial layer structure of the 2J PV device, based on results by Polly *et al.,* [66] 78
4.13 Hovel modeling of the 2J PV device, based on results by Polly *et al.,* [68, 66] 78
4.14 Fractional power loss in a 1.94 cm^2 2J PV cell for a GaAs LCL of varied thickness and doping. 79

4.15 Transmission loss at 1550 nm for a GaAs LCL of varied thickness and doping. 80
4.16 Hovel modeling fit of the fabricated 2J PV device before ARC [68]. 82
4.17 ARC thickness optimization based on non-ARC EQE results shown in Figure 4.16. 82
4.18 AM0 illuminated J-V curve for the 2J device after ARC deposition. 83
4.19 Measured transmission loss in the 2J PV device. 84
4.20 Epitaxial layer structure of the EAM for integration with the 2J PV device for the 0.5 U form factor. 85
4.21 ON/OFF ratio measurements of the EAM for mechanical bonding. 86
4.22 Cutoff frequency of the EAM for mechanical bonding. . . . 87
4.23 PDMS structure for modeling of transmittance in TFCalc . 88
4.24 TFCalc modeling of C-Band transmittance through a GaAs substrate bonded to an InP substrate with PDMS. 89
4.25 ZnS/MgF_2 structure for modeling of transmittance in TFCalc 90
4.26 C-Band and 1550 nm optimized transmittance with various ZnS and MgF_2 coatings. 91
4.27 A picture of a test wafer for bonding to the PCB with the top metal design of the PV (left) and EAM (right) electroplated for placing and testing. 92
4.28 Photographs of the 3D printed chuck for wire bonding to both sides of the PCB. 93
4.29 Final 0.5 U form factor mechanically stacked PV/EAM device. 94

5.1 High level illustration of a three terminal monolithic device on InP. 96
5.2 Illustration of the fabrication procedure for a single junction, top-bottom contact InP solar cell. 98

5.3 Picture of a completed InP solar cell with 12, 1 cm^2 cells on a 2” wafer. 99
5.4 AM0 illuminated J-V curves of InP solar cells with varying FSF thickness. 100
5.5 Efficiency versus FSF thickness for InP solar cells. 101
5.6 Open circuit voltage, short circuit current density, fill factor, and efficiency as a function of emitter thickness 102
5.7 Internal quantum efficiency comparison of the best InP cell fabricated at RIT compared to the best reported literature value from Keavney *et al.*, [75] 103
5.8 Mask design for the monolithic device with device areas of 1.00 cm^2 and 0.25 cm^2 104
5.9 Fractional power loss and two pass transmission of an InP and InAlAs LCL layer doped to 1 x 10^{19} cm^{-3}. 105
5.10 Fractional power loss and two pass transmission of an InP and InAlAs LCL layer doped to 5 x 10^{19} cm^{-3}. 106
5.11 Fractional power loss in a 1.00 cm^2 InP PV device for varying LCL thicknesses and doping. 108
5.12 Two pass transmission at 1550 nm through a p-InP LCL varying thickness and doping. 108
5.13 Illustration of a demonstrated epitaxial layer structure for a monolithically integrated EAM/PV device. 110

5.14 Fabrication procedure for a five level, monolithically integrated EAM/PV device.
a. Metal is deposited on the n-InGaAs contact.
b. The *np*-junction of the InP PV device is mesa isolated.
c. Metal is deposited on the p-InP common contact.
d. The n-InGaAs contact is etched from the field of the device.
e. The *pn*-junction of the EAM is mesa isolated.
f. Metal is deposited on the n-InP contact. 112
5.15 Photograph of the fully fabricated, monolithically integrated device under test. 113
5.16 AM0 illuminated current density-voltage measurements of a 1.00 cm^2 and 0.25 cm^2 monolithic devices. 114
5.17 Internal and external quantum efficiency and reflectance of the InP PV junction of the monolithic device. 115
5.18 ON/OFF ratio measurements of the monolithic device, with the peak observed at 1564 nm. 116
5.19 1550 nm illuminated bandwidth measurements of the EAM junction of a 120 mm^2 area EAM and a 35 mm^2 area EAM, the 3 dB line indicated as a horizontal line. The applied voltage was 0 to -5 V with a square wave. 117
5.20 Illustration of simultaneous power generation and data communication testing (left), 750 nm LED illuminated current density-voltage curve (middle), and modulated data and driving signal (right). 117

A.1 Block diagram of ON/OFF ratio measurement testing. . . 128
A.2 Photograph (top) and simplified diagram (bottom) of the optical cutoff frequency test setup used for testing of EAMs. 129

Chapter 1

Motivation

1.1 Reduction of SWaP

One of the major drivers in recent and future satellite research is the need for more satellites and increased communication speed with the emergence of proliferated low-Earth orbit (pLEO) constellations. Of the nearly 7,000 satellites currently in orbit, nearly 6,000 of them are in LEO [2]. Mega-constellations, such as Starlink and OneWeb, currently have over 5,000 satellites in orbit, with plans of this number surpassing 30,000 [3]. This push is in parallel with the ongoing need for the reduction of the size, weight, and power (SWaP) of mission critical subsystems, such as power generation systems and communications.

Figure 1.1 shows that, over time, there has been a steady decrease in the cost per kilogram of mass to launch to Low Earth Orbit (LEO). This is largely attributed to advances in rocketry, with SpaceX's Falcon Heavy launch cost having reached 1.4 $k/kg [1]. For evaluation of basic science payloads, there has been an increased interest in the use of nanosatellites such as CubeSats due to their orders of magnitude reduction of the

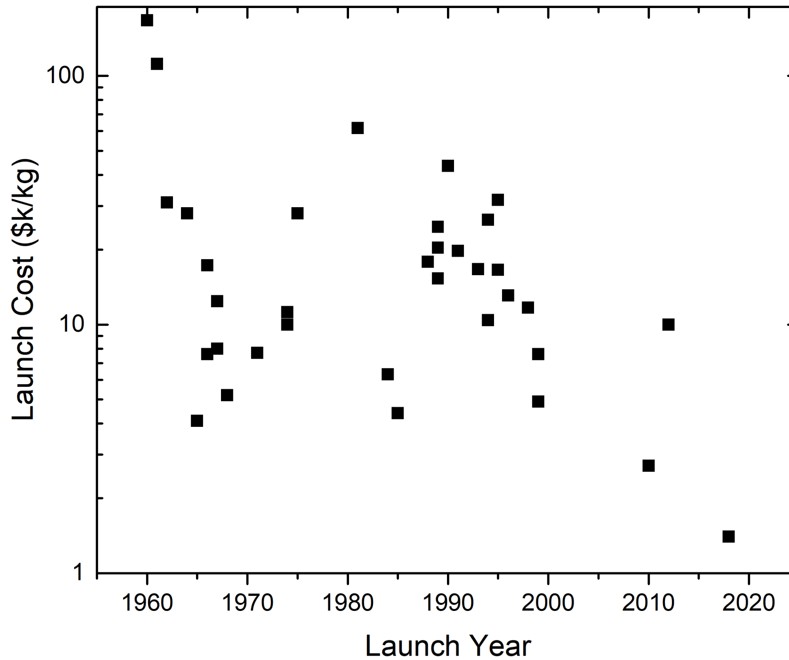

Figure 1.1: Launch cost to Low Earth Orbit per kilogram of mass over time. Adapted from Jones [1].

SWaP compared to conventional satellites [4]. Nanosatellites are typically between 1 to 8 kg in mass, and are 1 to 6 m^3 in volume. These nanosatellites enable lower cost LEO missions, making spaceflight testing of scientific payloads more accessible.

The small size of nanosatellites means that SWaP is at a premium. To maximize the SWaP available for the payload, it is imperative to minimize the SWaP of mission critical subsystems. Critical subsystems include, but are not limited to, power generation and communication. The power generation system typically utilizes high efficiency, III-V based photovoltaics due to their excellent mass specific power density compared to other classes of photovoltaics. This is contrasted with the communication systems that satellites rely on, which require high SWaP RF transceivers to establish an uplink and downlink with a ground station. Current state of the art (SoA) ultra-high frequency (UHF) band transceivers designed specifically for CubeSats, supplied by EnduroSat,

contribute to nearly 10 % of the mass of a 1 m^3 CubeSat. Attempts to integrate the communication system with the power generation system's solar arrays has been an active area of research. Integrating the UHF antenna with a deployable solar array has been flight tested by NASA and development on this system is ongoing [5, 6].

There exists, however, interest in communication protocols outside of RF. Specifically, free space optical (FSO) and laser communication are considered key technical areas of interest in NASA's Technology Roadmap [7]. RF communications require components that are heavy and high power consuming [8]. Additionally, the communication bands the RF communications operate over (30 kHz to 300 GHz) are heavily regulated and congested. Free space optical communication (FSO) is a line of sight communication technique that uses a laser to transmit data, capable of bandwidths of 1000 times greater than RF. Additionally, FSO is nearly an order of magnitude lower in power consumption, with RF requiring nearly 1000 W for 1 Gbps transmission, compared to 100 W for FSO according to calculations by William *et al.,* [9]. Being a line of site communication technique with smaller beam divergence than RF, FSO is also more secure than RF communication [10, 11]. Communication at 1.55 μm is of particular interest as it is considered eye-safe and substantial equipment and infrastructure already exist to support this wavelength from the telecommunications industry [12]. Additionally, the communication spectrum above 300 GHz is unlicensed, which provides facile access to these bands for communication and data transmission.

PV has the potential to be an enabling platform for optical wireless communication (OWC) [13, 14, 15, 16]. Power generation can occur via solar illumination, and data communication can occur with a laser. Kim *et al.,* demonstrated simultaneous power

generation and data reception of a 27 x 27 mm silicon solar cell at a rate of 3 kbps and a cutoff frequency of 10 kHz [17]. Shin *et al.,* further improved upon this, attaining a data rate of 17.05 Mbps using a self-reverse biased receiver circuit [18]. Organic PV has also been used for PV as both an energy harvester and data receiver, attaining a cutoff frequency of 1.3 MHz and data rate operation of 34 Mbps [19]. In addition to using solar irradiation as the means for power generation, Fakidis *et al.,* have demonstrated a GaAs laser power converter with 42 % efficiency operating at 0.5 Gbps at 847 nm [20].

Using PV as both the power generation and data communication element poses several challenges; for one, the wavelength used for data communication is limited to what the PV material can absorb. High efficiency PV cells, such as the current state of the art inverted metamorphic multijunction solar cells, are optically transparent to 1.55 μm light [21]. Silicon, which is used for the vast majority of terrestrial solar panels, is also optically transparent at 1.55 μm. Additionally, while PV has the potential as a receiver, its potential as a transmitter of data is limited. Using PV as a transmitter would require the PV cell to operate in forward bias, increasing the power draw of the device. Additionally, this wavelength would be at the band edge of the device, and would not be at 1.55 μm for typical state-of-the-art PV.

1.2 Proposed Solution

To address this need a low SWaP bidirectional communications system that utilizes free space optical communication at 1.55 μm in a hybrid photovoltaic/data communication device coupled with a retroreflector is proposed. A high level illustration of the hybrid

device is shown in Figure 1.2. Power is generated via the photovoltaic effect, with either a single junction or multijunction III-V based photovoltaic (PV) device. This PV device can be designed for use as a solar cell, generating power via multiple wavelengths of light incident from the sun, or as a laser power converter, designed to efficiently generate power from a specific wavelength. The material for the PV device is made optically transparent to the wavelength of light used for laser communication, typically 1.55 μm. As a result, the communication wavelength transmits through the PV cell with minimal insertion loss. The PV cell is stacked, either mechanically or grown monolithically, on a multiple quantum well (MQW) modulator that modulates the incoming laser signal. That signal then bounces off a corner cube retroreflector and the modulated data is returned to the sender.

Careful design consideration is required to optimize the PV device to ensure maximum power conversion efficiency (PCE), minimize insertion loss, maximize the operating speed of the modulator, and ensure a strong ON/OFF ratio. By and large, these goals are in tension with one another. This proposal investigates the parameters responsible for these intended device goals and how to optimize them.

1.3 Outline of Dissertation

Chapter 1 provides a high level motivation for this document and provides a proposed solution to a low SWaP FSO communications platform that hybridizes power generation and communication. Chapter 2 provides an overview of the theory of operation for solar cells and electroabsorption modulators. Additionally, Chapter 2 provides a literature

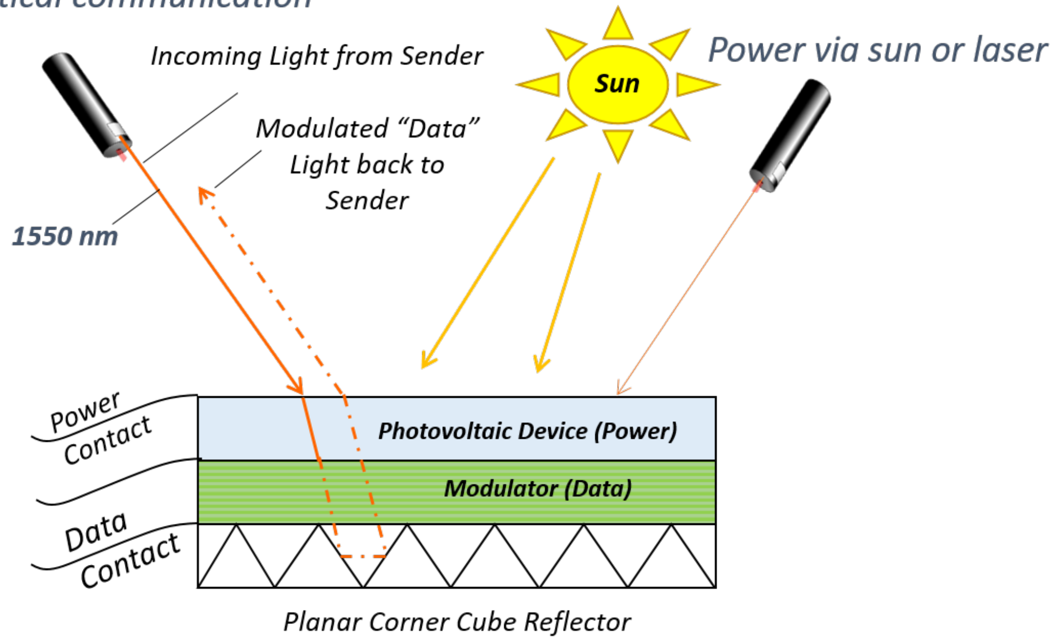

Figure 1.2: High level overview of proposed hybrid photovoltaic/data communication system that utilizes free space optical communication.

review of surface normal MQW electroabsorption modulators and an overview on free space optical communication. Chapter 3 discusses the development of surface normal EAMs for high speed operation at 1.55 μm. Chapter 4 details the development of a mechanically stacked hybrid device for single cell and 0.5 U form factor integration. Chapter 5 provides an alternative monolithically integrated hybrid communication/power generation device.

Chapter 2

Introduction

2.1 Solar Cell Theory of Operation

A semiconductor solar cell is, generally, a *pn*-junction diode that generates photocurrent when a photon is absorbed with enough energy to excite an electron from the valence band to the conduction band. The energy required to enable this transition is the bandgap of the material. The equivalent circuit single diode model for a solar cell is shown in Figure 2.1. The generated photocurrent is dependent upon the probability of a photon with a given energy being collected, known as the *quantum efficiency* (QE) of the solar cell. Additionally, this photogenerated current is dependent upon the flux of incident photons (b_s). This photogenerated current is referred to as the *short circuit current density* (J_{SC}). The formal definition for J_{SC} as it depends upon the energy of a photon is given by Equation 2.1 [22] .

$$J_{SC} = q \int_{E_g}^{\infty} b_s(E) QE(E) dE \tag{2.1}$$

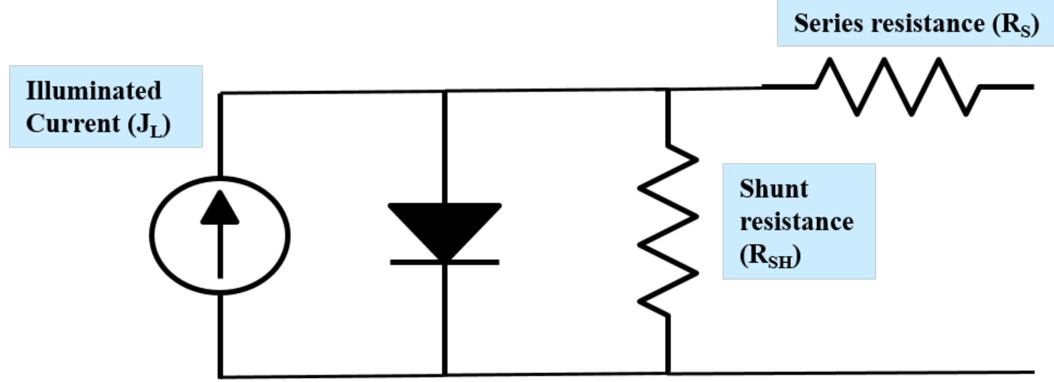

Figure 2.1: Equivalent circuit single diode model of a solar cell.

where q is the elemental charge. The solar cell parameter of chief importance is the device efficiency (η). In simplest terms, the efficiency of a solar cell is the ratio of generated electrical power to the the amount of incident optical power. More specifically, the maximum power of a solar cell is given by the product of the voltage (V_{MP}) and current (I_{MP}) at the maximum power point (P_{MP}). V_{MP} and I_{MP} are related to the directly measurable open-circuit voltage (V_{OC}) and J_{SC} by the *fill factor* (FF) of the cell, which is heavily influenced by the parasitic resistances in the device. The equation for device efficiency is [22]:

$$\eta = \frac{P_{Max}}{P_{In}} = \frac{J_m V_m}{P_{In}} = \frac{J_{SC} V_{OC} FF}{P_{In}} \tag{2.2}$$

From Figure 2.1, assuming zero series resistance and infinite shunt resistance, the current as it depends on voltage (V) can be written as [22]:

$$J(V) = J_{SC} - J_0[(exp(qV/k_B T) - 1)] \tag{2.3}$$

Where k_b is the Boltzmann constant and J_0 is referred to as either the reverse saturation current or dark current, which is dependent upon the minority carrier lifetimes ($\tau_{n/p}$) and depletion widths ($w_{n/p}$) in the p and n regions. With no current flow, Equation 2.3 can be rearranged to solve for the open-circuit voltage as it depends on the reverse saturation current [22]:

$$V_{OC} = \frac{k_B T}{q} ln \left(\frac{J_{SC}}{J_0} + 1 \right) \tag{2.4}$$

Modeling in parasitic resistances, denoted as the *shunt resistance* (R_{Sh}) and *series resistance* (R_S) in Figure 2.1, modifies Equation 2.3 to:

$$J = J_{SC} - J_0 \left[exp \left[\frac{q(V - JR_s)}{k_B T} \right] - 1 \right] + \frac{q(V - JR_s)}{R_{Sh}} \tag{2.5}$$

Equation 2.5 assumes that the ideality (n) of the diode is unity, and for practical device modeling this is rarely an entirely accurate description of solar cell operation. By and large, ideality for devices ranges between $n = 1$ and $n = 2$. A solar cell with an ideality of one has recombination primarily occurring in the quasi neutral region (QNR) of the device, whereas a solar cell with an ideality of 2 has recombination primarily occurring in the depletion region of the device.

Equation 2.5 can be modified to determine the ideality of a diode by:

$$J(V) = J_{SC} - J_0(exp(qV/nk_B T) - 1) \tag{2.6}$$

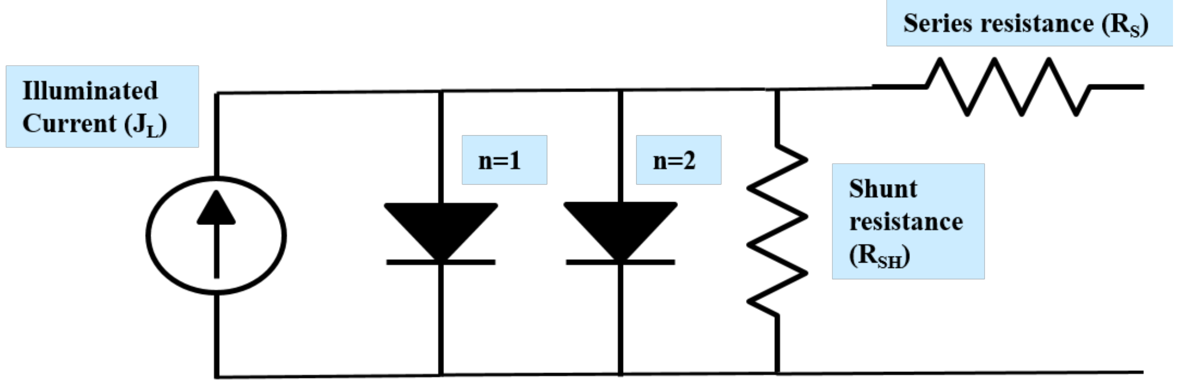

Figure 2.2: Double diode model equivalent circuit for a solar cell.

Arguably more useful than extracting ideality is determining the dark current contribution from recombination in the QNR and depletion region by utilizing a two diode model, assuming two diodes in parallel, one with an ideality $n = 1$ and one with an ideality of $n = 2$, with the equivalent circuit schematic shown in Figure 2.2. This splits the J_0 term into two separate terms, J_{01} and J_{02}. This gives a more complete model for analyzing not just solar cells, but also other optoelectronic devices where dark current contribution is of integral importance. Typically, analysis of dark current contribution is performed without light bias, eliminating the J_{SC} term, which even under low intensity dominates the total current generated for any high quality semiconductor material. The complete dark current model for a two diode equivalent circuit is given as:

$$J(V) = J_{01}\left[exp\,\frac{q(V-JR_S)}{k_BT}\right]-1\Bigg] + J_{02}\left[exp\,\frac{q(V-JR_S)}{2k_BT}\right]-1\Bigg] + \frac{q(V-JR_s)}{R_{Sh}} \quad (2.7)$$

2.2 III-V Photovoltaics

Since 1976, the National Renewable Energy Laboratory has tracked the record solar cell efficiencies for multiple classes of photovoltaics, such as silicon, organic, and III-V based photovoltaics [23]. Typically, silicon based solar cells have been utilized for most terrestrial applications due to their low cost, now less than 1$/W. These cells, however, have attained a maximum, one sun efficiency of 26.1 %. For space applications, however, the mission specific power requirement often requires high efficiency panels.

Single junction solar cells have an inherent peak efficiency limit, known as the Shockley-Queisser limit [24]. For a single junction cell under the AM0 spectrum, the theoretical maximum efficiency is 30 % [25]. The primary limiting factors are from transmission of photons with energies below the bandgap of the material and thermalization of photons with energies that have energies much greater than the bandgap of the material. To attain efficiencies, and subsequently, the power required for space applications, these losses need to be mitigated.

2.2.1 Multijunction Solar Cells

To surpass the intrinsic limits of single junction solar cells, an alternative approach is to utilize III-V semiconductor compounds, that is, materials from Groups III and V of the periodic table, and to stack materials in ascending bandgaps atop one another to minimize thermalization and transmission loss. This partitions the solar spectrum in order to more efficiently collect a greater portion wavelengths of light output from the sun. These concepts are illustrated in Figures 2.3 and 2.4. These solar cells, known as 'multijunction

solar cells' (MJSC), attain the highest efficiencies of all classes of photovoltaics, with the premier result being a six junction device with 39.5 % by France *et al.,* from the National Renewable Energy Laboratory [26].

The first triple junction solar cell was grown lattice-matched to germanium, with a 0.74 eV germanium bottom cell, a 1.40 eV $In_{0.01}Ga_{0.99}As$ middle cell, and a 1.80 eV $In_{0.49}Ga_{0.51}P$ top cell. This design achieved a cell efficiency of 29.7 % under the AM0 spectrum. [27, 28]. This design, however, is not the optimal configuration for a triple junction cell. For an optimized triple junction using GaAs and InGaP based compounds as the middle and top cells, the ideal bandgap for the bottom cell is between 0.95 and 1.05 eV [29]. To move to a more optimized design, an inverted metamorphic (IMM) cell was developed [21]. The bottom Ge junction was replaced with an 1.0 eV, $In_{0.30}Ga_{0.70}As$ bottom cell. Additionally, as this design is not lattice matched, a stepwise metamorphic grade is required to grade the lattice constant. To minimize the impact of threading dislocations and defects on the higher voltage cells (the top and middle cell), the cell is grown inverted on a GaAs substrate, with the InGaP top cell grown first. To grow the InGaAs bottom cell, an optically transparent buffer of $Ga_xIn_{1-x}P$ is grown, grading the lattice constant from 5.66 $\mathring{A}$ to 5.76 $\mathring{A}$, which is the same lattice constant as the desired 1.0 eV $In_{0.30}Ga_{0.70}As$. This design recorded an AM0 efficiency of 30.6 %.

Current commercially available MJSCs often utilize three junctions, with the highest lot minimum efficiency being an IMM cell with an efficiency of 32 % from Solaero Technologies. This triple junction solar cell, illustrated in Figure 2.4, uses an InGaAs (1.0 eV) bottom junction, a GaAs middle junction (1.4 eV), and an InGaP (1.9 eV) top junction. This design efficiently collects light from 250 to 1240 nm, where most of the

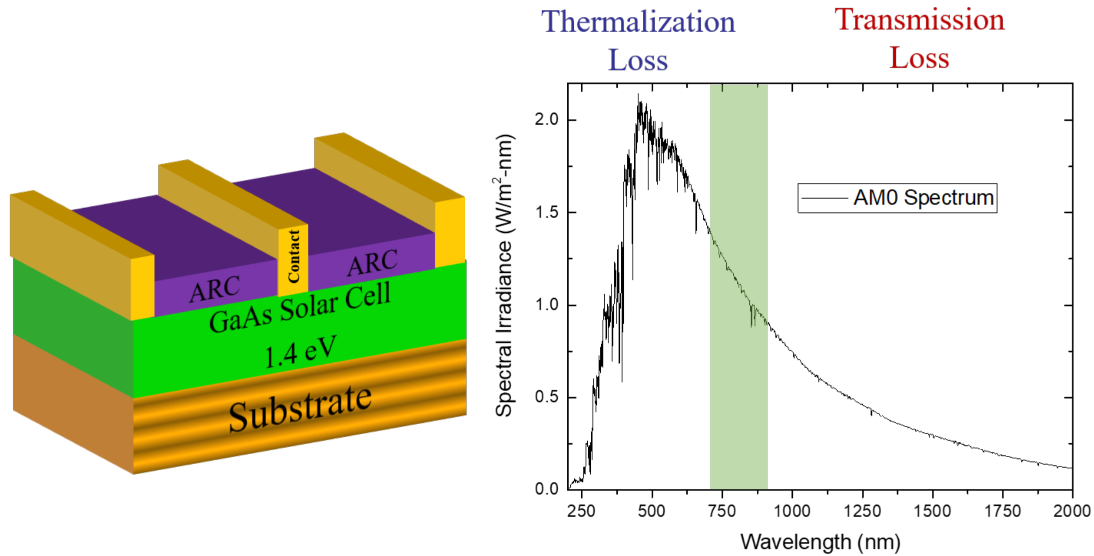

Figure 2.3: Left: Illustration of a single junction GaAs solar cell with a bandgap of 1.4 eV, corresponding to 885 nm.
Right: Plot of the AM0 solar spectrum with the wavelength range in which GaAs optimally collects highlighted in green, with shorter wavelength photons resulting in thermalization loss and longer wavelength photons resulting in transmission loss.

spectral irradiance of the solar spectrum resides. Critically, the current state of the art technology does *not* collect at 1550 nm, which is the wavelength of interest for optical communication. As a result, the current state of the art, commercial grade space-base photovoltaics are able to be hybridized with optical communication based around 1550 nm.

2.3 Free Space Optical Communication

Radio frequency (RF) communications have historically dominated both terrestrial and space-based communication. RF communications use frequencies of 30 kHz to 300 GHz

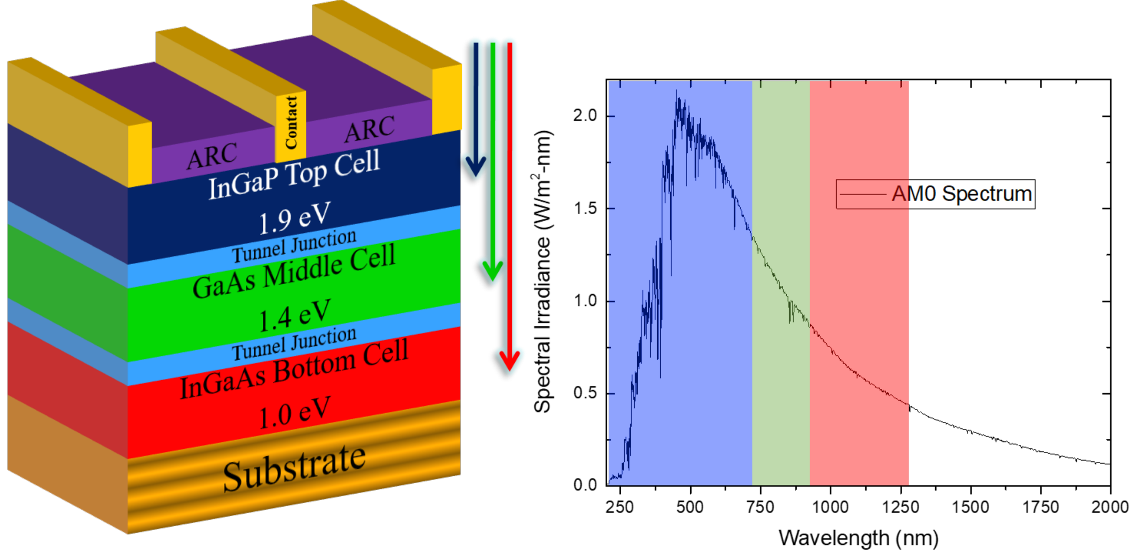

Figure 2.4: Left: Illustration of a current state of the art triple junction solar cell with an InGaAs bottom junction, GaAs. middle junction, and an InGaP top junction. Right: Plot of the AM0 solar spectrum with the collection ranges for each subcell highlighted in blue for the InGaP junction, green for the GaAs junction, and red for the InGaAs junction.

for communication, which corresponds to a wavelength range of 1 mm to 10 km. Maximum data rate attainable is inversely proportional to the wavelength use for communication, limiting the theoretical maximum rates possible over RF communication to the hundreds of GHz range. Beam divergence is also directly related to the wavelength of the carrier signal, given by:

$$\theta = \frac{\lambda}{\pi w_0} \tag{2.8}$$

where θ is the beam divergence, λ is the wavelength of the carrier signal, and w_0 is the beam waist. From Equation 2.8, as the wavelength used decreases, the beam divergence also decreases. A lower beam divergence results in a higher intensity at the signal's intended target, given by:

$$I(r) = I_0 e^{-2(r/w_0)^2} \tag{2.9}$$

where $I(r)$ is the signal strength at a radial distance r away from the beam center, and I_0 is the initial signal intensity at the beam waist. By decreasing the beam divergence, the signal intensity at the intended signal receiver is higher, resulting in a superior signal-to-noise ratio. In addition, RF communication bands are, at present, highly congested due to the high demand for access to these bands.

To circumvent the limitations of RF communications, significant interest has evolved in the area of free space optical communication (FSOC). FSOC is a line of sight communication technique that sends and receives information via laser emission as the carrier signal. The wavelengths used are in the range of 1 to 10 microns (30-300 THz in frequency). As a result, the possible data rates achievable with FSOC are more than 100 times greater than what is possible with RF communications. Due to the smaller wavelength, the beam divergence for an equidistant communication link is three orders of magnitude smaller than that of RF. This reduced beam divergence and inherent line of sight nature of FSOC makes it a more secure means of communication compared to RF communication [11, 10]. In addition to superior data rates and security provided by FSOC, FSOC equipment is also lower SWaP compared to RF communication equipment [9].

Utilizing PV as a receiver has been demonstrated in silicon single crystal PV [30], silicon polycrystalline [15], organic PV [19], and a GaAs PV cell [20]. Using a 1 mm diameter GaAs cell, Fakidis *et al.,* demonstrated a data rate as a receiver of 0.5 Gbps

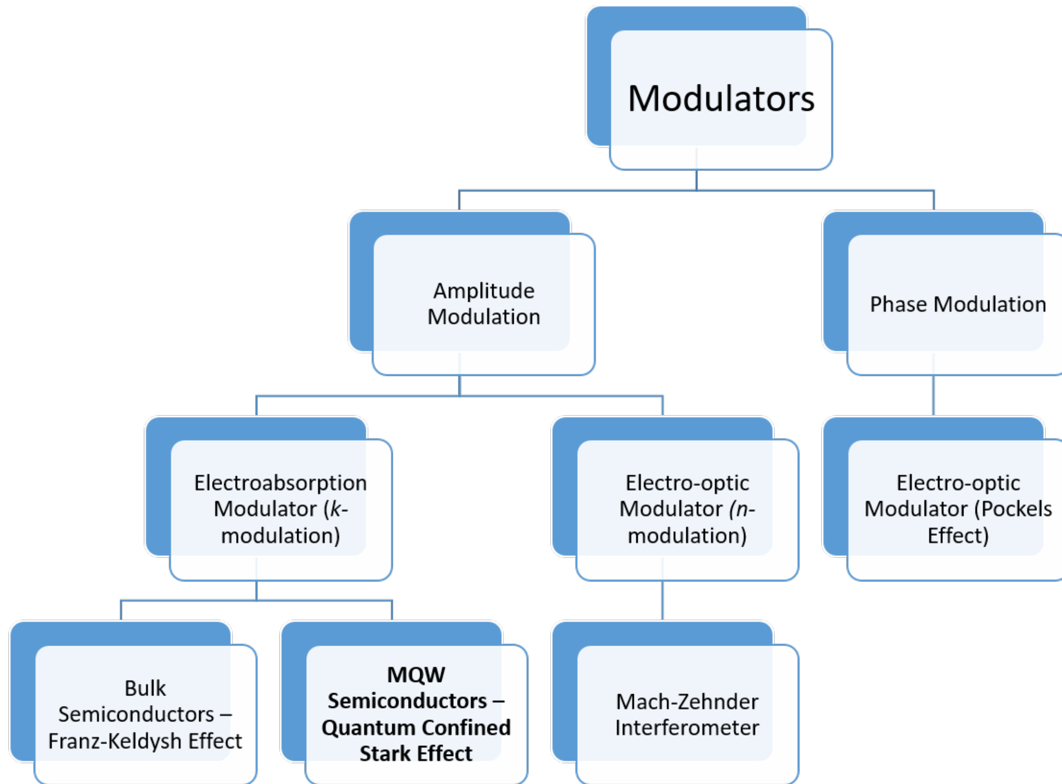

Figure 2.5: Overview of different types of optical modulators.

over a 2 m link. PV can be utilized as a transceiver by taking advantage of the the electroluminescent properties of direct bandgap semiconductors. PV as a transceiver, however, has been by comparison difficult to demonstrate with speeds above the kbps range [31, 32, 33]. The emission of the PV transceiver cell is omnidirectional, eliminating the benefit of FSOC as a more secure communication technique. Additionally, the communication wavelength used with PV as a transceiver is limited to the bandgap of the PV device.

2.4 Electroabsorption Modulators

Modulation is, by definition, the alteration of a property of an incoming periodic waveform. By modifying a property, such as amplitude, phase, or polarization, digital data communication can occur. Figure 2.5 shows several different classes of modulators that are used for amplitude and phase modulation in optical communication. In optical communication phase modulation is often employed using an *electro-optic modulator* (EOM) taking advantage of the Pockels effect [34]. The Pockels effect is an electro-optic effect where the real component (n) of the refractive index of a material is changed linearly with an applied electric field. Lithium based materials are common, such as lithium niobate ($LiNbO_3$) [35] as is silicon for silicon based photonic platforms [36]. EOMs can also be used for amplitude modulation when combined with a Mach-Zehnder interferometer [37]. Lithium and silicon EOMs, however, are not synergystic with III-V based PV.

Electroabsorption modulators (EAMs) provide an alternative pathway to allowing data modulation when combined with PV. EAMs modulate the imaginary (k) component of the refractive index of the material, consequently varying its absorption coefficient. This effect has been demonstrated in bulk semiconductors, coined the *Franz-Keldysh* effect [38], which broadens the band-edge absorption. This theory was used to explain the change in the optical absorption near the bandedge of a semiconductor in the presence of a large (MV/cm) electric field. To invoke a meaningful contrast between the ON and OFF states, a very large bias is required, which is counterproductive to implementing a low power device for data communication.

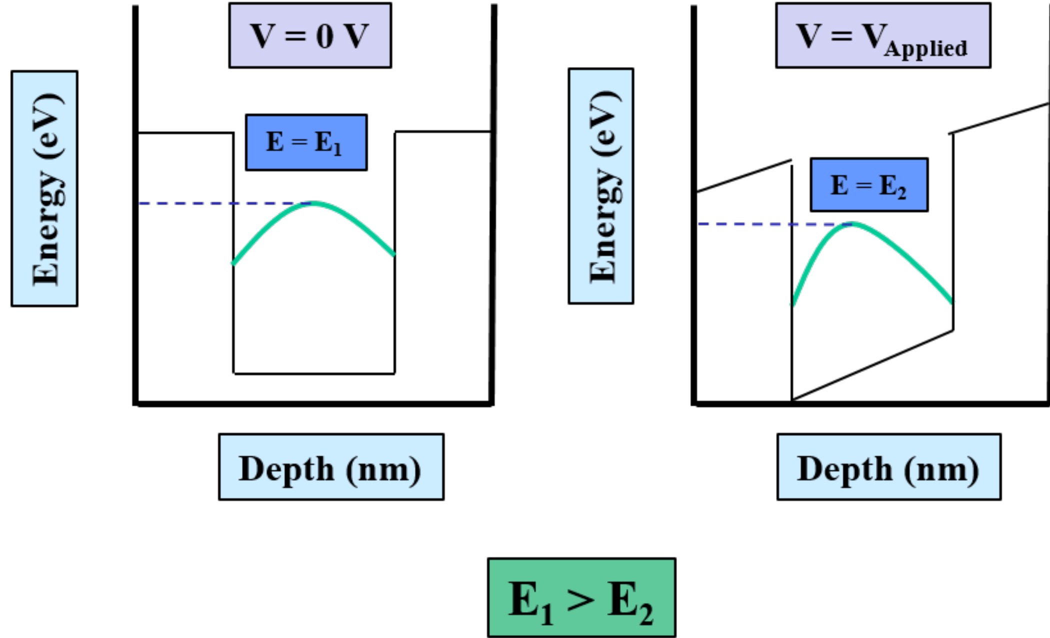

Figure 2.6: The effect of an applied voltage on a confined energy state with 0 V (left) and an applied voltage (right) showing the decrease in the transition energy in the case of an applied bias.

2.4.1 Quantum Confined Stark Effect

Miller *et al.,* first reported on the shift in optical absorption in AlGaAs-GaAs multiple quantum well (MQW) structures with an applied bias, which was explained by an electric field perpendicular to the MQW region separating the electrons and holes to opposite sides of the MQW layer, which reduces the energy of the electron-hole pair, effectively narrowing the bandgap, with this effect called the *Quantum Confined Stark Effect* (QCSE) [39]. This causes a red-shift in the absorption coefficient with an applied bias. Specifically, the QCSE is strongly dependent on the thickness of the quantum well, with an increase in well thickness red-shifting the band-to-band transition energy [10]. This is a result of the lowering of the transition energy states with an applied bias, illustrated in the band diagram in Figure 2.6.

In thin semiconductor layers, on the order of 10 nm or a few monolayers (MLs), the optical properties of the material dramatically change due to a shift in the confinement of the carriers. This creates a one dimensional quantum well. As such the change in the absorption properties of the MQW region will behave differently than the bulk material, which is governed by the Franz-Keldysh effect. This variance in absorption properties was first observed by Miller *et al.,* in a MQW structure of GaAs QWs and $Al_xGa_{1-x}As$ barriers [39]. The absorption properties in the MQW regions are governed by the quantum confined Stark effect (QCSE), which causes the red shift in the absorption coefficients of the overall material system when a perpendicular field is applied and a change in the complex refractive index of the material.

The shift in the electronic states from the application for a perpendicular electric field (ΔE) is given by [40]:

$$\Delta E = \frac{\eta(m^*, L_z)^2 m^* e^2 L_z^4}{8\hbar^2} F^2 \tag{2.10}$$

Where η is a material dependent proportionality constant, m^* is the effective mass, L_z is the thickness of the well, e the the charge of an electron, $\hbar$ is the reduced Planck's constant, and F is the electric field in the z-direction. The shift in electronic states is strongly tied to the to the applied electric field.

The optical response of a MQW modulator is dictated by the field dependent complex dielectric function. Schwedler *et al.,* provide a thorough derivation of the total dielectric function across the quantum well region (ϵ_{MQW}), leading to the simplified expression [40]:

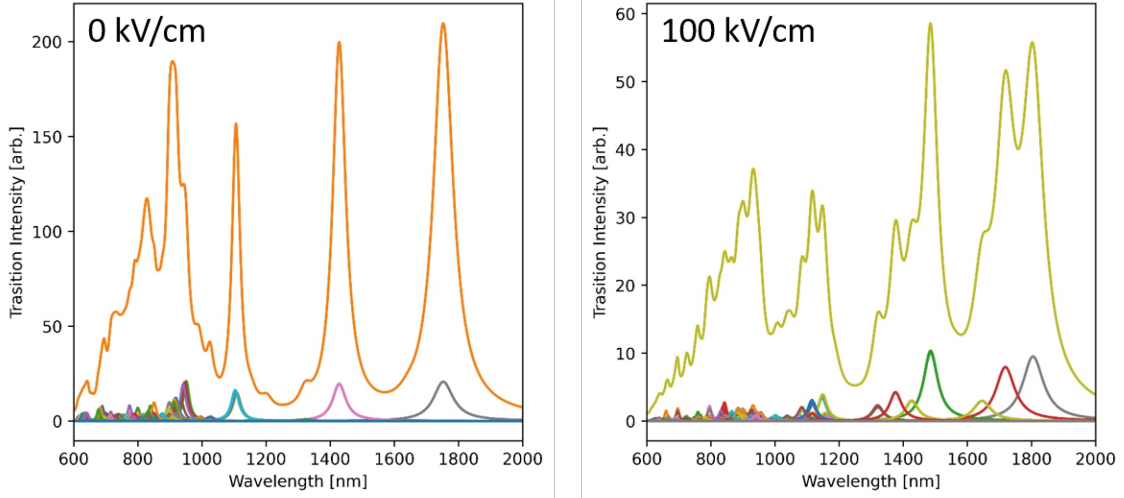

Figure 2.7: *nextnano* simulation of transition energy intensity for the bound states of ten repeats of $In_{0.53}Ga_{.47}As$ quantum wells and $In_{0.52}Al_{0.48}As$ barriers with no applied electric field (left) and a 100 kV/cm electric field (right) for various energy transition levels.

$$\epsilon_{MQW} = \frac{L_z}{L_z + L_c}\epsilon_w = \frac{L_b}{L_z + L_b}\epsilon_b \tag{2.11}$$

where L_b is the thickness of the barrier. This effect is shown in Figure 2.7, which shows a simulation of a shift in the energy transition intensity with an applied electric field for a quantum well stack with ten repeats of $In_{0.53}Ga_{.47}As$ quantum wells and $In_{0.52}Al_{0.48}As$ barriers.

This effect can be leveraged for optical communication with lower applied biases needed for attaining the same or greater contrast between ON and OFF states compared to bulk semiconductors using the Franz-Keldysh effect. The low driving voltages make MQW EAMs operating via the QCSE an attractive candidate for integration with III-V PV.

2.4.2 EAM Figures of Merit

A fundamental property of an electroabsorption modulator is its *contrast ratio* (CR), also referred to as *extinction ratio* (ER) or more generally the ON/OFF ratio. This is the ratio of the laser power after transmission in the 'ON' state to the 'OFF' state [41].

$$ON/OFF = e^{\Delta\alpha L_{MQW}} = \frac{P_{Out}(V = 0V)}{P_{Out}(V = V_{Applied})} \tag{2.12}$$

Where L_{MQW} is the length of the modulating region and $\Delta\alpha$ is the change in absorption coefficient. It is evident that as L_{MQW} increases, the ON/OFF ratio increases.

In addition to the ON/OFF ratio, the speed at which an EAM can operate is a critical parameter. The figure of merit for determining the operating speed of the EAM is the *cutoff frequency* (f_c). The cutoff frequency is defined by the frequency at which the output power has decreased by 50 %, also referred to as the 3 dB point. For large area devices, that is, devices that can be synergized with PV devices, the 3 dB point is dependent upon the device resistance (R) and capacitance (C), given by:

$$f_c = \frac{1}{\sqrt{2\pi RC}} \tag{2.13}$$

Typically, the analog cutoff frequency cannot be directly related to its corresponding digital data rate. EAMs using the QCSE, however, can encode data using the amplitude modulation scheme of on-off keying (OOK), where data is represented by either the presence or absence of a signal. OOK represents a special type of data modulation that can directly relate the cutoff frequency to data rate. The Nyquist-Shannon Theorem

states *"If a function f(t) contains no frequencies higher than W (cps), it is completely determined by giving its ordinates at a series of points spaced 1/2 W seconds apart"* [42]. Put more simply, for OOK, the cutoff frequency needs to be twice the maximum allowable data rate.

For a high signal to noise ratio, and the ability to strongly differentiate between a binary '1' or '0' during data communication, a high ON/OFF ratio is preferred. This improves the *bit error rate* (BER) of the device, which determines the ratio of incorrectly recieved bits to the number of transmitted bits. The BER is given by:

$$BER = \frac{N_{Err}}{N_{bits}} \tag{2.14}$$

The addition of any component into a system imparts some loss, known as *insertion loss* (IL). For an EAM, the insertion loss is driven by parasitic absorption of the target wavelength, with insertion loss being calculated as [41]:

$$IL = \frac{P_{In} - P_{Out}(V = 0V)}{P + In} = e^{\alpha(0V)L_{MQW}} \tag{2.15}$$

2.4.3 Surface Normal EAMs

EAMs have predominately been used for integrated photonics. As a result, there is substantial literature reporting on waveguide structure EAMs for communication at 1.55 μm. These structures have attained ON/OFF ratios of over 100 [43] with data rates of 40 Gbps [44]. Waveguide structures allow for a long modulating region down the device (greater than 100 μm), and the small geometry and cross-sectional area (1600 μm^2) result

in capacitance values of 5 pF, allowing for a cutoff frequency of 10 GHz due to the low RC time constant [43].

Due to their small apertures, waveguide EAMs cannot be used for free space optical communication, nor can they be easily integrated with large area solar arrays. An alternative geometry is a surface normal EAM, which have large apertures that can be synergistic with III-V PV. Extensive work has been done on both waveguide and surface normal EAMs for operation at 1.55 μm, with figures of merit shown in Table 2.1. Surface normal EAMs suffer from two primary issues: the short modulating region resulting in a reduced ON/OFF ratio for an equivalent bias, and the cutoff frequency and data rate being several orders of magnitude lower due to the increased device size of a surface normal modulator (and correspondingly, increased device capacitance).

2.5 Conclusion

Both photovoltaics and free space optical communication rely on similar physical properties and requirements; tailoring of the bandgap of a material and optical absorption are critical for device operation for both power generation and data communication. III-V photovoltaics are currently the primary source for power generation for space due to their high efficiencies attainable via the multijunction solar cell device design. Optical communication using PV has been demonstrated previously, primarily with the PV cell acting as a receiver. To target a specfic wavelength, and to allow for high speed transmission, coupling the PV cell with a surface normal electroabsorption modulator allows for a potential path for bidirectional communication with simultaneous data transmission.

Table 2.1: Table of literature reported EAM figures of merit for operation at and around 1.55 μm.
NR = Not Reported
InGaAs = $In_{0.53}Ga_{0.47}As$
InAlAs = $In_{0.52}Al_{0.48}As$
Compositions for quaternary alloys were not reported.

Material	**Structure**	**Wavelength (μm)**	**L_{MQW} (μm)**	**ON/OFF Ratio**	**Cutoff Frequency**	**Data Rate**	**Driving Voltage (V)**	**Citation**
GeSi	Waveguide	1.55	NR	4.0	40.7 GHz	28 Gbps	2.8	[45]
AlGaInAs	Waveguide	1.55	NR	79.4	4 GHz	NR	6	[46]
InGaAs/InAlAs	Waveguide	1.55	150	31.6	20 GHz	10 Gbps	1.2	[47]
InGaAs/InP	Waveguide	1.55	400	107.2	10 GHz	NR	2.6	[43]
InGaAs/InAlAs	Waveguide	1.55	100	31.6	40 GHz	40 Gbps	2.5	[44]
InGaAs/InAlAs	Surface Normal	1.53	NR	2.6	17 MHz	2 Mbps	5	[48]
InGaAs/InP	Surface Normal	1.59	3	2.6	NR	NR	40	[49]
InGaAsP/InAlAs	Surface Normal	1.55	5	11.2	10 MHz	NR	80	[50]
InGaAs/InP	Surface Normal	1.55	3.6	2	NR	NR	20	[51]
InGaAs/InAlAs	Surface Normal	1.55	1.5	1.5	NR	5 Mbps	6	[52]

Chapter 3

Electroabsorption Modulator Development

3.1 Material Selection and Epitaxial Design

3.1.1 EAM Quantum Well and Barrier Material Selection

To enable both data communication and power generation, appropriate material selection for the EAM is critical. As both the PV device and the EAM are absorption-based devices, selecting materials with optical transparency in mind is vital. Additionally, to enable high quality epitaxial growth, it is desired to have the material be lattice matched to a commercially available substrate. Figure 3.1 shows the lattice constant versus bandgap for commonly grown III-V semiconductors, with a line drawn at 1.55 μm. $In_{0.53}Ga_{0.47}As$, henceforth referred to as 'InGaAs', is lattice matched to InP, a commonly available starting substrate, lies close to the 1.55 μm line. As a result, InGaAs was selected as the QW material.

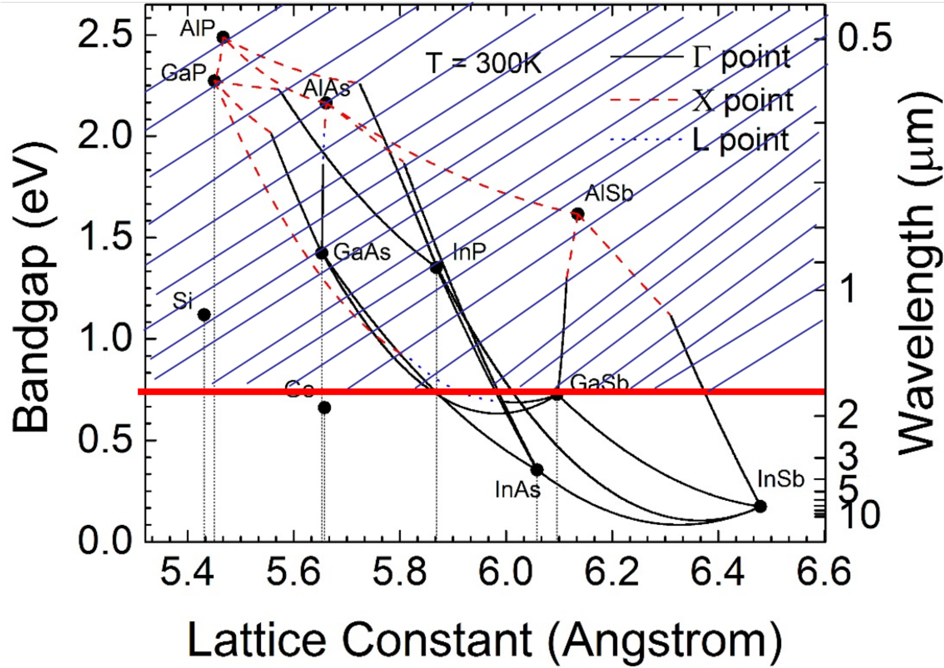

Figure 3.1: Lattice constant versus bandgap for commonly grown III-V semiconductors. A line is drawn at 1.55 μm to denote the desired laser communication wavelength. The region above the line represents materials that are optically transparent to 1.55 μm and can be used for collection of solar energy.

For a wider bandgap barrier material, both InP ($E_g = 1.34$ eV) and $In_{0.52}Al_{0.48}As$ (1.50 eV) (lattice matched to InP), henceforth referred to as 'InAlAs', were investigated. InP, while more straightforward to grow, suffers from a very poor interface with the InGaAs QW due to the Group V precursor switch [53]. When etched in concentrated hydrochloric acid (HCl), it becomes evident that there is roughening at the interfaces between the InP and InGaAs, shown in Figure 3.2 (right). Additionally, there is incompatibility in etching As-based and P-based compounds [54]. InP etches rapidly, at a rate of 6.5 μm/min. HCl, however, is selective and does not etch InGaAs. Generally speaking, the mechanism by which As-based compounds are etched requires an oxidizing agent, such as hydrogen peroxide (H_2O_2), which oxidizes the surface. That oxide is then removed with a strong acid, such as phosphoric acid (H_3PO_4). It is hypothesized that etching the InP/InGaAs

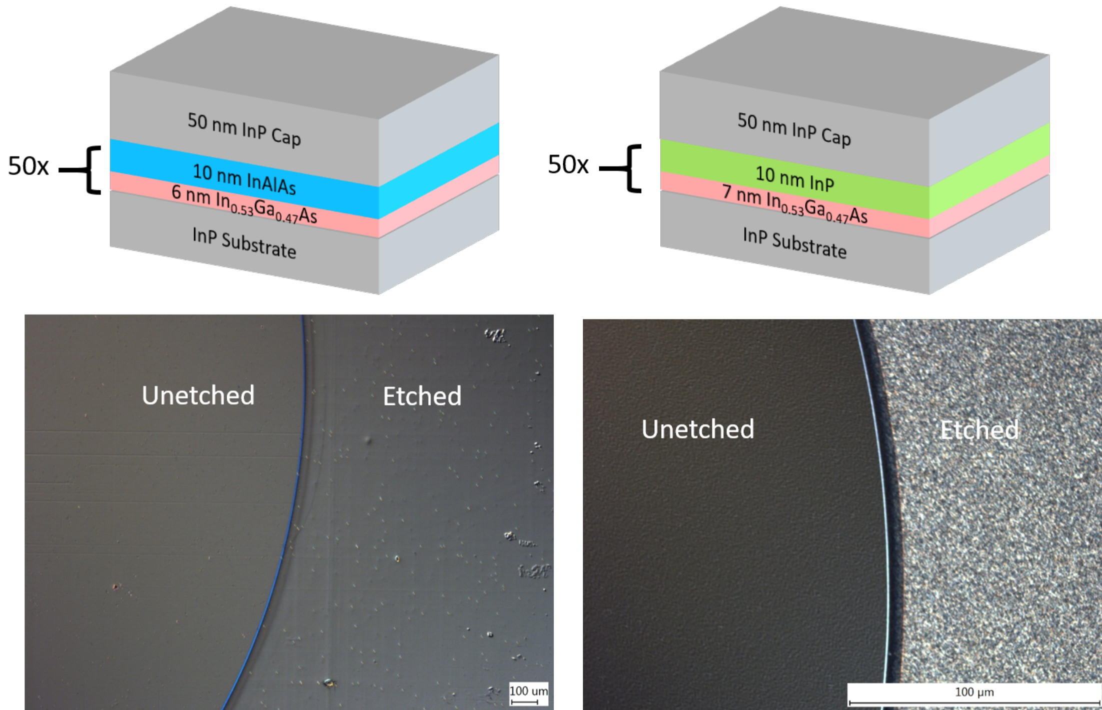

Figure 3.2: Top Left: Illustration of a test structure of 50 repeats of InGaAs/InAlAs
Bottom Left: InGaAs/InAlAs test structure etched in 1:1:38 H_2O:H_2O_2:H_3PO_4
Top Right: Illustration of a test structure of 50 repeats of InGaAs/InP
Bottom Right: InGaAs/InP test structure etched in concentrated HCl.

test structure in HCl was accomplished by the aggressive etching of the InP effectively ripping away at the QW layers.

Switching to InAlAs as a barrier material removes the Group V precursor switch, resulting in a much smoother interface [53]. Additionally, InGaAs and InAlAs etch at the same rate in hydrogen peroxide:phosphoirc acid based solutions. When etched in 1:1:38 H_2O:H_2O_2:H_3PO_4, a smooth surface is revealed, shown in Figure 3.2 (right). As a result, InAlAs is the preferred barrier material for the EAM.

3.1.2 Lateral Conduction Layer Design

For integration with a PV device and to allow transmission of 1.55 μm light through the entire device a lateral conduction layer is required for the back contact of the EAM. This is opposed to traditional fabrication of PV devices which utilize the entire back of wafer as the contact, which results in low series resistance. Material selection of the lateral conduction layer is important to limit insertion loss of the modulator. The absorption of 1.55 μm of undoped InGaAs, InAlAs, and InP through 50 nm of material is shown in Figure 3.3.

This InGaAs layer parasitically absorbs approximately 5 % of the incident 1.55 μm light, or approximately 10 % after two passes, as shown in Figure 3.3. Alternative, wider bandgap, lattice-matched materials are $In_{0.52}Al_{0.48}As$ and InP, which are completely transparent to 1.55 μm light. InP was selected as the material for the n-type LCL due to ease of growing homoepitaxial material and ease of achieving high doping concentrations in this layer.

To improve the rate at which data can be modulated, and correspondingly transmitted to and from the hybrid PV/EAM device, increasing the cutoff frequency is paramount. Very high n-type doping of InP can be achieved using tellurium (Te) as the dopant [55]. As resistance is inversely related to the cutoff frequency of a device, a thick, highly doped LCL is desired for high cutoff frequency. This, however, is in tension with reduction of parasitic absorption due to free carrier absorption in the lateral conduction layer. Wavelength dependent free carrier absorption can be calculated by the method described by Bulashevich *et al.,* [56]:

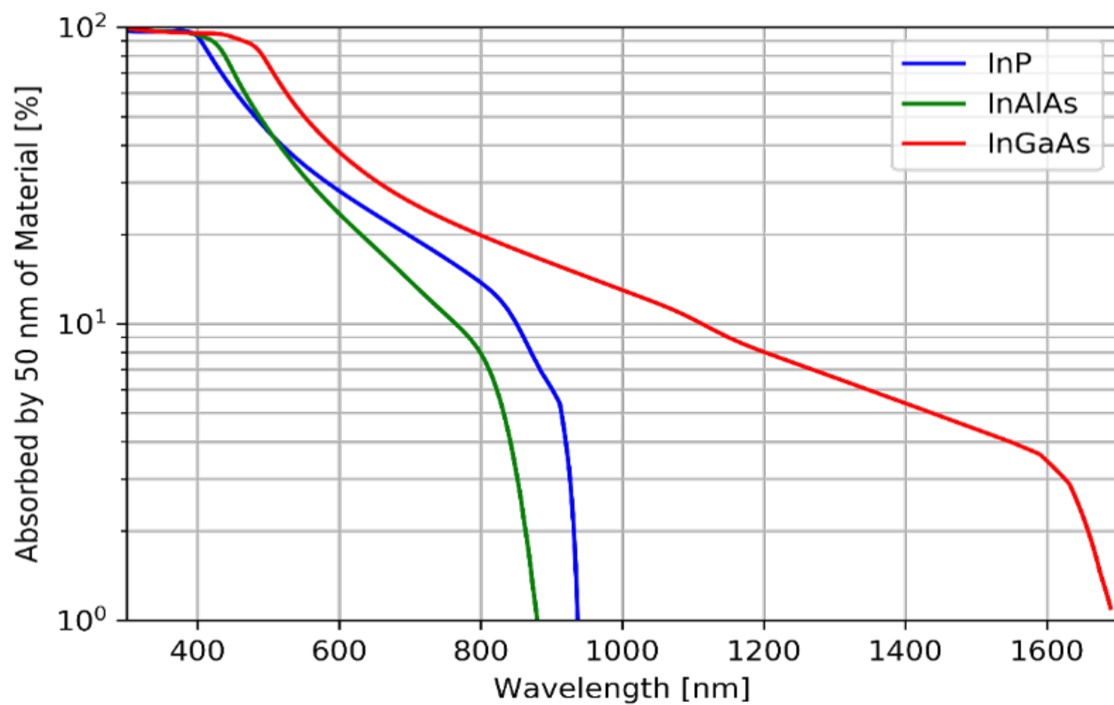

Figure 3.3: Percent absorbed light through 50 nm of material for InGaAs, InAlAs, and InP by wavelength.

$$\alpha = \frac{q^3\lambda^2 n}{4\pi^2\mu m^2 N_r \epsilon_0 c^3} \tag{3.1}$$

Where α is the absorption coefficient, q is the elementary charge, λ is the wavelength, μ is the mobility, m is the effective mass, N_r is the refractive index, ϵ_0 is the permittivity of free space, and c is the speed of light. From absorption coefficient, the transmission of 1.55 μm light can be found by the Beer-Lambert Law:

$$Transmission(\lambda = 1.55\mu m) = exp(-\alpha(\lambda = 1.55\mu m) * t_{LCL}) \tag{3.2}$$

Where t_{LCL} is the thickness of the lateral conduction layer. For a layer of InP doped to 8 x 10^{19} cm^{-3} (the highest measured doping for InP doped with Te for a sample measured at RIT), the transmission versus wavelength for various thicknesses is shown in Figure 3.4. As thickness of the highly doped layer increases, the transmission at 1.55 μm begins to drop below 95 % after only 100 nm. If the doping were to be lowered to 7 x 10^{18} cm^{-3}, the thickness of the layer can be increased to 2500 nm before transmission drops to 99 %, as shown in Figure 3.5.

To balance the need for both high cutoff frequency and low free carrier absorption, a dual-layer LCL is employed, with a thicker, lower doped carrier transport layer and a thin, very highly doped capping layer for low contact resistance. For a cap doping of 8 x 10^{19} cm^{-3} and a bulk layer doping of 7 x 10^{18} cm^{-3}, the cutoff frequency for a 1 cm^2 device was determined using a simplified 1D resistance model that models carrier transport both vertically and laterally through the device. The model is shown in Figure 3.6, outlining the different resistive components of the dual-layer LCL.

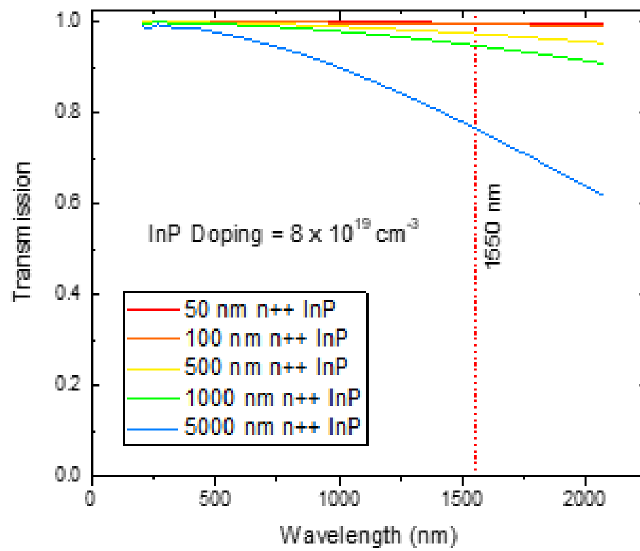

Figure 3.4: Transmission versus wavelength for various thicknesses of InP with doping levels of 8 x 10^{19} cm^{-3}.

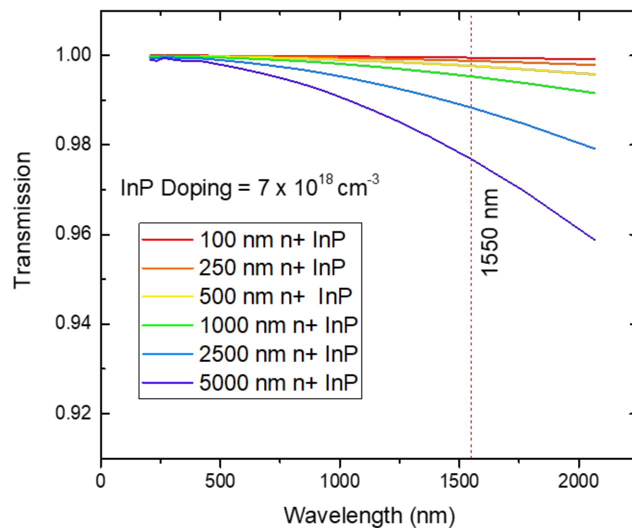

Figure 3.5: Transmission versus wavelength for various thicknesses of InP with doping levels of 7 x 10^{18} cm^{-3}.

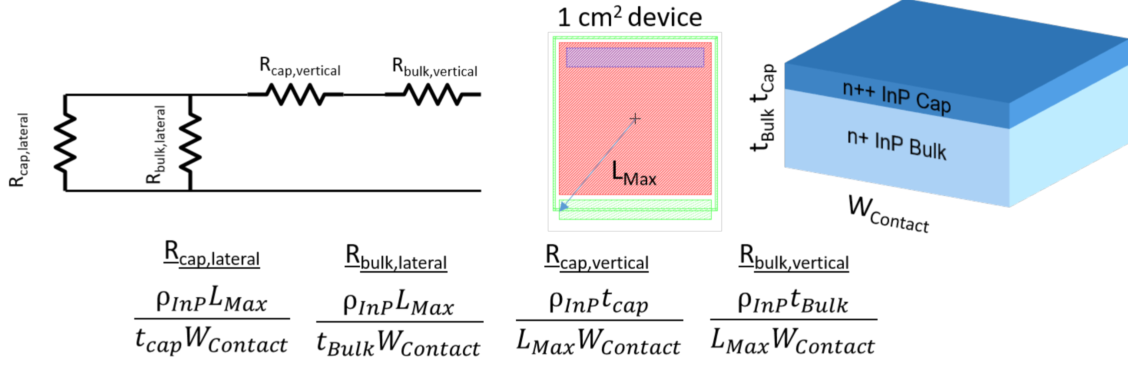

Figure 3.6: Dual-layer LCL model used to determine the resistive components of the LCL for calculating cutoff frequency, showing the cell area for a 1 cm^2 EAM.

The lumped resistance for the circuit shown in Figure 3.6 is given by:

$$R = \left(\frac{1}{\frac{\rho_{InP} L_{Max}}{t_{cap} W_{Contact}}} + \frac{1}{\frac{\rho_{InP} L_{Max}}{t_{Bulk} W_{Contact}}} \right)^{-1} + \frac{\rho_{InP} t_{Cap}}{L_{Max} W_{Contact}} + \frac{\rho_{InP} t_{Bulk}}{L_{Max} W_{Contact}} \tag{3.3}$$

Where ρ is the doping dependent resistivity, L_{Max} is the maximum distance carriers need to travel in a 1 cm^2 device to be collected, t_{cap} is the thickness of the highly doped cap, t_{bulk} is the thickness of the bulk LCL layer, and $W_{Contact}$ is the width of the contact. Varying t_{cap} and t_{bulk} the cutoff frequency can be determined. A capacitance of 14 nF was assumed as this was the value experimentally determined from previous measurements. The parameter space is shown in Figure 3.7.

To balance the need for high cutoff frequency and low free carrier absorption, a thicknesses of 50 nm was selected for the 8 x 10^{19} cm^{-3} cap and 500 nm for the 7 x 10^{18} cm^{-3} LCL bulk.

Contact resistance is also a critical parameter in ensuring high cutoff frequency. For a smaller, 0.25 cm x 0.25 cm device, where the resistive component of the LCL would be

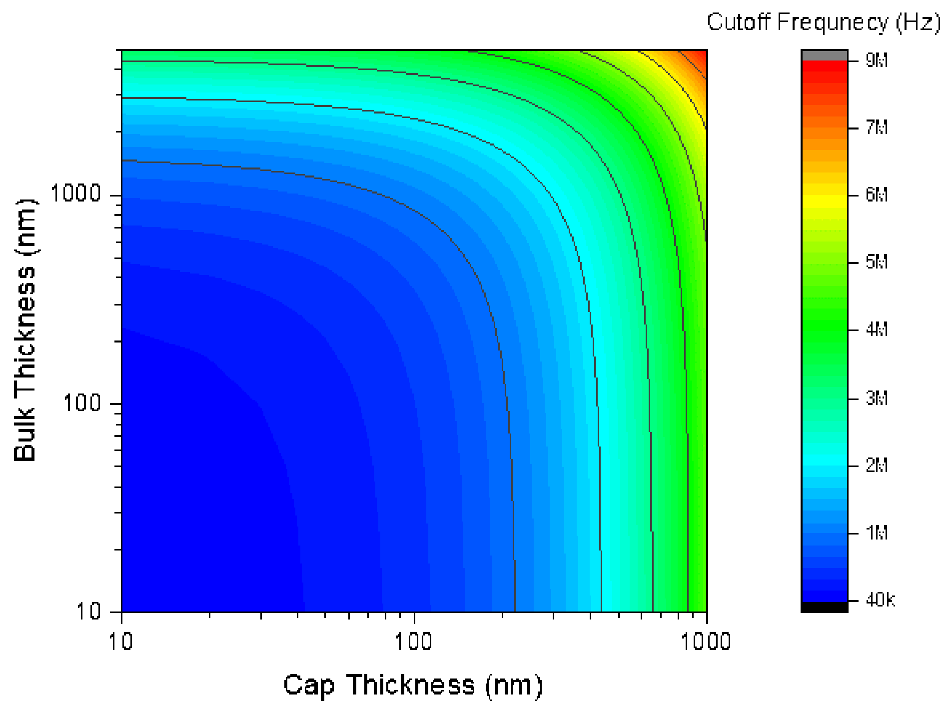

Figure 3.7: Parameter space for cutoff frequency of a 1 cm^2 EAM for varied LCL bulk and capping layer thicknesses.

smaller due to the reduced distance carrier need to travel, the effect of contact resistivity on the cutoff frequency is larger. For a 0.25 x 0.25 cm device, the cutoff frequency begins to decrease precipitously at contact resistivities greater than 10^{-5} Ω-cm^2.

To ensure excellent contact to the InP LCL, a study of different metallizations, anneal temperatures, and anneal times were investigated on n++ InP. A test structure of 50 nm 8 x 10^{19} cm^{-3} cap and 500 nm for the 7 x 10^{18} cm^{-3} LCL bulk to emulate the modulator contact layer. This doping was verified by Hall Effect measurements. Three metallization schemes were tested: Ge (25 nm) /Au (50 nm) /Ni (25 nm); Ge (25 nm) /Au (50 nm) /Ni (25 nm) / Au (200 nm); and Au0.88Ge0.12 (300 nm) / Ni (70 nm) / Au (200 nm). Each was subjected to a tube-furnace (N_2 ambient) anneal at temperatures from 300 °C to 400 °C and times from 90 to 210 seconds. Figure 3.9 shows the change in specific contact resistance (extracted via transmission line measurements) of the different metallizations for various annealing temperatures. Here, all anneals were conducted for 90 s. Using Ge/Ni/Au yielded a specific contact resistance in the 10^{-3} Ω-cm^2 range, which would dominate the EAM RC time constant. The introduction of a gold cap improved the contact resistivity slightly. However, the introduction of a direct eutectic alloy of $Au_{0.88}Ge_{0.12}$ at the interface of the InP allowed for a significant reduction in specific contact resistance. While both of the other schemes has Au and Ge thickness in proportion to give 12 wt% of Ge, the data shows that having the direct alloy at the metal to semiconductor interface leads to a much improved contact. At a temperature of 375 °C AuGe (300 nm)/Ni (70 nm)/Au (200 nm) a contact resistivity of 4 x 10^{-6} Ω-cm^2 was obtained, shown in Figure 3.9.

The final epitaxial layer structure for the EAM for maximizing both transmission of

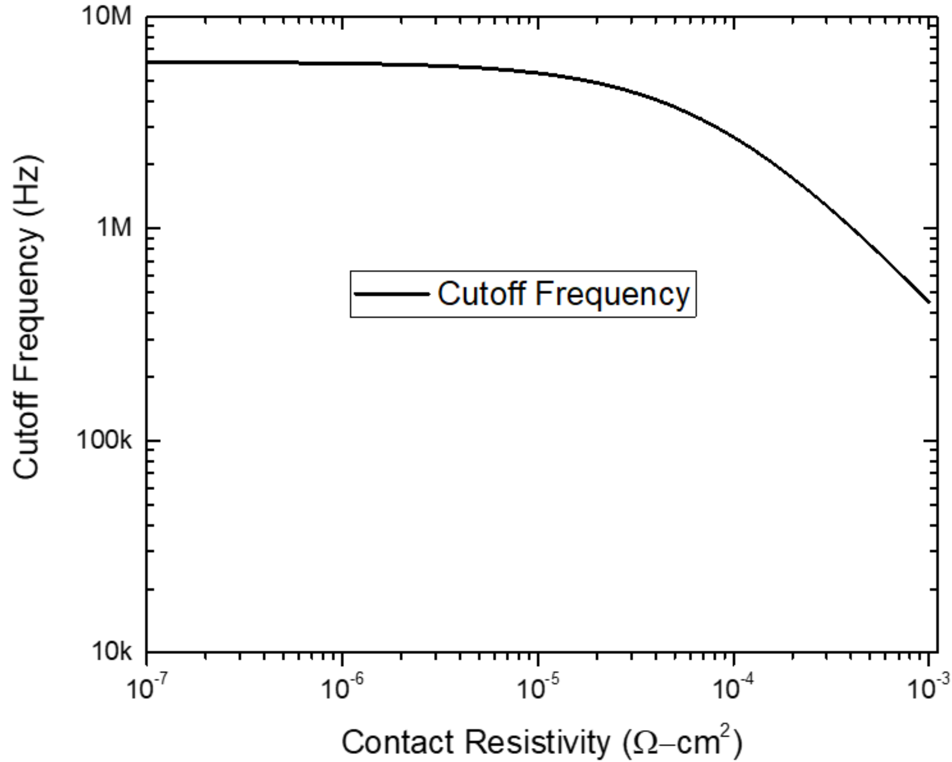

Figure 3.8: Simulated cutoff frequency versus contact resistivity for a 0.25 cm x 0.25 cm device.

1.55 μm light and cutoff frequency is shown in Table 3.1.

3.2 EAM Growth and Fabrication

3.2.1 MOVPE Growth of EAMs

The structure described in Table 3.1 was grown via metal-organic vapor phase epitaxy (MOVPE) on an Aixtron 3x2" Close-Coupled Showerhead system. Dual-side polished wafers were used to minimize transmission loss from scattering. UID substrates were required to reduce free carrier absorption. Trimethylindium (TMIn), trimethylgallium

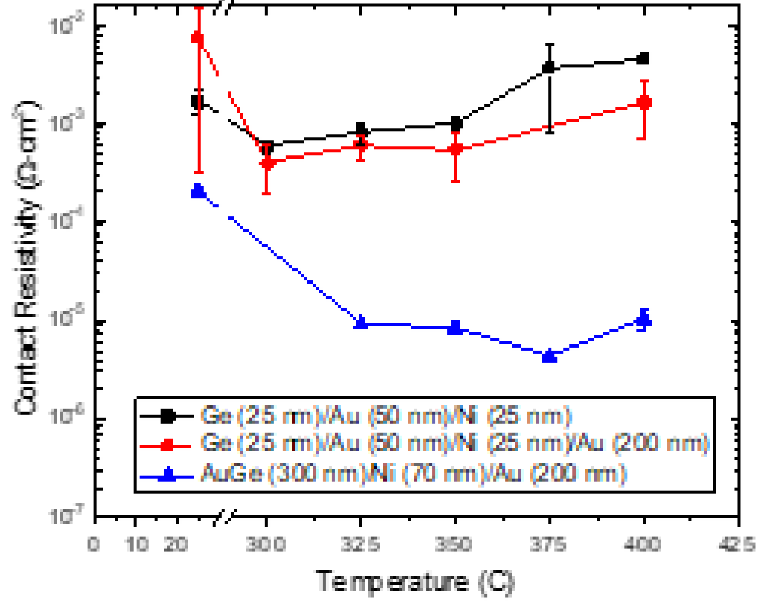

Figure 3.9: Contact resistivity versus anneal temperature for various metal stacks for contact to n-InP.

Table 3.1: Epitaxial layer structure for an EAM with optimized free carrier absorption and cutoff frequency.

Layer	**Material**	**Thickness (nm)**	**Doping cm^{-3}**	**Doping Species**
Top Contact	$In_{0.53}Ga_{0.47}As$	500	2 x 10^{19}	Zn
Etch Stop	InP	50	2 x 10^{18}	Zn
Emitter	$In_{0.52}Al_{0.48}$	500	1 x 10^{18}	Zn
MQW Region	$In_{0.52}Al_{0.48}/In_{0.53}Ga_{0.47}As$	QW pairs x [$t_{well}/t_{barrier}$]	UID	N/A
Base	$In_{0.52}Al_{0.48}$	500	1 x 10^{18}	Si
LCL Cap	InP	50	8 x 10^{19}	Te
LCL Bulk	InP	500	7 x 10^{18}	Si

(TMGa), and trimethylaluminum (TMAl) were used as the Group III precursors for In, Ga, and Al, respectively. Arsine (AsH_3) and phosphine (PH_3) were used as the Group V precursors for As and P. Diethylzinc (DEZn), disilane (Si_2H_6), and diethyltellirum (DETe) were used as the dopant sources for Zn, Si, and Te. Growth temperature was held at 620 °C for all layers, with the exception of the p-type InAlAs, which reduced the growth temperature to 600 °C for improved surface morphology. A V/III ratio of 158.5 was maintained for InP growth, 60 for bulk InGaAs growth, and 26.7 and 6.8 for n-type and p-type InAlAs, respectively.

For growth of the MQW region, arsine flow was maintained at 20 sccm for the entire MQW region growth. To form the InGaAs and InAlAs wells and barriers, the TMIn flow was fixed to the same value and was flowing the entire time. TMGa and TMAl were toggled on and off for the well and barrier growths (TMGa on, TMAl off for the InGaAs well growth, TMGa off, TMAl on for the InAlAs barrier growth) and were set to lattice match each material at growth temperature. Lattice mismatch (f) is defined as:

$$f = \frac{a_S - a_L}{a_L} \tag{3.4}$$

where a_S is the lattice constant of the substrate, and a_L is the lattice constant of the grown layer. For f < 0, the lattice constant of the grown layer is greater than that of the substrate, resulting in a compressive strained film. For f > 0, the lattice constant of the grown layer is smaller than that of the substrate, resulting in a tensile strained film. For pseudomorphic growth, that is, growth in which the film is grown below the critical thickness [57], strain is assumed to all be in the perpendicular direction ($\epsilon_\perp$), defined as:

$$\epsilon_{\perp} = -2\frac{C_{12}}{C_{11}}f \tag{3.5}$$

where C_{11} and C_{12} are the stiffness coefficients in the x-direction and xy-direction. For measuring lattice mismatch at growth temperature, the curvature of the wafer is measured *in situ* using a LayTec EpiCurveTT monitoring system. To obtain strain from curvature, the film stress (σ_f) can be calculated from curvature (k) by using the Stoney formula:

$$k = \frac{6h_f\sigma_f}{M_s h_s^2} \tag{3.6}$$

Where h_f is the film thickness, h_s is the substrate thickness, and M_S is the substrate biaxial modulus. From the calculated stress, the film strain (ϵ_f) can be calculated by:

$$\epsilon_f = \frac{M_f}{\sigma_f} \tag{3.7}$$

For run to run consistency and to eliminate strain and stress as a variable when comparing data sets, lattice matched QWs were defined as ± 100 ppm of strain at growth temperature, and all EAMs discussed in this chapter and subsequent chapters meet this criteria.

3.2.2 Fabrication of EAMs

A mask was designed for the EAMs to test multiple EAM sizes and to provide the ability to integrate with a PV device. The mask design is shown in Figure 3.10 shows

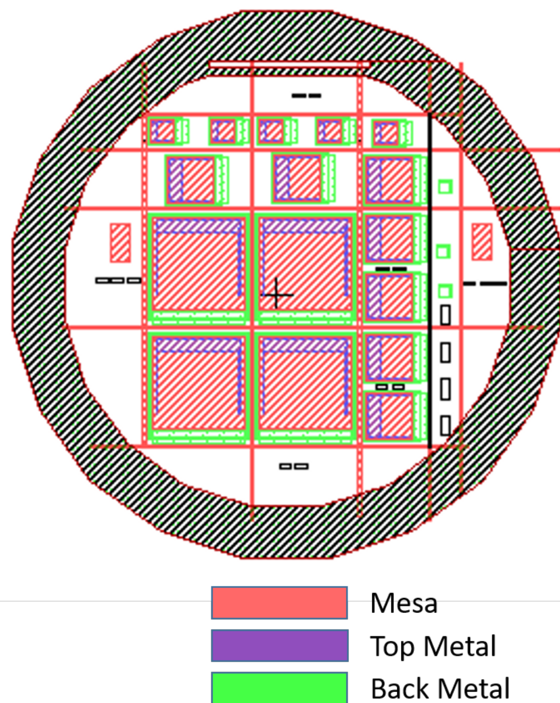

Figure 3.10: Left: Mask design of the EAMs.
Right: Photograph of fully fabricated EAMs.

the photomask layout. Modulator areas were selected to be 1 cm^2, 0.25 cm^2, and 0.625 cm^2. Each modulator was designed to have a corresponding PV device that could be integrated for a hybrid PV/EAM device, which will be discussed in Chapter 4. The mask was designed to be a top-top design due to the need for the laser to pass through the entire device. This necessitated the need for the development of a low insertion loss, low resistance lateral conduction layer discussed previously.

EAMs were fabricated with the following process. Metal contact was made to the p++ InGaAs top contact via evaporation of 500 nm of Au using a liftoff procedure. The InGaAs contact was then removed from the field of the device through a self-aligned etch in 1:1:10 H_3PO_4:H_2O_2:H_2. The devices were then mesa isolated, using concentrated HCl for InP and 1:1:10 H_3PO_4:H_2O_2:H_2 (selective against the InP LCL) for the InAlAs barriers

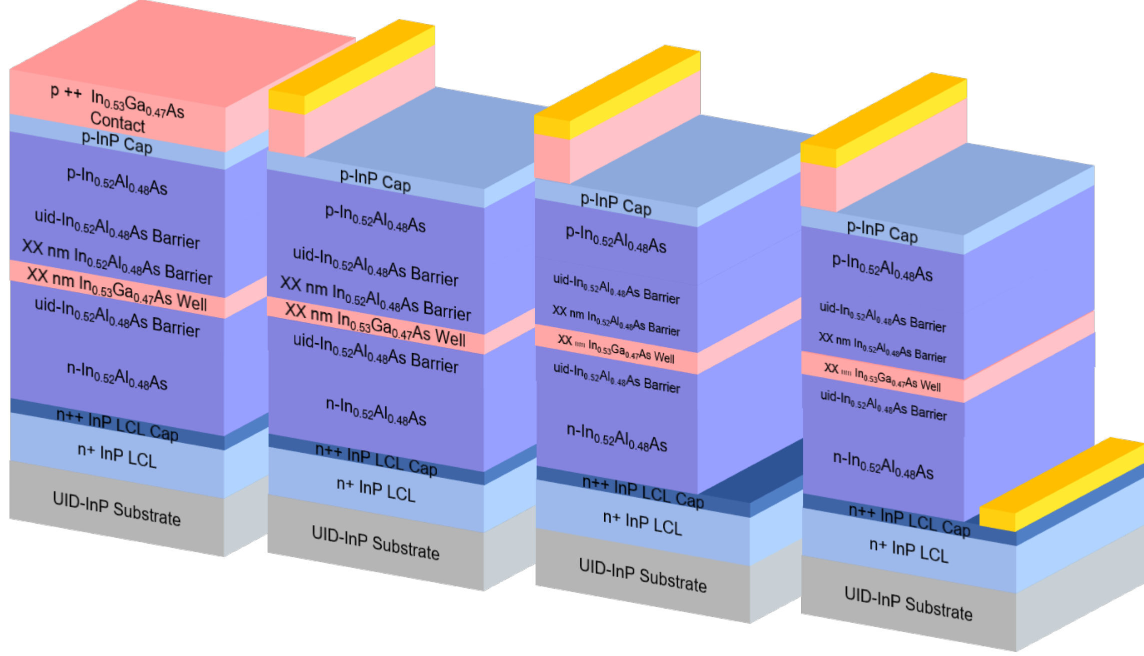

Figure 3.11: Fabrication procedure for the EAM.

and the MQW region. Metal contact was made to the n++ InP LCL via evaporation of AuGe (300 nm)/Ni (70 nm)/Au (500 nm). Similar to the top InGaAs contact, this also used a liftoff process. The EAMs were annealed for 90 s at 375 °C in an N_2 environment. The full process flow is illustrated in Figure 3.11, and fully fabricated devices are shown in Figure 3.10.

3.3 Quantum Well Thickness Study

3.3.1 Lumerical Workflow

Initial simulations of a multiple quantum well (MQW) electroabsorption modulator (EAM) have been conducted. The goal was to develop an initial working model for InP-based EAMs in order to investigate the design space with respect to parameters

such as quantum well and barrier thickness and material selection. Simulations were conducted in Ansys Lumerical, a multi-physics photonic design suite. The solvers used were:

- MODE: An eigenmode analyzer that provides the modal properties of the light propagating through the structure.
- CHARGE: A three-dimensional Poisson/drift-diffusion solver which provides results for electrical, thermal, and optical inputs. This module provides the electric field across the MQW region.
- MQW: A quantum well gain simulator which utilizes a 4 x 4 band k p model for solving for the absorption coefficient as a function of applied electric field for the structure.

Using the described workflow, a square quantum well (SQW) EAM with 10 nm $In_{0.53}Ga_{0.47}As$ wells and 10 nm $In_{0.52}Al_{0.48}As$ barriers was simulated (structure shown in Figure 3.12). Two pairs of wells/barriers were simulated to reduce simulation time, and to simulate the effect of a 1 micron thick QW region, the calculation for the contrast ratio parameter set the QW region thickness to 1 micron. This assumes that each well contributes equally across a 1 micron thick modulation region. The change in the overlap in the wave function is not dependent on the number of repeats of wells, rather, it is dependent upon the total thickness of the intrinsic region and the resulting electric field. The total thickness of the MQW region can be modeled by unintentionally doped (uid) layers. To accurately model the electric field drop across a 1 μm thick MQW region,

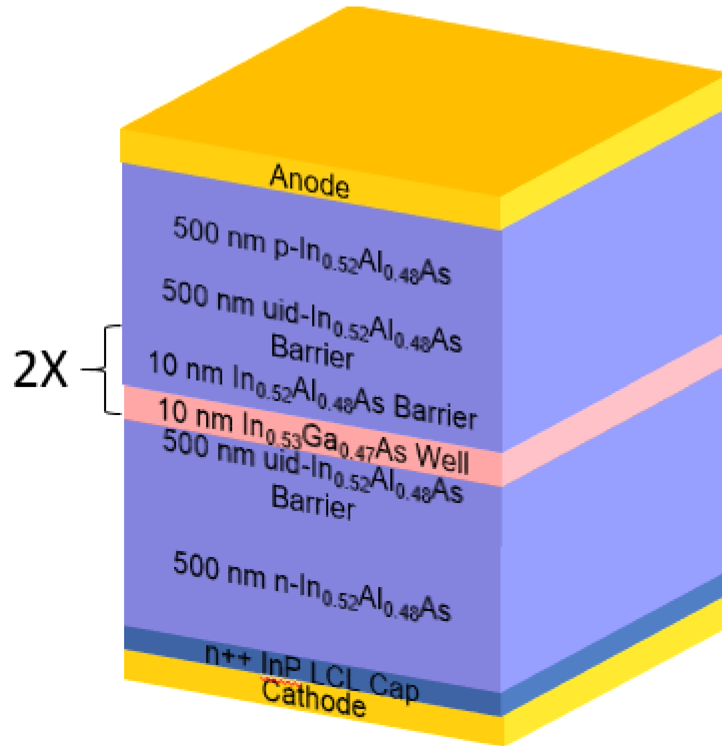

Figure 3.12: Illustration of the structure used for simulations in Lumerical.

500 nm thick InAlAs p and n regions were included on either side of the MQW region to drive the electric field.

Figure 3.13 shows the extracted electric field across the MQW region for the structure under 0 V bias (blue) and -10.25 V bias (green) as simulated in the CHARGE solver. The electric field was solved from 0 V to -10.25 V in steps of 0.25 V. Unbiased, the electric field in the MQW region is approximately 10 kV/cm, and in the biased case it is approximately 90 kV/cm. These values for electric field were imported into the MQW gain solver.

Figure 3.14 illustrates the absorption coefficient calculated by Lumerical's MQW solver as a function of applied bias (and, by extension, the applied electric field) for an example structure. Due to the quantum confined Stark effect (QCSE) there is a

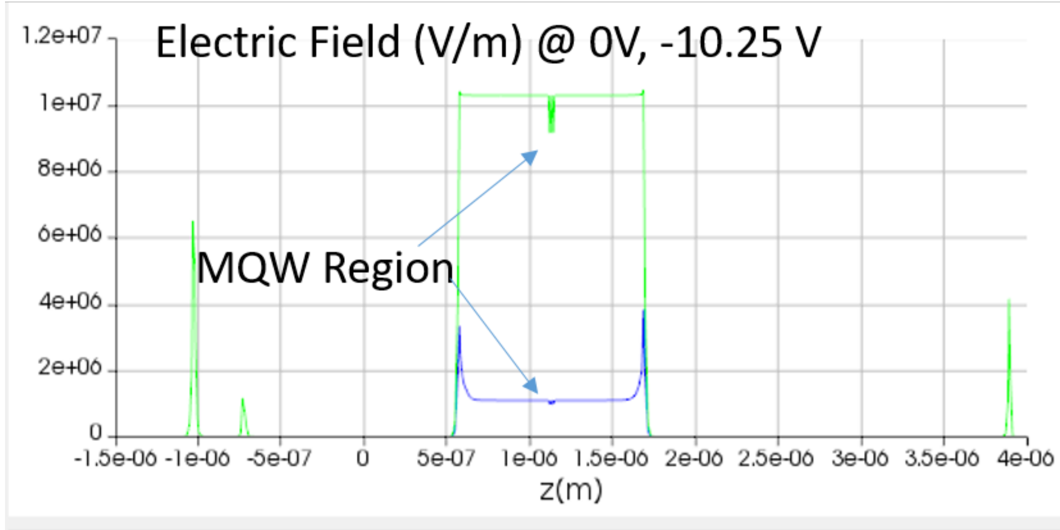

Figure 3.13: Extracted electric field for 0 V (blue) and -10.25 V (green) using the CHARGE solver.

pronounced red shift in the absorption coefficient when an external bias is applied.

Using the extracted change in absorption coefficient, the contrast ratio, calculated by Equation 2.12, can be determined. For the example structure, the contrast ratio at -5 V and -10 V biases is shown in Figure 3.15.

3.3.2 Simulated Well/Barrier Ratio Study

Using the workflow previously described, the thickness of the InGaAs quantum wells and InAlAs barriers were varied to investigate the effect on peak contrast ratio and peak contrast ratio location. With that, the optimum configuration for an EAM with targeted operation at 1550 nm for a desired operating voltages can be derived. The well thickness was swept from 5 nm to 21 nm in steps of 1 nm, and the barrier thickness was swept from 10 nm to 21 nm, also in steps of 1 nm. The length of the MQW region was set to be 1 µm. Figure 3.16 and Figure 3.17 show the extracted, simulated contrast ratio for

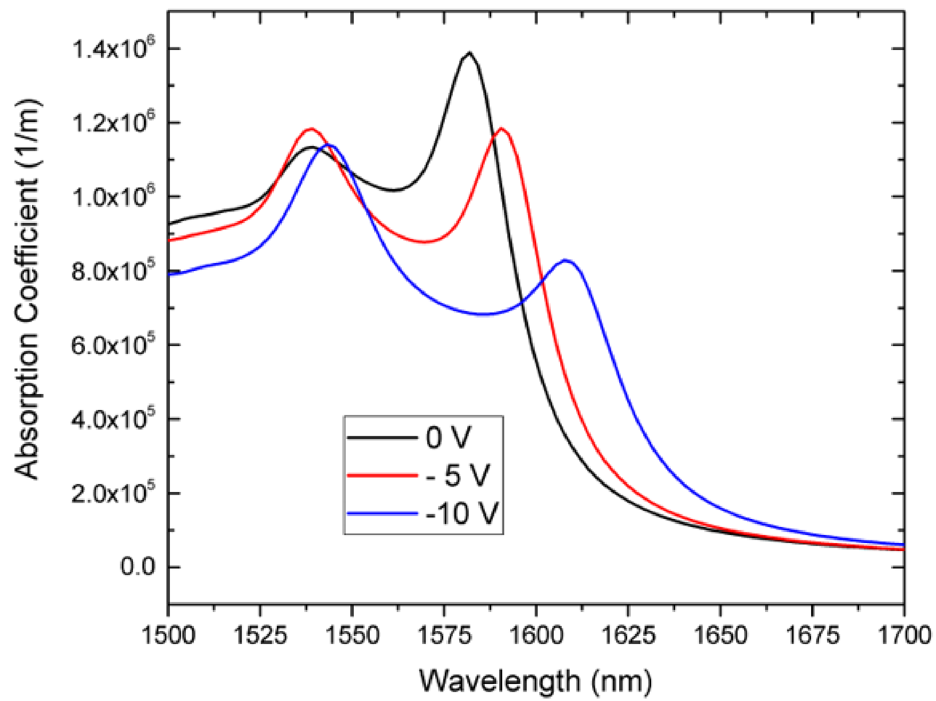

Figure 3.14: Absorption coefficient versus wavelength for the simulated Lumerical structure.

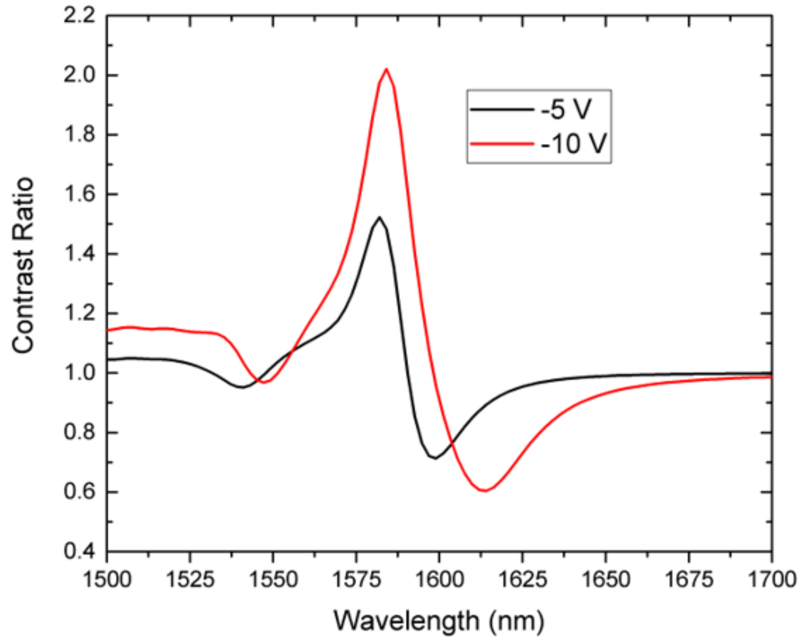

Figure 3.15: Contrast ratio versus wavelength for the simulated Lumerical structure.

an applied bias of -5 V and -10 V, respectively. As anticipated, the peak contrast ratio is higher for the EAM biased at -10 V due to a larger electric field across the MQW region, and thus a stronger QCSE resulting in a larger change in the absorption coefficient.

There is a very strong dependence of well thickness on contrast ratio; intended operating voltage also effects well thickness. For an operating voltage of -5 V, the ideal well thickness for modulation at 1550 nm is 9.5 nm, whereas for a -10 V bias the optimal thickness is 7.5 nm. Barrier thickness, however, appears to have minimal impact on contrast ratio. This, however, may be a limitation of the simulation in modeling only two pairs of MQWs.

The location of the peak contrast ratio for -5 and -10 V biases is shown in Figure 3.18 and Figure 3.19, with the range of peak contrast ratios at 1545-1555 cross-hatched

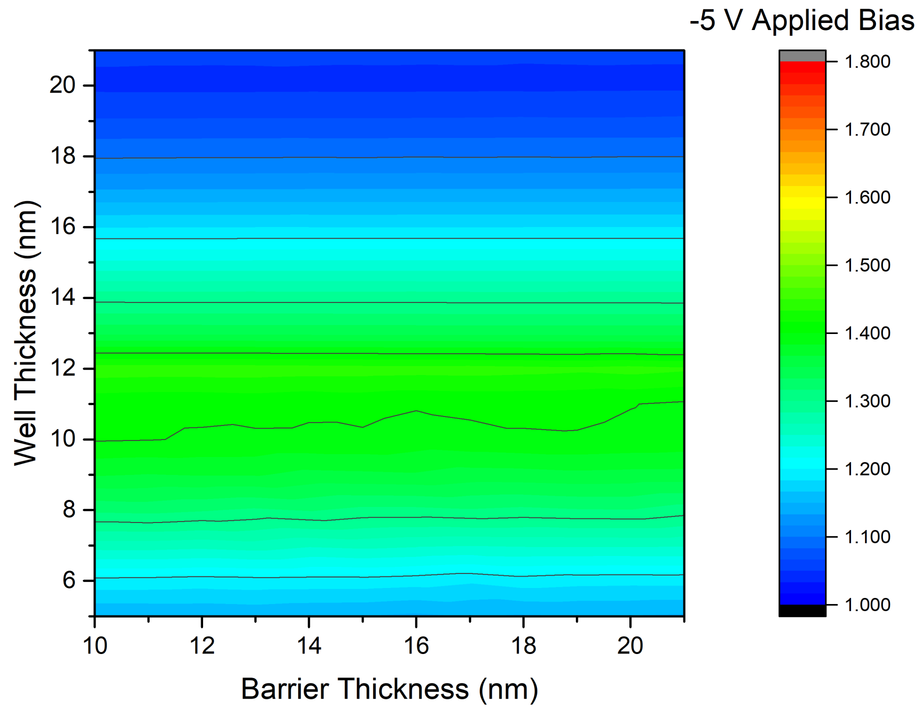

Figure 3.16: Simulated contrast ratio for varying InGaAs quantum well and InAlAs barrier thicknesses for an applied bias of -5 V

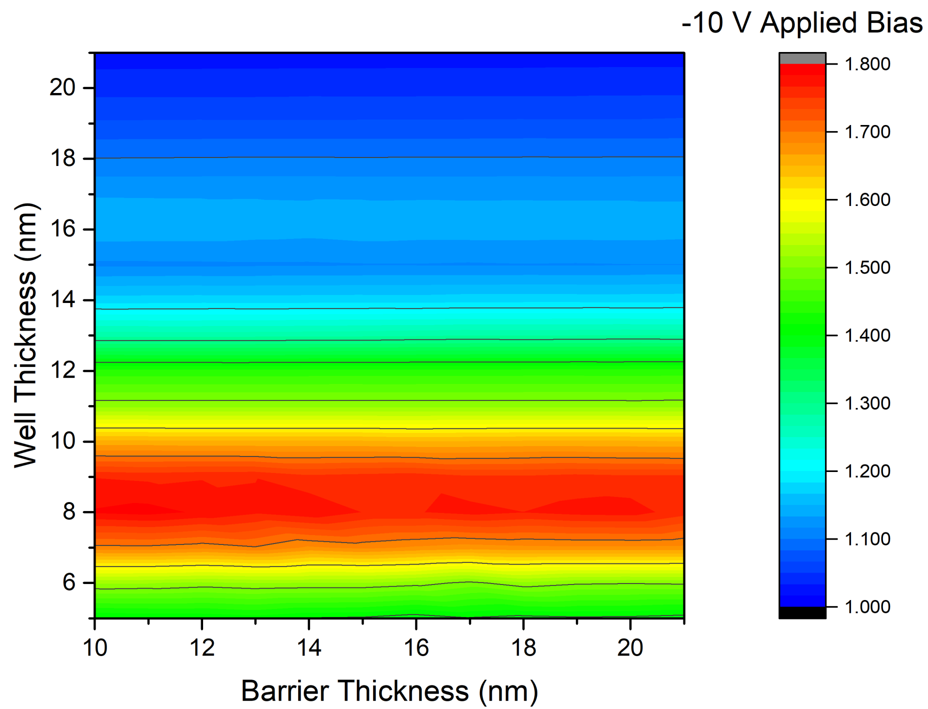

Figure 3.17: Simulated contrast ratio for varying InGaAs quantum well and InAlAs barrier thicknesses for an applied bias of -10 V

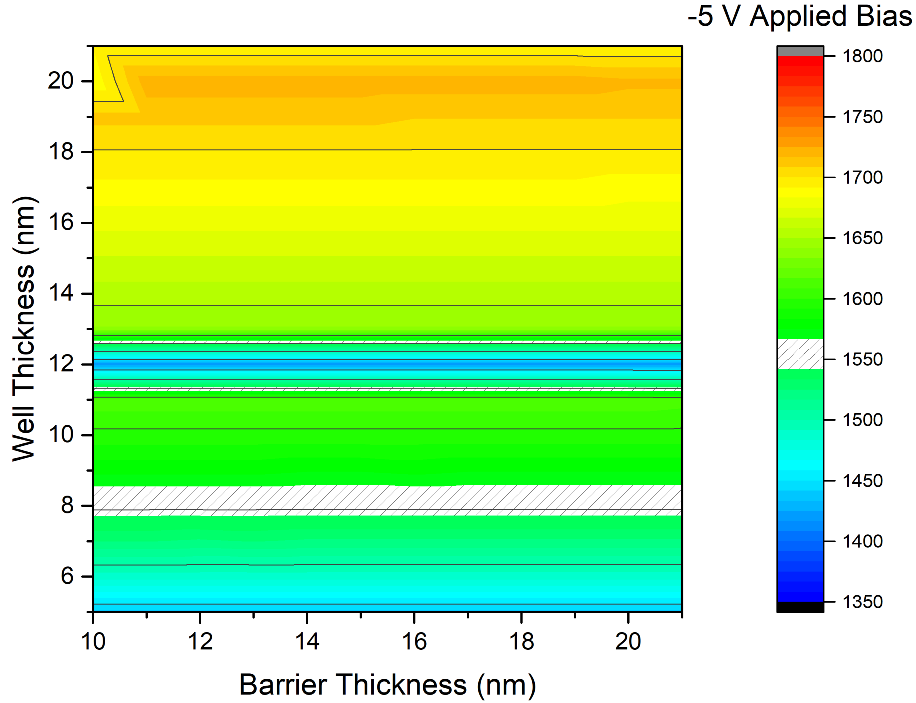

Figure 3.18: Peak contrast ratio location in nanometers for varying InGaAs quantum well and InAlAs barrier thicknesses for an applied bias of -5 V. The wavelength range of 1545-1555 nm is cross hatched.

for emphasis. For attaining a peak contrast ratio in the range of 1545-1555 nm, a well thickness of 7.8 nm is sufficient for both the -5 V and -10 V bias cases. For both biases, the well thickness is of much stronger importance than the barrier thickness, showing virtually no dependence on InAlAs barrier thickness. This, however, may be a limitation of the simulation if not enough repeats were simulated to accurately model the decay of the wave function in the barrier region of the MQW stack.

3.3.3 Experimental Well Thickness Study

3.3.3.1 EAM Well Thickness Variation

The effect of QW region thickness on ON/OFF ratio was also investigated experimentally. Based on simulated findings, the QW thickness strongly influences the peak ON/OFF

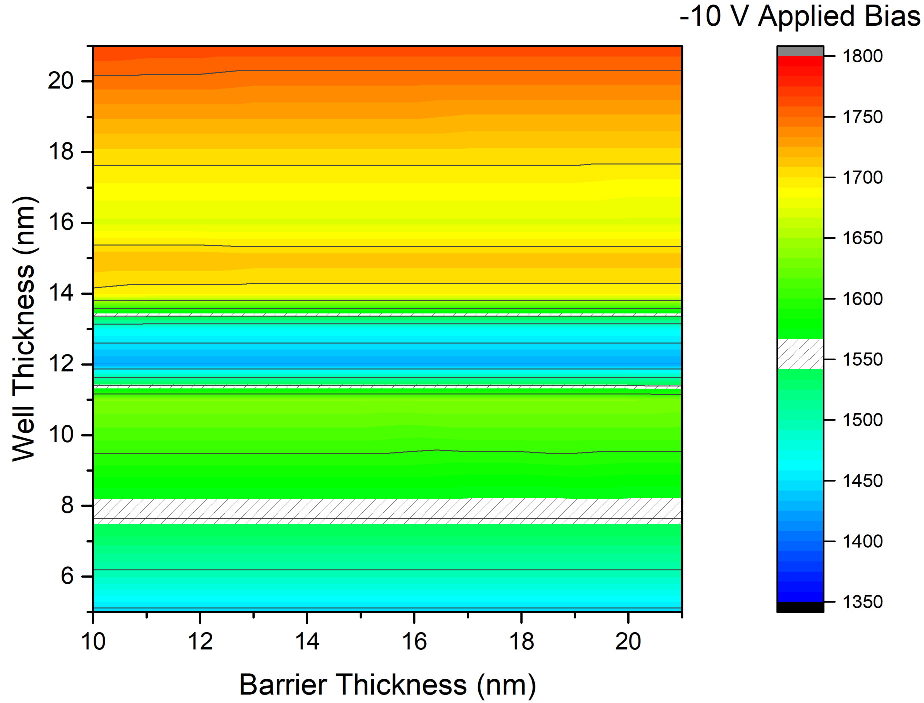

Figure 3.19: Peak contrast ratio location in nanometers for varying InGaAs quantum well and InAlAs barrier thicknesses for an applied bias of -10 V. The wavelength range of 1545-1555 nm is cross hatched.

ratio location, however the barrier thickness has minimal impact, and as a result only QW region thickness was investigated. To provide a one-to-one comparison between thicknesses and the impact on ON/OFF ratio, the thicknesses of the MQW region was held constant at 1 μm, adjusted by the number of repeats of QWs, shown in Figure 3.20.

Figure 3.21 shows the measured ON/OFF ratio for the EAMs with varied QW region thickness, and Figure 3.22 shows the peak ON/OFF ratio location dependence on QW thickness both experimentally and for simulated values at a -5 V bias. For thinner wells, the difference between the measured and simulated peak contrast ratio location narrows, and all simulation results show a red-shift in peak contrast ratio location, in line with what is expected from the QCSE [41]. The trends, however, are consistent with experimental findings. These variations are possibly due to slight differences in InGaAs

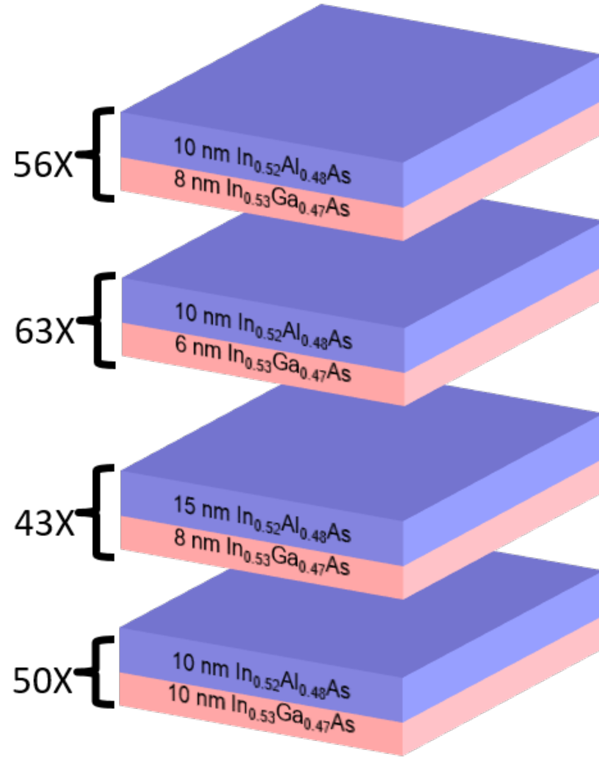

Figure 3.20: QW regions for the QW thickness study.

composition in the measured results compared to the experimental results. For an EAM with a peak ON/OFF ratio at 1550 nm, an 9 nm well according to experimental results would achieve this.

3.3.3.2 PL Test Structures

ON/OFF ratio measurements require both a several hour growth of an EAM and a full fabrication sequence in order to evaluate if the ON/OFF ratio is on target. To shorten the time required to evaluate if a given QW thickness (and to calibrate growth conditions for the QW region to be in line with the 100 ppm strain requirement specified previously), photoluminescence (PL) test structures were grown and evaluated. The epitaxial layer structure is shown in Figure 3.23. 20 repeats of a QW pair with a given well thickness

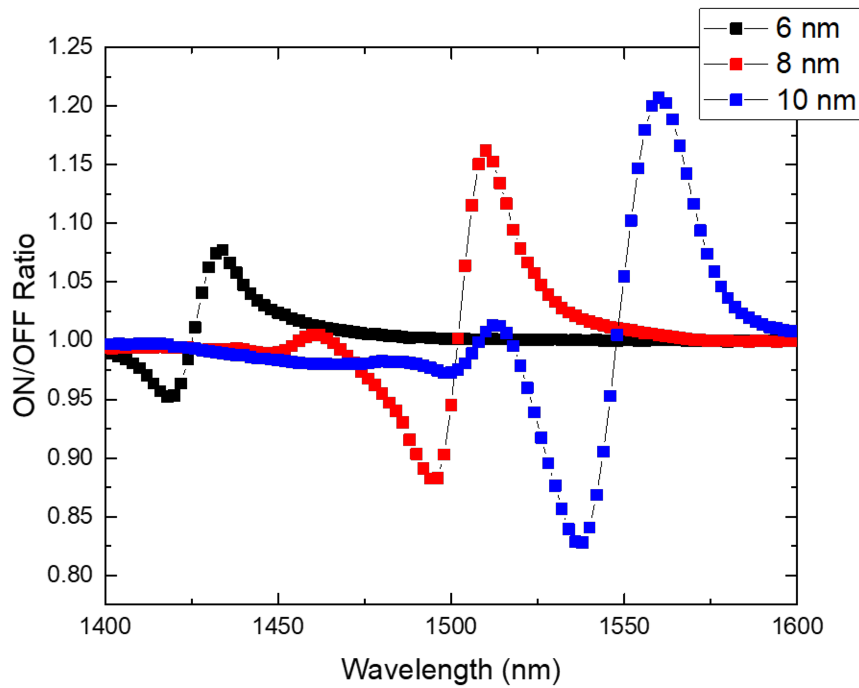

Figure 3.21: Measured ON/OFF ratio for EAMs with QW thicknesses of 6, 8, and 10 nm. All barrier thicknesses are 10 nm, and the applied bias is -5 V.

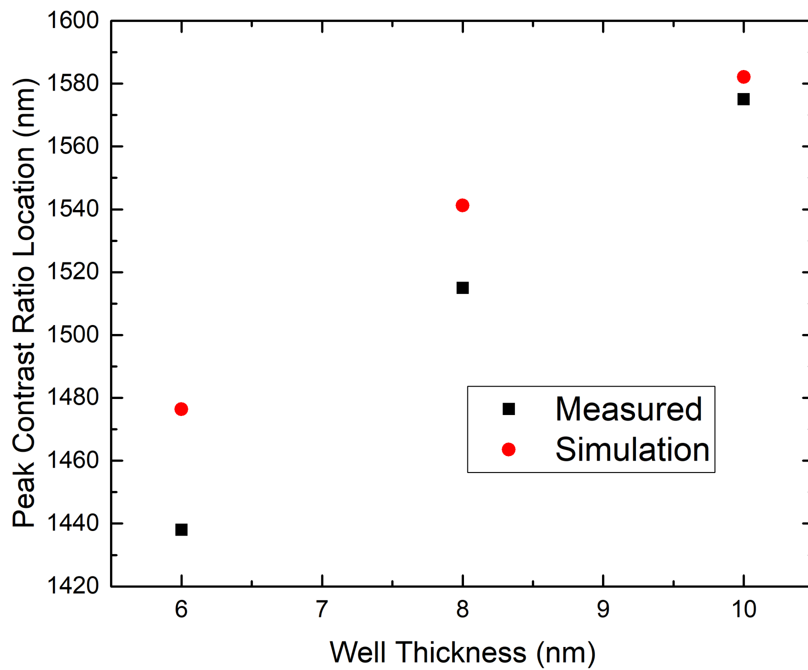

Figure 3.22: Peak contrast ratio location versus quantum well thickness for different well thicknesses via simulation and measured experimentally. The barrier thickness for 10 nm for all cases.

with a fixed, 10 nm barrier were grown. Both the InP cap and the InP buffer were undoped.

Figure 3.24 shows the measured peak ON/OFF ratio location for EAMs of different QW thickness, the PL of these EAMs, and the PL of test structures of equivalent QW thickness. The strain in all of the PL test structures was less than 100 ppm, the same as the EAMs. For both the EAMs and the PL test structures, the peak PL location red shifts with increased well thickness, similar to what was observed for the peak ON/OFF ratio location. The PL peak locations of the EAMs are red shifted compared to the PL test structures due to the built in electric field arising from the *pn*-junction of the EAM. The PL peak location for the test structures was between 8 and 20 nm shifted from the respective EAMs, with the difference reducing as well thickness increased. This difference in PL peak location is likely not from the difference in well thickness, but from a difference in overall QW region thickness in the PL test structures. Unlike the EAMs, the QW region thickness was not fixed to the same thickness, and 20 repeat units of QW/barrier pairs were grown for all PL test structures. This resulted in a reduced electric field across the QW region of the thicker test structure (10 nm) compared to the thinner QW region (6 nm), resulting in a smaller shift in the PL compared to the EAM.

When comparing ON/OFF ratio location to PL peak location, a similar red shift is observed with increasing applied voltage. The peak ON/OFF ratio location increases with an increase in applied bias due to a larger shift in the absorption coefficient (evident in the simulations shown in Figure 3.14). Generally, the peak ON/OFF ratio location of an EAM is 20-30 nm red shifted from the PL peak of a test structure. As a result, the peak ON/OFF ratio location can be roughly anticipated based on the PL of a test

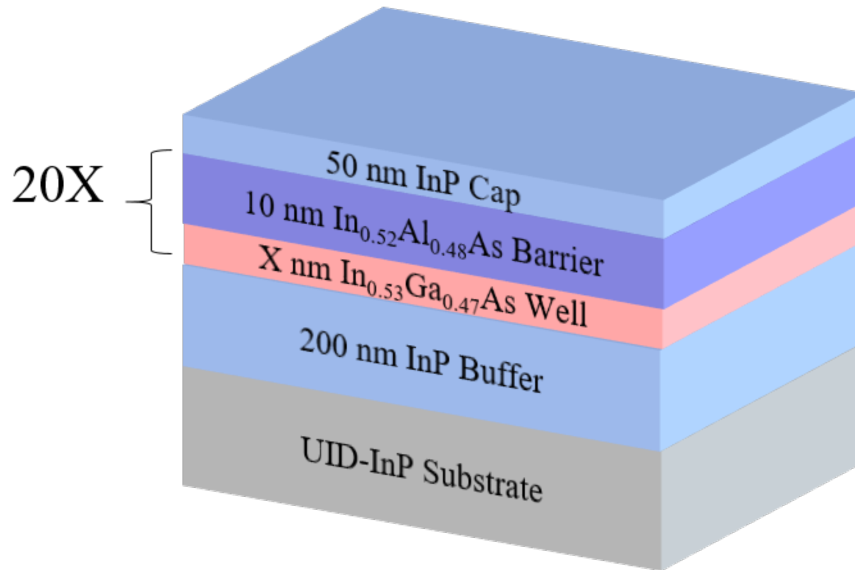

Figure 3.23: Epitaxial layer structure for PL test structures.

structure, without the need for a time-intensive EAM growth and fabrication. While hitting exactly 1550 nm is difficult, and highly sensitive to InGaAs composition and other effects such as device shunting and erroneous device heating, the peak ON/OFF ratio can be predicted well within the C-band range based on PL calibration samples.

3.3.4 Coupled Quantum Well Design

An alternative method to increase contrast ratio was to develop coupled QWs to enable carrier wavefunction overlap and separation of those states under bias. Structures shown in Figure 3.25(c,f) were modeled in nextnano, a commercial finite element Schrödinger-Poisson-drift-diffusion simulation tool, to extract transition energies at varying bias. An example of transition intensities and the delta-transmission (analogous to delta-absorption) between 0 V and -5 V bias are shown in Figure 3.25(a,b), for square QWs (SQW) and in Figure 3.25(d,e) for coupled QWs (CQW), respectively. In this

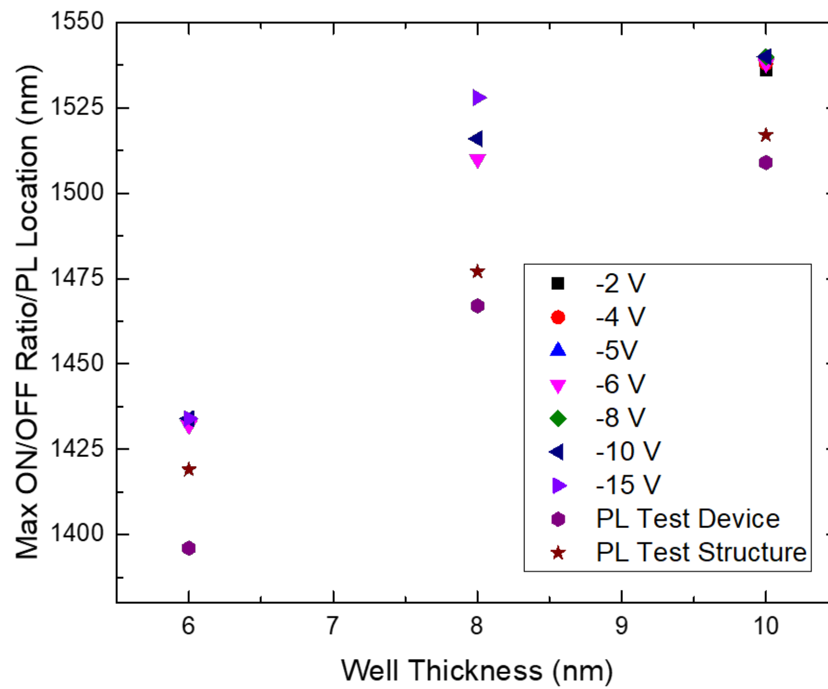

Figure 3.24: Photoluminescence and ON/OFF ratio for measured EAMs and PL test structures. The EAMs had both PL and ON/OFF ratio measured, with ON/OFF ratios being measured at voltages from -2 V to -15 V.

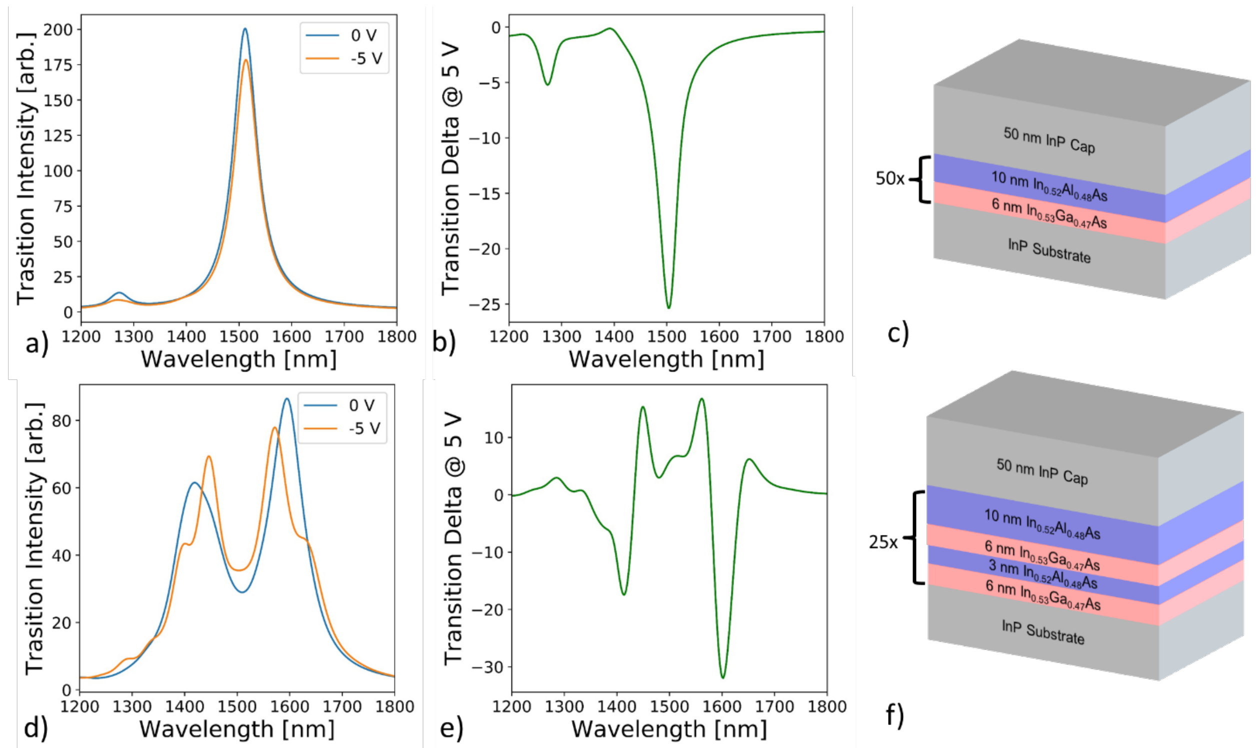

Figure 3.25: Device structures and simulated optical transition intensities for 50x MQW structures at 0 V and -5V bias, along with the change in transmission for the two designs. Top: Square QW (SQW) design. Bottom: Coupled QW (CQW) design.

particular design, the CQW design exhibits a larger peak-delta, which was expected to ultimately translate to a larger contrast ratio.

Device structures with the SQW and CQW MQW region were grown and fabricated, with the structures shown in Figure 3.26.

To evaluate the effect the SQW compared to the CQW on change in transition energies, and resulting change in absorbance as a function of voltage, voltage biased internal quantum efficiency (IQE) was measured on the SQW and CQW devices. The measured IQE was normalized and compared to the normalized IQE without biasing. In the SQW design the band edge shifts 3.2 nm/V and in the CQW design the band edge shifts 6.0 nm/V, shown in Figure 3.27 and Figure 3.28, respectively. The SQW devices compares

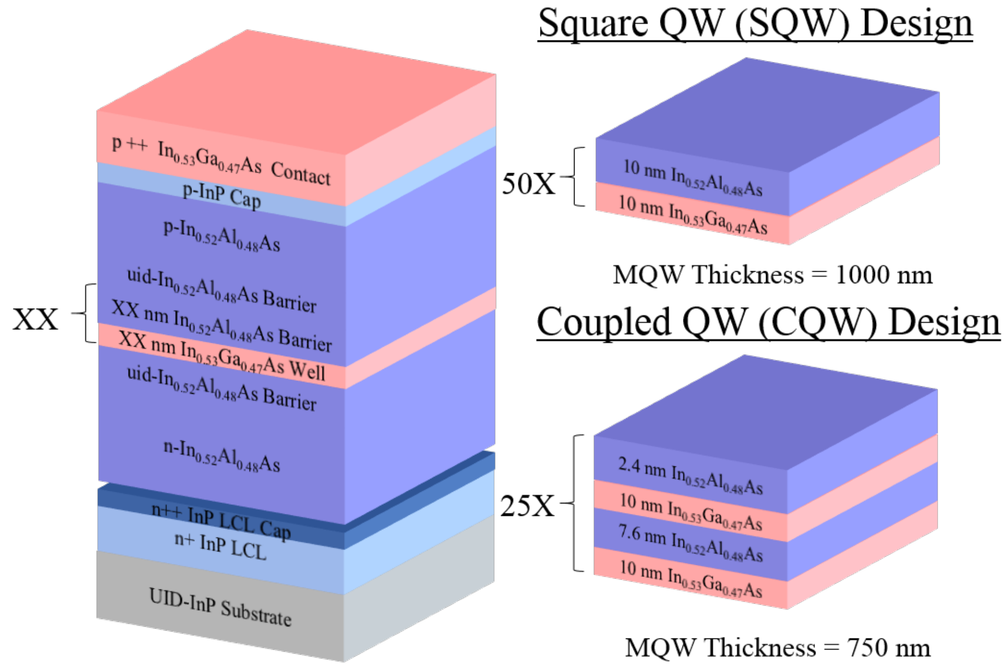

Figure 3.26: Square quantum well and coupled quantum well modulators.

well the shift in band edge observed in absorbance by Goetz et al [48] for a similar SQW InGaAs/InAlAs design at 2.0 nm/V. The CQW design demonstrates a very strong shift in band edge compared to the SQW design at 6.0 nm/V, and this is due to a stronger quantum confined Stark effect in the CQW device.

3.4 Bandwidth and Cutoff Frequency

The operational electronic switching speed of the modulators of varied device size was also investigated by capacitance-voltage measurements using a dedicated Agilent B1500A semiconductor device analyzer. A DC-bias of -3V was applied and the small signal applied voltage had a peak-to-peak voltage of 50 mV. Analyzing the system as a low-pass filter, the output voltage was found using:

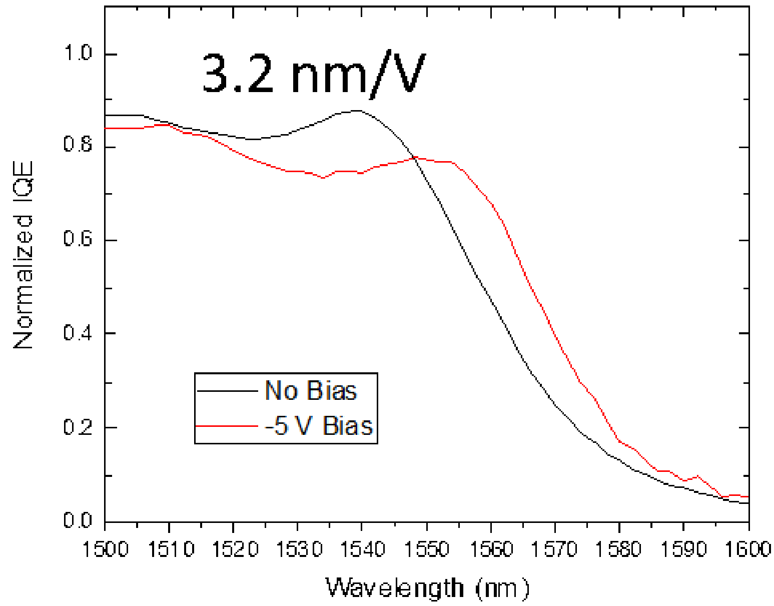

Figure 3.27: Voltage biased IQE of a SQW EAM.

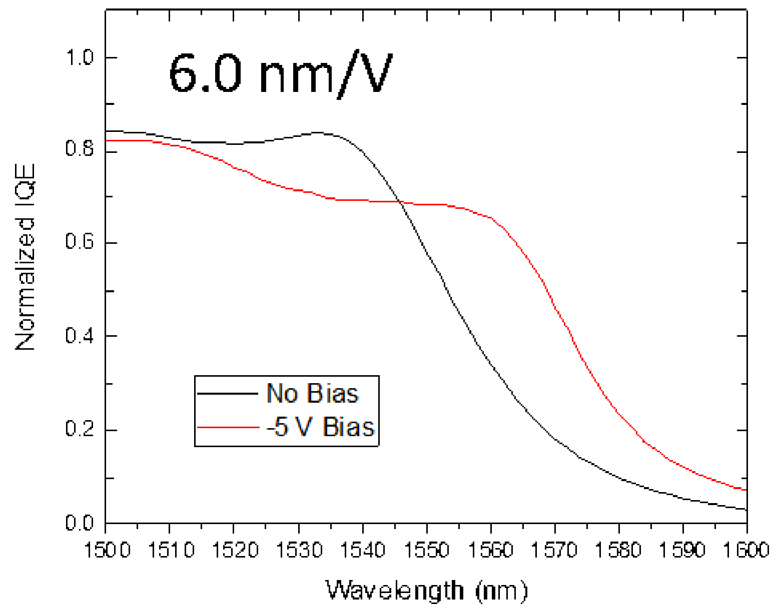

Figure 3.28: Voltage biased IQE of a CQW EAM.

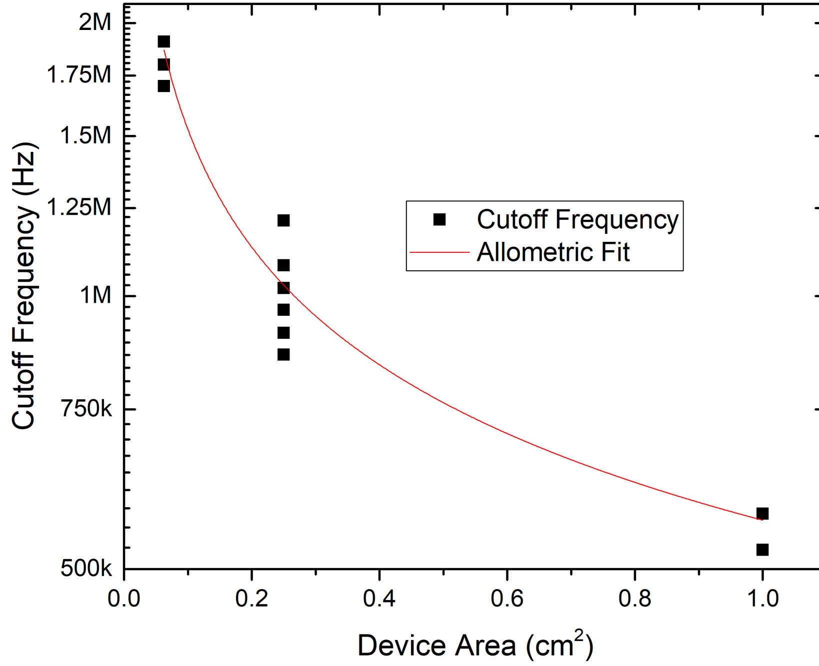

Figure 3.29: Cutoff frequency versus device area for EAMs

$$V_{Out} = V_{In} \frac{X_C}{Z} \tag{3.8}$$

where X_C is the capacitive reactance of the device and Z is the impedance. The gain is calculated using:

$$Gain(dB) = 20log_{10} \frac{V_{Out}}{V_{In}} \tag{3.9}$$

and the cutoff frequency, f_c, corresponds to the frequency at which the magnitude of the gain is equal to 3 dB, corresponding to a decrease in the maximum device response of 50 %. The smallest devices demonstrate a cutoff frequency of, on average, 1.5 MHz. The largest devices exhibit a cutoff frequency of approximately 600 kHz. The 3 dB cutoff frequency is related to the device capacitance (C) and resistance (R) by Equation 2.13.

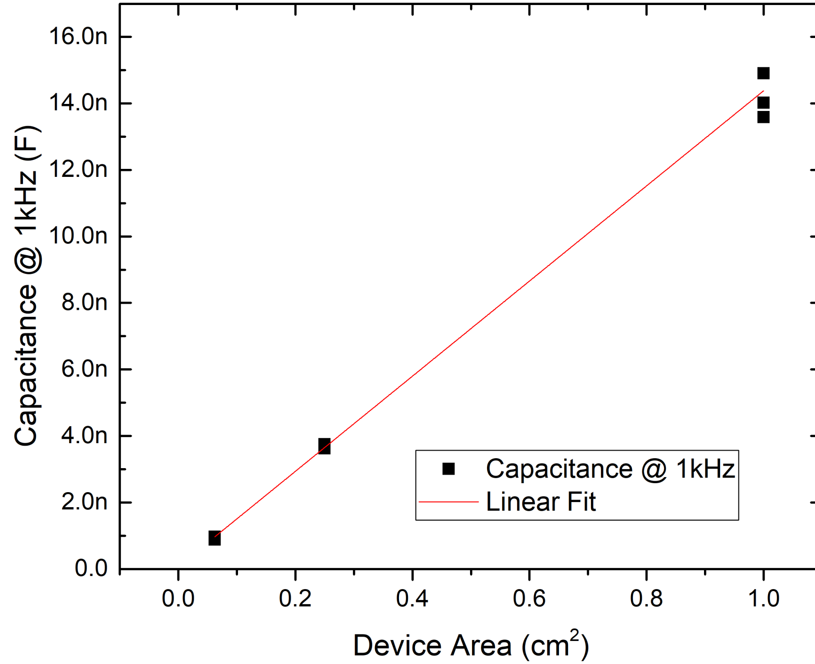

Figure 3.30: Capacitance versus area for EAMs of varied size.

Here, the 3 dB cutoff frequency is dominated by the device capacitance, which is inherently driven by the device area. Modeled as a parallel plate capacitor, the capacitance of the modulators as they depend on area (A) and the thickness of the MQW region (t_{MQW}) is given by:

$$C = \frac{\epsilon A}{t_{MQW}} \tag{3.10}$$

Where ϵ is the relative permittivity of the material. As area increases, the capacitance increases linearly, and this was experimentally verified, shown in Figure 3.30.

3.5 Summary of Section

Significant effort has gone in to the development of an electroabsorption modulator that can be integrated with a PV device. Materials for the QW region (InGaAs and InAlAs) were selected to simplify growth and fabrication while maintaining competitive ON/OFF ratios compared to literature reported values. Figure 3.31 shows the ON/OFF ratio for EAMs reported in this section compared to other surface normal EAMs reported in the literature. The ON/OFF ratio, however, is directly dependent on the length of the modulating region. Figure 3.32 shows the ON/OFF ratio normalized by MQW region thickness, which shows the be reported performance below 5 V to date.

It is evident that devices reported in this section excel at low voltage operation compared to those previously reported. This low voltage operation is the target operation region as in an ideal case, the EAM would be driven directly by the integrated PV device, and such the voltage range of interest is sub-5 V operation. Additionally, device breakdown frequently occurred at voltages greater than -10 V, irrespective of device size. Higher voltage operation was not heavily explored in these devices because of this intended operation, however it is reasonable to assume that with minor modifications (such as sidewall passivation to limit sidewall shunts that could lead to device breakdown) these devices would also excel at higher voltage operations.

With an EAM, the modulation scheme used is on-off keyeing (OOK), which is a form of amplitude shift keying (ASK), in which the amplitude of a signal provides the data '1' and data '0'. Using OOK as the modulation scheme, the cutoff frequency can be directly correlated to the maximum data rate possible for a given device. The corresponding

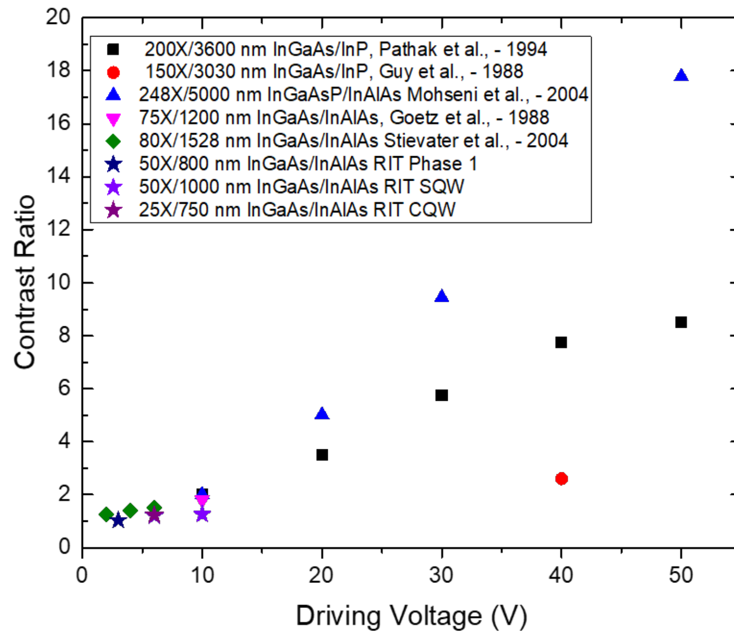

Figure 3.31: ON/OFF ratio comparison to literature reported values.

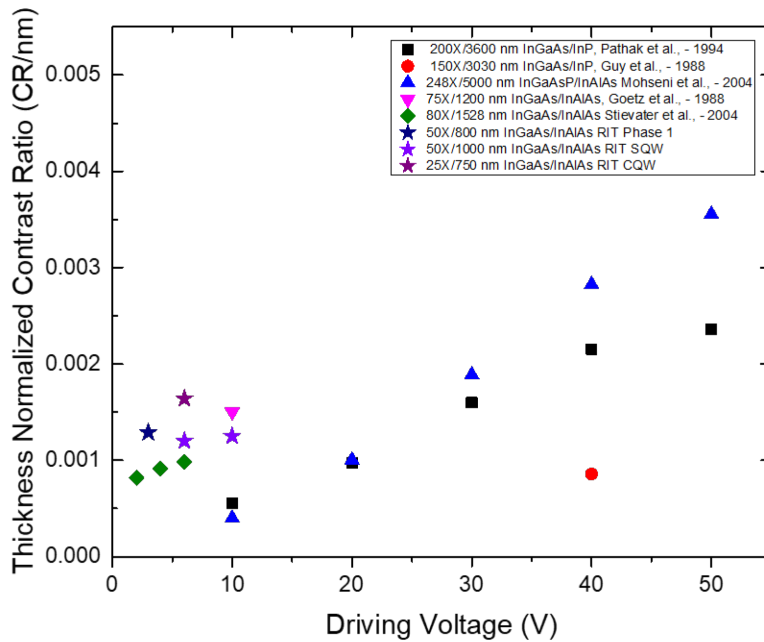

Figure 3.32: QW region thickness normalized ON/OFF ratio comparison to literature reported values.

data rates based on the Shannon-Nyquist theorem for the measured EAMs range from 0.3 to 0.9 Mbps. This is still two orders of magnitude below what was demonstrated by the Laser Communication Relay Demonstration due to the capactive limitations of the surface normal EAMs, that device was not optimized for hybrid use with a PV device, and the previously mentioned EAMs can be further optimized with a segmented design (discussed in later chapters) [58].

Chapter 4

Mechanically Stacked Hybrid Device

The development of an electroabsorption modulator presented in Chapter 3 was then used to realize a hybrid, PV/EAM device. One avenue for integrating a PV device with an EAM is to mechanically stack them and create a four terminal device. By having the PV device completely separate from the EAM, it eliminates the restriction of having to use InP as the substrate for the power generating device. InP-based multijunction photovoltaics have been looked into extensively for their potential AM0 efficiency of 37 % for a lattice matched triple junction [59]. This design, however, struggles from the difficulty in growing a suitable, low defect, high quality top junction [60, 61, 62, 63]. Specifically, Sb-containing compounds that would result in a 1.8 eV, lattice-matched material is prohibitively difficult to grow [64]. Having the growth of the EAM separate from the growth of the PV device circumvents this difficulty, and the more developed multijunction technologies grown on GaAs can be used.

This chapter discusses the development of two mechanically stacked designs - one being a single EAM integrated with a single junction PV device in a 1 cm^2 form factor, and the other being a 0.5 U form factor mini-module that integrates multiple EAMs

with multiple dual junction, InGaP/GaAs PV devices. This work was done in parallel effort with the EAM optimization described in Chapter 3, and further, improved upon mechanically stacked devices could be developed using findings from that chapter.

4.1 Single Cell Integration

4.1.1 Growth and Fabrication of Single Cell Hybrid Device

To meet the needs for the hybrid PV/EAM device the mask design for the hybrid device work was done to develop a design that could be mechanically bonded while leaving both devices operational for both discrete and conjoined operation. The modulators were designed using the mask design discussed in Chapter 3. PV device sizes were selected to be 0.75 cm^2, 0.15 cm^2, and 0.0375 cm^2. This allowed for the PV device to be nested atop the modulator while retaining ability to contact all four terminals. Three mask levels were required for each device, resulting in six discrete mask layers. The final mask design for the PV device is shown in Figure 4.1.

The *nip* GaAs solar cell had an active absorber region of 4 μm. The front surface window was $In_{0.53}Al_{0.47}P$ and the back surface field, which also acts as the p-type back contact, was $Al_{0.70}Ga_{0.30}As$. The n-type top contact was highly doped GaAs doped to 3×10^{19} cm^{-3}. Metal contact was made to the solar cell using standard electroplating procedures. Cell areas were defined via mesa isolation in a chemistry of H_2O_2:H_3PO_4:H_2O (3:4:1) and the InAlP window and InGaP etch stops were removed in HCl. The n+ GaAs contact was removed in a solution of NH_4OH:H_2O_2:H_2O (1:1:50). The process flow is

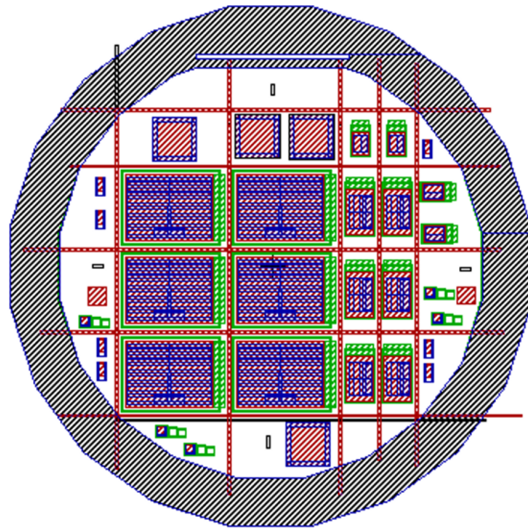

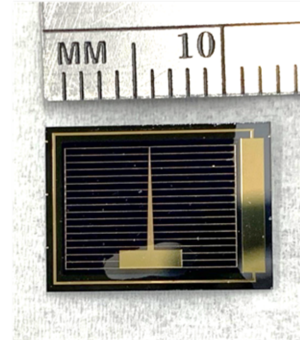

Figure 4.1: Left: Mask design of the GaAs PV devices for integration. The red is the mesa isolation, the blue is the top metal, and the green is the back contact.
Right: Photograph of a fully fabricated GaAs PV.

shown in Figure 4.2 (a). A bilayer anti-reflection coating of 50 nm ZnS/ 100 nm MgF_2 to enhance GaAs absorption was thermally evaporated in a Kurt Lesker PVD 75A system. Calculated reflection loss at 1.55 μm is approximately 35% as determined by the optical software TFCalc with an ARC. The design target for this device was 22 % based on previously fabricated devices with this structure.

This modulator was designed and grown prior to the lateral conduction layer optimization and well thickness study conducted in Chapter 3. For the modulator, 50 repeats of 6 nm InGaAs wells and 10 nm InAlAs barriers formed the MQW region and a highly doped p-InAlAs and n-InAlAs were grown on either side of the MQW structure to drive the electric field, with thicknesses and doping levels specified in Chapter 3. Contacts to the modulator were made using both p-type and n-type InGaAs. The p-type and n-type metal contact (Au) was made to the modulator via thermal evaporation in a Kurt Lesker

PVD 75 system using a liftoff photolithography technique. Devices were mesa isolated in a solution of 1:1:38 H_2O_2:H_3PO_4:H_2O. The InP etch stops were removed in HCl:H_3PO_4 (1:1). The process flow is shown in Figure 4.2 (b). It is important to note that this EAM did not use the InP lateral conduction layer described in Chapter 3, this EAM uses a 50 nm thick n-InGaAs layer. While contacting this layer is straightforward, with evaporated Au serving as a low contact resistance metallization solution as compared to the more complicated AuGe/Ni/Au metallization required for low resistance ohmic contact to n-InP, this InGaAs layer parasitically absorbs at 1550 nm.

4.1.2 Discrete Device Testing

4.1.2.1 1J GaAs PV Testing

Post-fabrication, the GaAs PV device was tested for AM0 illuminated current-voltage characteristics. An efficiency of 19.53 % was measured. The GaAs PV device demonstrated an open circuit voltage of 1.03 V, indicating excellent material quality, high shunt resistance, and low reverse saturation current, as implied by Equation 2.4. A primary reason why the efficiency is lower than the target efficiency of 22 % is due to the top-top contact design of the GaAs PV device. Metal cannot be deposited on the back of the GaAs wafer as this would prevent transmission of 1.55 μm light through the PV device to the modulator. As a result, a top-top contacting scheme was necessary, requiring the use of a lateral conduction layer (LCL). This LCL inherently imparts more series resistive losses compared to a conventional top-back. The AlGaAs LCL for the GaAs PV device was doped to 2 x 10^{19} cm^{-3} to give a sheet resistance of 6.6 x 10^{-7} Ω/square. The

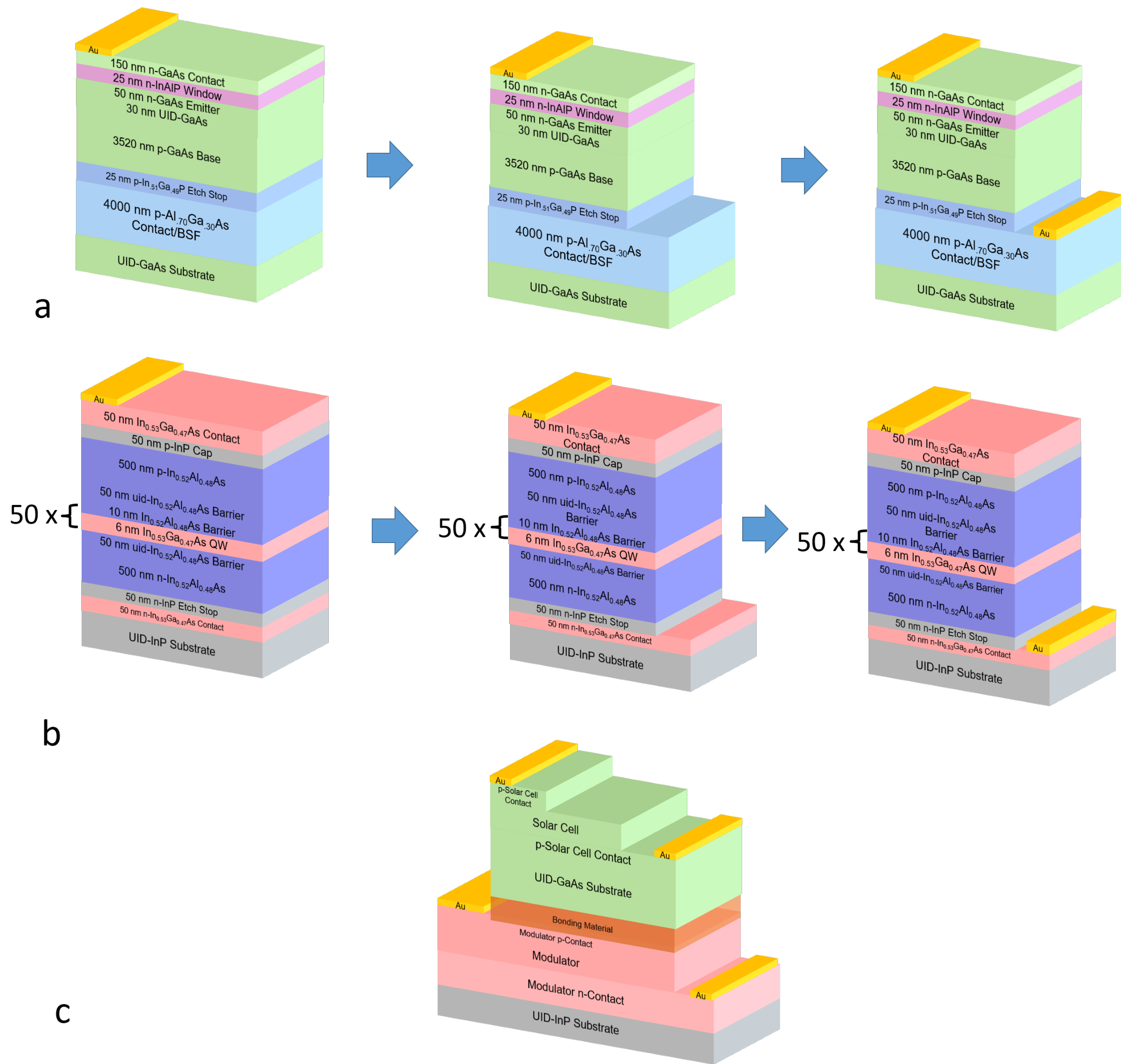

Figure 4.2: a: Process flow for the GaAs PV device for the mechanically stacked hybrid device.
b: Process flow for the InGaAs/InAlAs EAM for the mechanically stacked hybrid device.
c: Illustration of mechanically stacked hybrid device.

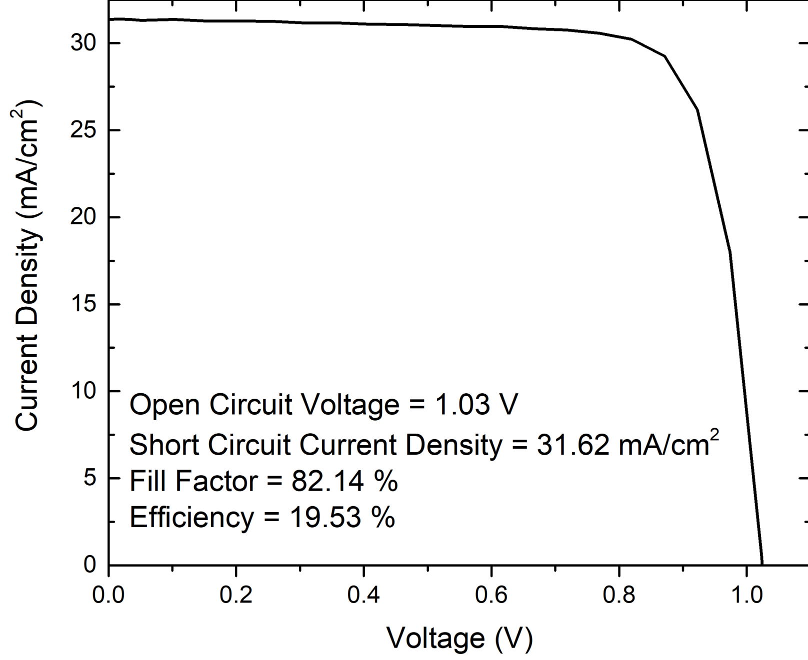

Figure 4.3: AM0 illuminated current density-voltage measurement of the GaAs PV device.

fractional power loss (FPL) from a LCL is given by [65]:

$$FPL = \frac{P_{loss}}{P_{MP}} = \frac{\rho_s S^2 J_{MP}}{12 V_{MP}} \tag{4.1}$$

Where S is the longest path a carrier would travel for a given cell design and ρ_s is the resistivity. Resistivity is given by [65]:

$$\rho_s = \frac{1}{q\mu N t} \tag{4.2}$$

Where q is the elemental charge, μ is the majority carrier mobility, N is the material carrier concentration, and t is the layer thickness. For a 0.75 cm x 1.00 cm cell, with V_{MP} and J_{MP} based on the JV curve in Figure 4.3, the fractional power loss versus is shown in Figure 4.4. After 4 μm, the rate of decrease in the reduction of FPL begins to

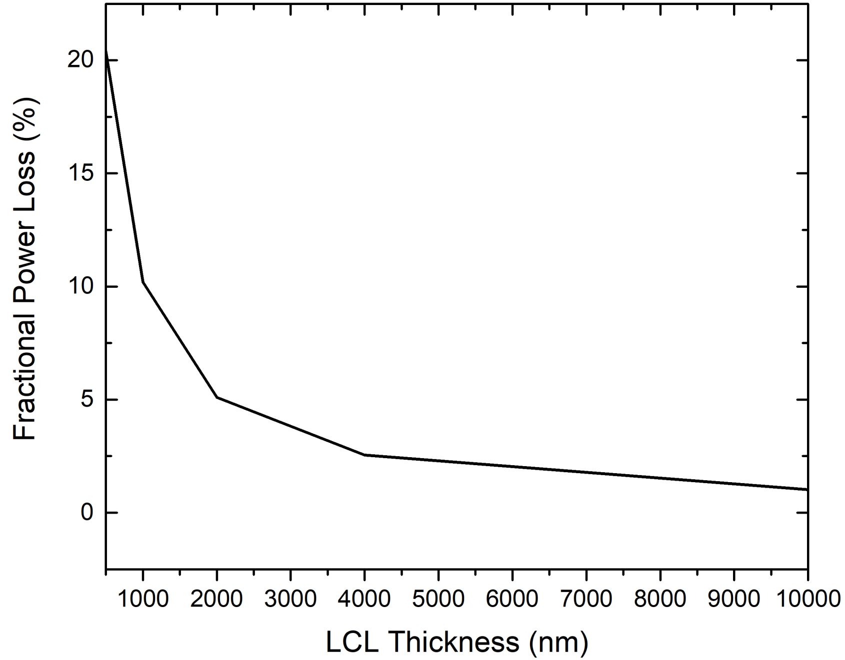

Figure 4.4: Fractional power loss versus AlGaAs LCL thickness for a 1 cm^2 GaAs PV device.

minimize asymptotically at approximately 2.5 %. As a result, a 4 μm AlGaAs LCL was used in the GaAs PV design, and corroborates the difference in efficiency between the top-back GaAs PV device with an efficiency of 22 % and the top-top PV device.

4.1.2.2 EAM Testing

Dark current density-voltage measurements were taken of the discrete EAMs to assess leakage current in reverse bias that would increase the power required to operate the EAM. Experimental J-V measurements were fit with Equation 2.6 to extract reverse saturation current, ideality, and series and shunt resistance, shown in Figure 4.5. With an ideality factor (n) of close to 2, this suggests that recombination is occurring primarily within the depletion region of the device, and is strongly tied to the MQW region material quality. The reverse saturation current is found to be 2.00 x 10^{-6} A/cm^2. For a point of

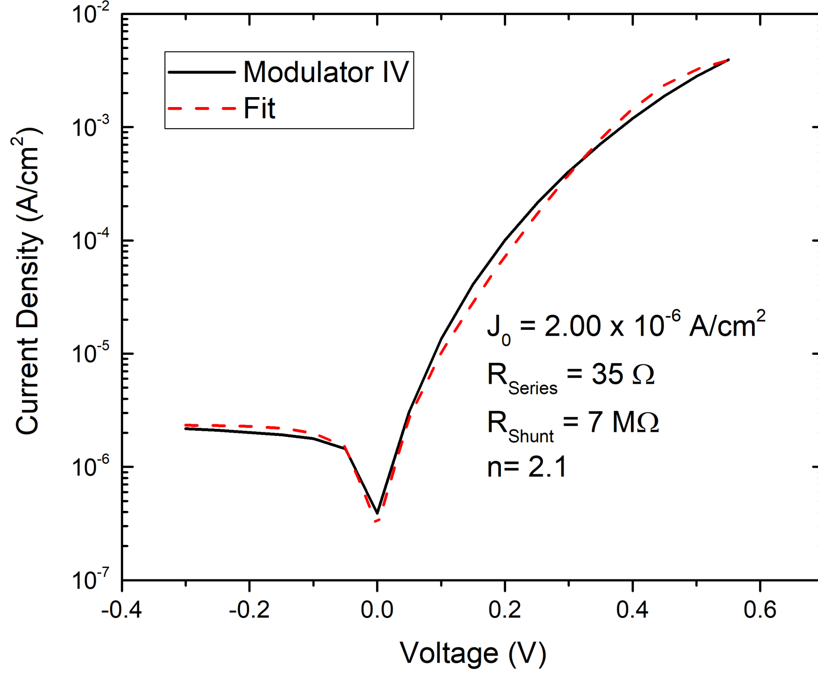

Figure 4.5: Dark current density-voltage measurement and single-diode model fit of a fabricated EAM.

comparison, the recombination current in the depletion region for 1 μm of InGaAs, based on ideal lifetimes and mobilities, is 10^{-9} A/cm^2. The three order of magnitude increase in reverse saturation current is likely due to excess strain in the MQW region above 100 ppm (grown prior to determining under 100 ppm was the target metric). Additionally, the series resistance is high, determined to be 35 Ω. This parameter directly impacts the operating speed of the device due to the adverse effect on the RC time constant.

ON/OFF contrast ratio (CR), also referred to as *extinction ratio* (ER), measurements were conducted on the EAMs. Peak ON/OFF ratio modulation occurred at 1536 nm, attaining a peak value of 1.05 at a bias of -5 V. Slight alterations to QW thickness and/or composition can re-center the modulation peak to 1550 nm. This EAM, however, still demonstrates a ON/OFF ratio of greater than 1 at 1550 nm, which allows it to be used for amplitude modulation and communication at 1550 nm.

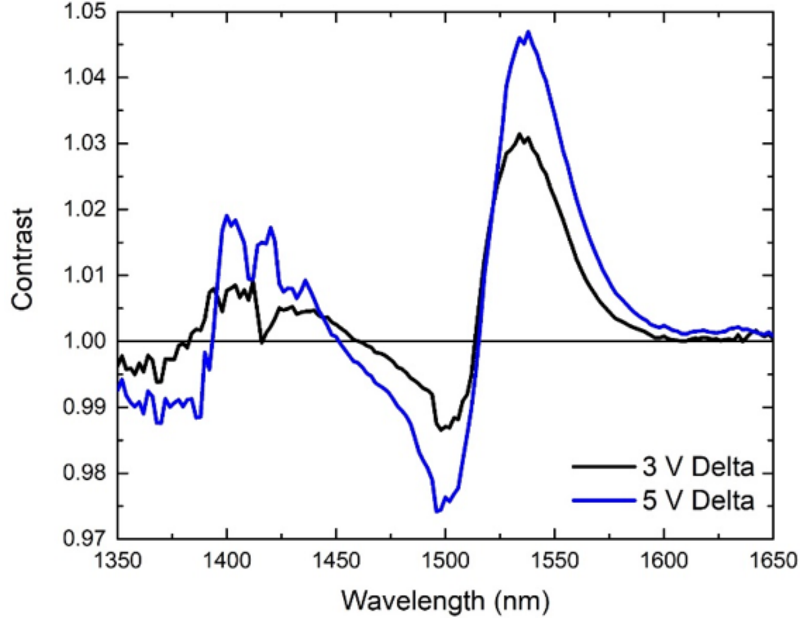

Figure 4.6: ON/OFF contrast measured at 3 V and 5 V reverse bias.

4.1.3 Hybrid Device Bonding and Testing

4.1.3.1 Device Bonding

After fabrication and discrete device testing the modulator and solar cell were diced to allow for bonding of individual devices. Bonding material was selected to be Shipley S1813, a novolak based resist that is optically transparent at 1.55 μm. To form the hybrid device, S1813 is applied directly to the modulator and the PV device is placed on top. The hybrid device was then baked at 90 °C for 10 minutes to remove the solvent from the S1813. The final, mechanically stacked hybrid device is shown in Figure 4.7.

4.1.3.2 Current-Voltage Measurements

Devices were tested for their current density-voltage characteristics pre-bond and post bond. As all four terminals are accessible, the devices can be tested independently of one

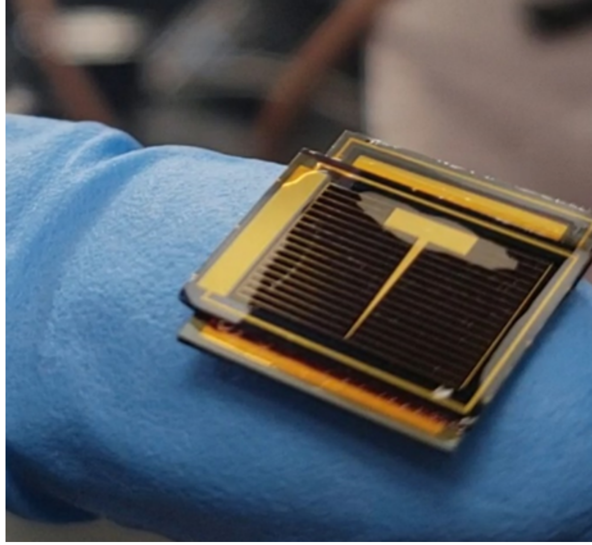

Figure 4.7: Photograph of a completed, mechanically stacked hybrid EAM/PV device with a 1 cm x 1 cm EAM and a 1 cm x 0.75 cm PV cell.

another while bonded together. Figure 4.8 shows that the JV characteristics are identical pre-bond and post-bond, suggesting no adverse effect to electronic device performance from the bonding procedure. If the bonding method had ill-effect on the devices, an increase in dark current and/or an increase in series resistance would be observed.

4.1.4 Simultaneous Modulation and Power Generation

The bonded, hybrid PV/EAM device was tested for simultaneous modulation at 1.55 μm and power generation from 1-sun illumination. Monochromatic light at 1.55 μm was incident on the hybrid device for modulation with additional 1-sun illumination powering the device. A square wave with 5 V amplitude was applied to the modulator terminals of the hybrid device with a frequency of 1 kHz for on-off-keying (OOK). Figure 4.9(top) shows the input signal (CH1) and the modulated output (CH2). Data modulation was possible due to the existence of a contrast ratio at 1.55 μm. This demonstrates the first

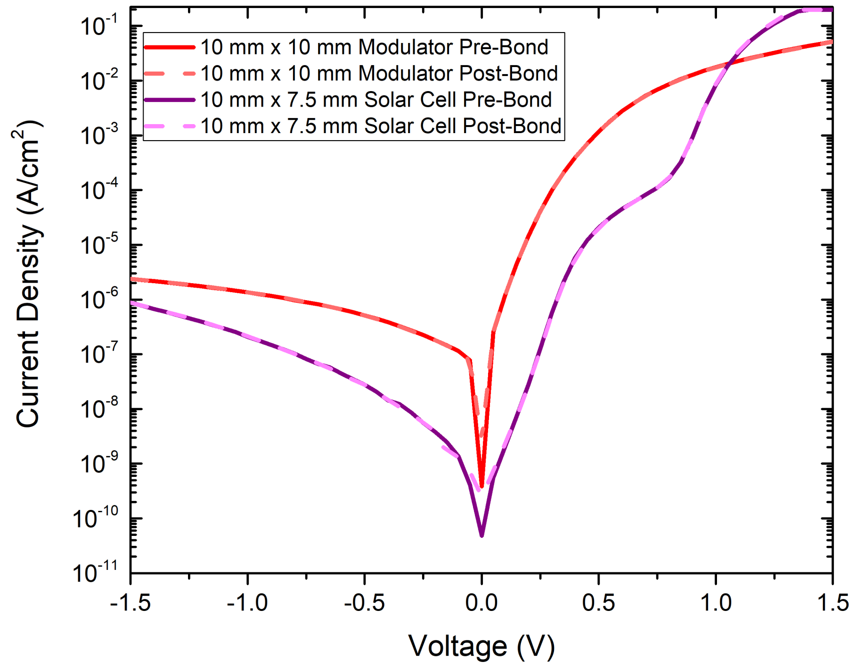

Figure 4.8: J-V characteristics of a modulator and PV device pre-bond and post-bond showing identical performance.

operational prototype design of a hybrid PV/EAM device.

4.2 0.5 U Module Integration

Building upon the single cell prototype discussed previously, a larger, mini-module mechanically stacked hybrid device was designed, grown, and fabricated. The goal was to develop a mini-module for 0.5 U CubeSat form factor integration. This required a redesign of the mask to be able to integrate this device with a printed circuit board and driver electronics. Additionally, to increase power generation in the PV component of the hybrid device a dual junction (2J), $In_{0.51}Ga_{0.49}P$ (InGaP)/GaAs solar cell was used. This design integrated multiple PV cells with a segmented EAM design that would allow for large area PV coverage while still allowing for Mbps-level data modulation. Additionally,

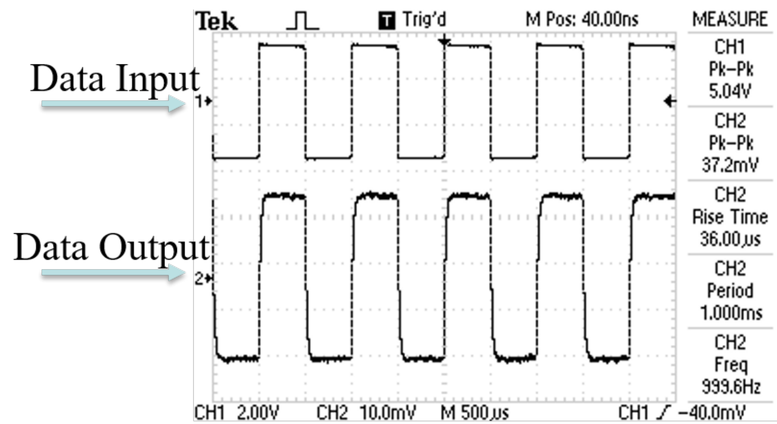

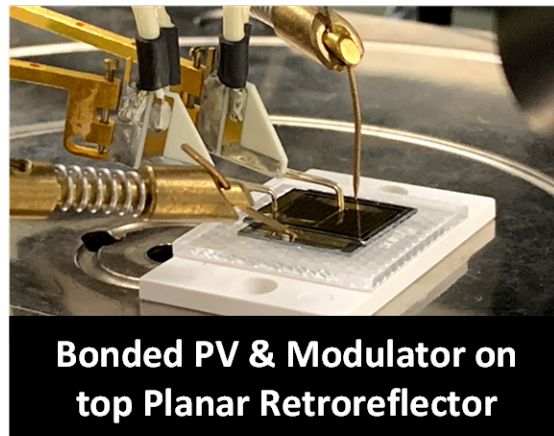

Figure 4.9: Top: Oscilloscope capture of on-off-keying of a hybrid, mechanically bonded PV/EAM device while simultaneously harvesting solar energy.
Bottom: Photograph of a bonded PV/EAM atop a planar retroreflector for reflection mode testing.

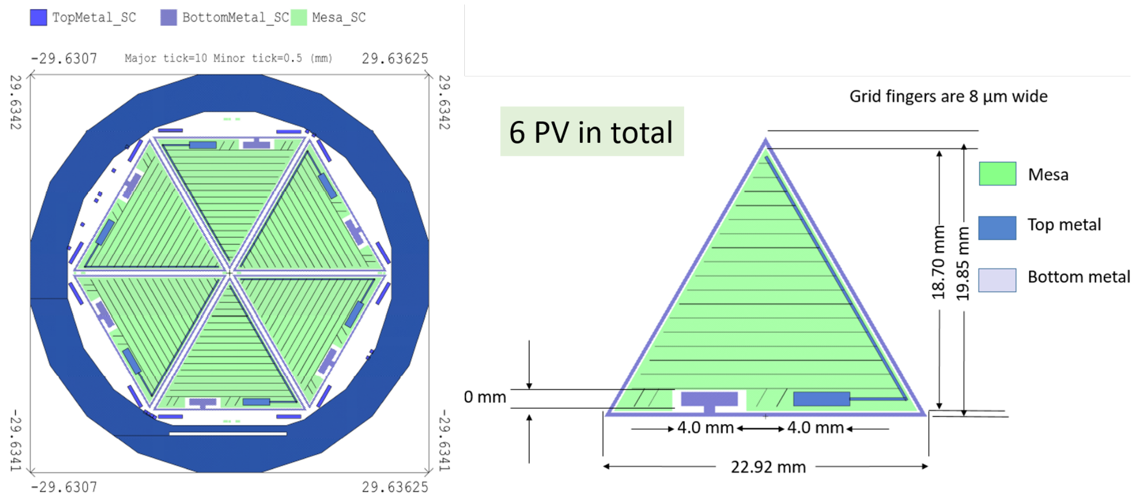

Figure 4.10: Left: Full wafer mask design for 6, 2J PV devices for integration in a PCB. Right: Schematic of PV devices.

a space grade bonding agent, Dow Corning 93-500 (DC 93-500) was investigated for its ability to be used as the bonding agent between PV and EAM components, in addition to being the bonding agent for hybrid device to the PCB.

4.2.1 Mask Design

The goal of the mask for the 0.5 U form factor mechanically stacked device was to be able to integrate a full 2" wafer for each the PV and the EAM into the designed PCB. To maximize the PV area, each cell was made into a 1.93 cm^2 triangular area, with large contact pads (4.0 mm^2 for both the top and bottom contacts) for wire bonding were designed. The total metal coverage was 5.3 %. The back contact extends as a ring around the defined mesa area to minimize generated carrier travel distance and resistive losses. This mask design is shown in Figure 4.10. A total of 6 cells were integrated in this mask.

For the EAM mask, a segmented design was constructed. If the EAM were to match

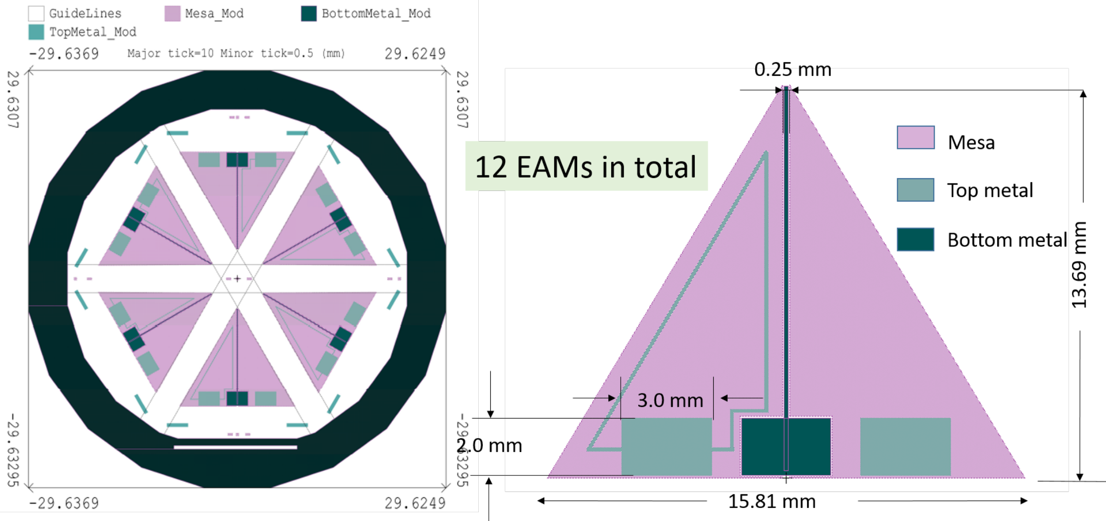

Figure 4.11: Left: Full wafer mask design for 12, segmented EAMs for integration in a PCB.
Right: Schematic of segmented EAMs.

the PV area size (1.94 cm^2), the cutoff frequency would be less than 400 kHz. To achieve a 1 MHz cutoff frequency, device areas of approximately 0.5 cm^2 are required. To achieve this, a segmented design was used, illustrated in Figure 4.11. The 1.94 cm^2 area was divided into two, 0.51 cm^2 mesa defined EAM areas, with a common contact for the bottom metal contact being shared between the two devices. Both the top and the bottom contact pads were 0.6 cm^2 in area for simplicity in wire bonding to the PCB. A total of 12 EAMs were integrated in this design.

4.2.2 Dual Junction Solar Cell Design

For increased power generation in the PV component of the hybrid device, a dual junction InGaP/GaAs PV device was used. This device was based on work by Polly *et al.*, [66], with Figure 4.12 showing the individual layer structure, with details in Table 4.1. The device uses a homojunction InGaP top cell with a heterojunction InGaP/GaAs bottom

cell. This 2J device was designed to be top cell limited to take advantage of the higher fill factor in the top cell [67]. This modeling was done using the analytical drift-diffusion method known as the Hovel Model [68], which models the current generation in each individual layer as a function of the minority carrier diffusion length (L), wavelength (λ) dependent absorption coefficient (α) and reflectance (R), thickness (t), diffusivity, and interface recombination velocity (S). The equations for holes are:

$$J_p = q\int F_0(\lambda)\left\{\frac{L_pF_1(\lambda)+\frac{S_pL_p}{D_p}F_2(\lambda)-F_3(\lambda)\left(\sinh\frac{D_1}{L_p}+\frac{S_pL_p}{D_p}\cosh\frac{d_1}{L_p}\right)}{\left(\cosh\frac{d_1}{L_p}+\frac{S_pL_p}{D_p}\sinh\frac{d_1}{L_p}\right)}-L_pF_4(\lambda)\right\}d\lambda$$

$$+\mathrm{qD}\frac{{}_pp_0\left(e^{qV/kT}-1\right)}{L_p\left\{\frac{\sinh\frac{d_1}{L_p}+\frac{S_pL_p}{D_p}\cosh\frac{d_1}{L_p}}{\cosh\frac{d_1}{L_p}+\frac{S_pL_p}{D_p}\sinh\frac{d_1}{L_p}}\right\}(4.3)}$$

$$F_0(\lambda) = \frac{L_p(1-R_1)\alpha\varphi_0}{\left(1-\alpha^2L_p^2\right)}(4.4)$$

$$F_1(\lambda) = \alpha \tag{4.5}$$

$$F_2(\lambda) = 1 \tag{4.6}$$

$$F_3(\lambda) = e^{-\alpha d_1} \tag{4.7}$$

$$F_4(\lambda) = \alpha e^{-\alpha d_1} \tag{4.8}$$

Table 4.1: InGaP/GaAs dual junction PV device for integration with an EAM.

Layer	**Material**	**Thickness (nm)**	**Doping cm^{-3}**	**Doping Species**
Contact	GaAs	50	2 x 10^{19}	Te
Contact	GaAs	100	5 x 10^{18}	Si
Top Cell Window	$In_{0.52}Al_{0.48}P$	20	8 x 10^{17}	Si
Top Cell Emitter	InGaP	70	2 x 10^{18}	Si
Top Cell Intrinsic	InGaP	10	UID	N/A
Top Cell Base	InGaP	460	5 x 10^{16}	Zn
Top Cell Back Surface Field	$Al_{0.27}Ga_{0.25}In_{0.48}P$	100	2 x 10^{18}	Zn
Tunnel Junction	$Al_{0.30}Ga_{0.70}As$/GaAs	10/10	2 x 10^{19}	C/Te
Bottom Cell Window	$In_{0.52}Al_{0.48}P$	25	8 x 10^{17}	Te
Bottom Cell Emitter	InGP	50	2 x 10^{18}	Si
Bottom Cell Intrinsic	GaAs	200	UID	N/A
Bottom Cell Base	GaAs	3500	2 x 10^{17}	C
Bottom Cell Back Surface Field	InGaP	50	2 x 10^{18}	Zn
Lateral Conduction Layer	GaAs	1000	2 x 10^{19}	C

and by symmetry, the electron current contribution can be found as well. From this, the external quantum efficiency can be modeled. Using measured refractive index values, specifically the extinction coefficient (k), the absorption coefficient as a function of wavelength can be calculated by:

$$\alpha = \frac{4\pi k}{\lambda} \tag{4.9}$$

Using the minority carrier diffusion lengths and interface recombination reported by Polly *et al.*, [66] and measured refractive index values, the thickness of base of the InGaP top cell was adjusted to make the 2J slightly top cell limited. A base thickness of 460 nm resulted in a cell top cell current collection of 16.264 mA/cm^2, and a bottom cell current collection of 16.436 mA/cm^2. With an assumed open circuit voltage of 2.37 V and a fill factor of 88 %, an AM0 efficiency of 24.78 % was predicted from this design. This design, however, is limited by the need for a lateral conduction layer, which will reduce the overall efficiency of the device.

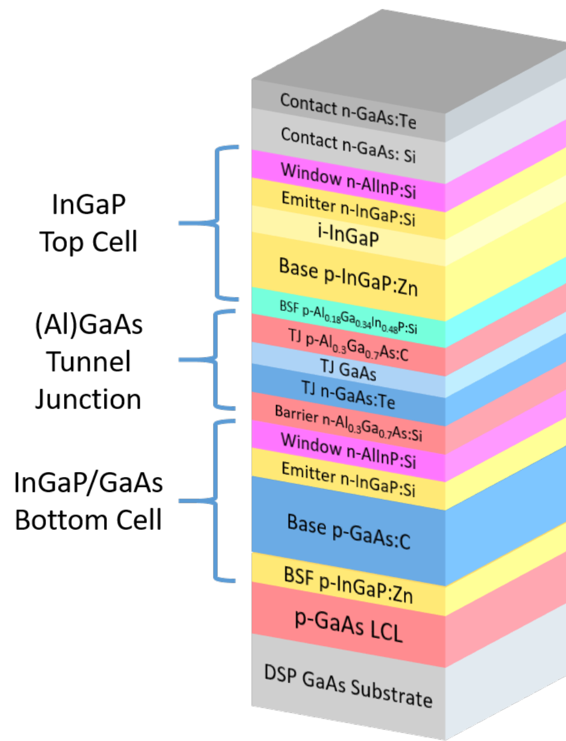

Figure 4.12: Epitaxial layer structure of the 2J PV device, based on results by Polly *et al.*, [66]

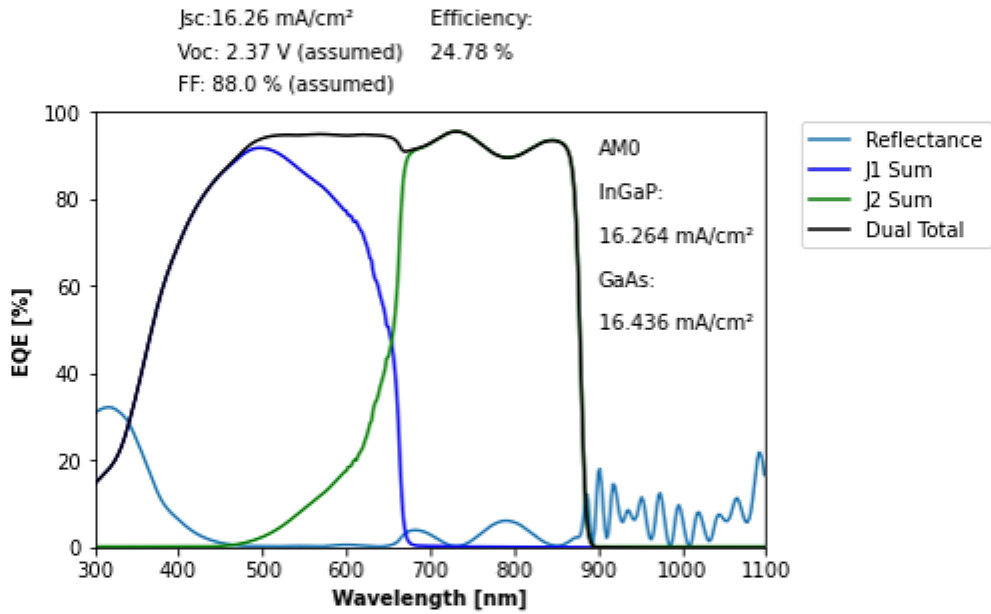

Figure 4.13: Hovel modeling of the 2J PV device, based on results by Polly *et al.*, [68, 66]

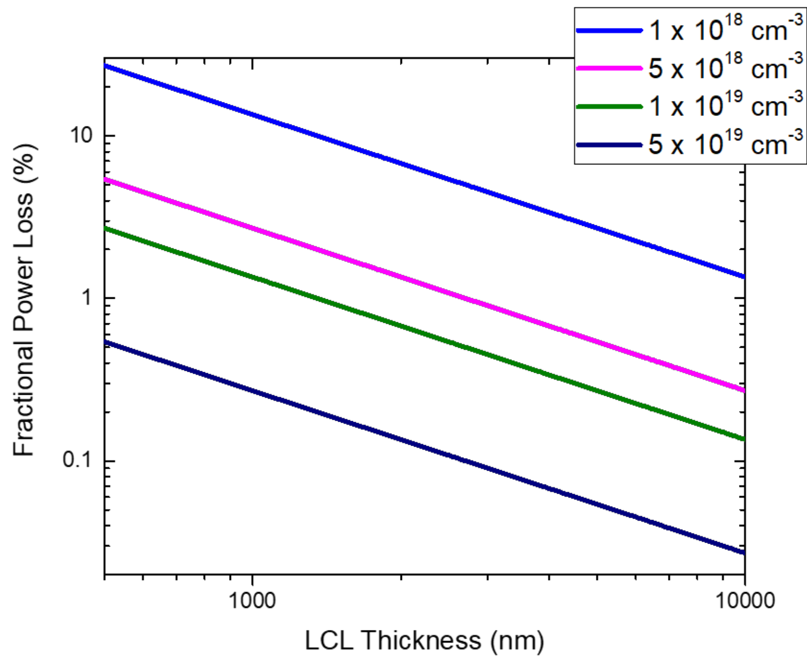

Figure 4.14: Fractional power loss in a 1.94 cm^2 2J PV cell for a GaAs LCL of varied thickness and doping.

4.2.2.1 GaAs LCL Design

A top-top contacting design is required for the 2J PV device in order to be coupled with an EAM and a retroreflector. As a result, a lateral conduction layer is required for the p-type back contact of the device, similar to the device discussed in the single cell prototype. GaAs was selected as the LCL material. The fractional power loss in the LCL based on Equation 4.1 was designed based on the upright JV results reported by Polly *et al.,* for an AM0 cell with no quantum wells. The fractional power loss for varied LCL thicknesses and doping concentrations is shown in Figure 4.15. As thickness and doping levels increase, the fractional power loss in the 2J decreases. This indicates that a thicker, more highly doped LCL is preferable.

A thicker, more highly doped LCL, however, has the drawback of increased free

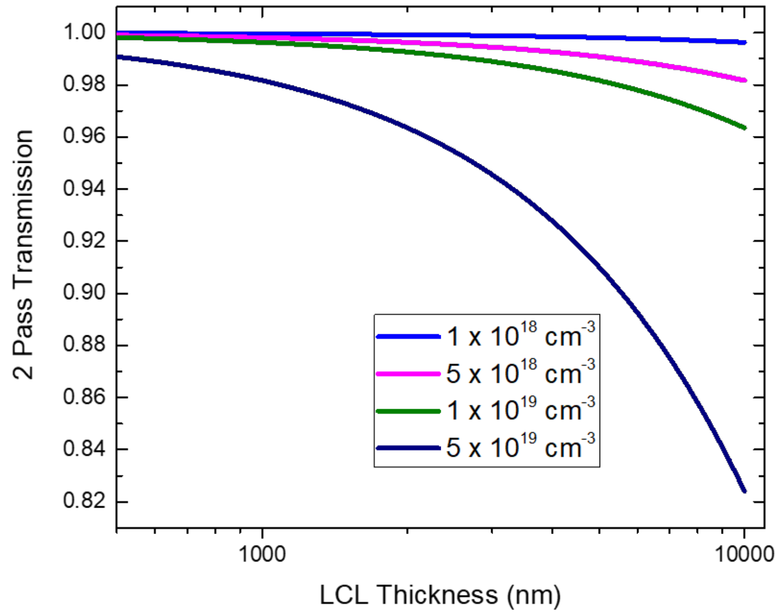

Figure 4.15: Transmission loss at 1550 nm for a GaAs LCL of varied thickness and doping.

carrier absorption. Using Equations 3.1 [56] and 3.2, the transmission loss as a function of LCL thickness and doping was modeled, with the results shown in Figure 4.15. As thickness and doping increases, transmission decreases. To balance both the need for low transmission loss and low fractional power loss, a GaAs LCL thickness of 1000 nm doped 1 x 10^{19} cm^{-3} was selected. This would result in an anticipated overall efficiency loss of 1.5 % and transmission loss of 1.0 % based on the model estimates.

4.2.2.2 2J PV Growth and Fabrication

The 2J PV devices were grown on an Aixtron 3x2" Close-Coupled Showerhead System using the precursors described in Section 3.2.1. Growth temperatures were between 580 and 680 °C. The devices were grown on (100) 2° → <111A> DSP (to limit scattering)

UID (to limit free carrier absorption in the substrate) wafers were used.

The fabrication of the 2J was nearly identical to the fabrication of the 1J GaAs cell described previously. Metal contact was made to the solar cell using standard electroplating procedures. Cell areas were defined via mesa isolation in a chemistry of H_2O_2:H_3PO_4:H_2O (3:4:1) for the As-based materials and 1:1 HCl:H_3PO_4 for the P-based materials. The n+ GaAs contact was removed in a solution of NH_4OH:H_2O_2:H_2O (1:1:50). An anti-reflection coating (ARC), described in upcoming sections, of ZnS/MgF_2 was thermally evaporated to enhance PV absorption.

4.2.2.3 2J PV Results

After fabrication, but prior to ARC deposition, the 2J cells were tested for their external quantum efficiency (EQE). In order to deposit an ARC that gives the optimal boost to current collection, the non-ARC EQE was fit using the Hovel model (Figure 4.16) to obtain the diffusion lengths in each of the layers of the 2J cell and then thickness of ZnS and MgF_2 was iterated to find the optimal thickness for the highest efficiency. Figure 4.17 shows the parameter space for the efficiency of the 2J as a function of ARC thickness. For an efficiency of 24 % based on only the EQE, a thickness of 55 nm for ZnS and 100 nm for MgF_2 were deposited.

After ARC deposition, the 2J PV devices were tested for their AM0 illuminated current density-voltage characteristics, with the resulting JV curve shown in Figure 4.18, and the figures of merit for the expected 2J results based on a top-bottom contact versus the measured top-top design in Table 4.2. The expected and measured open circuit voltages are identical, and the measured short circuit current density is within 0.1 mA/cm^2 of

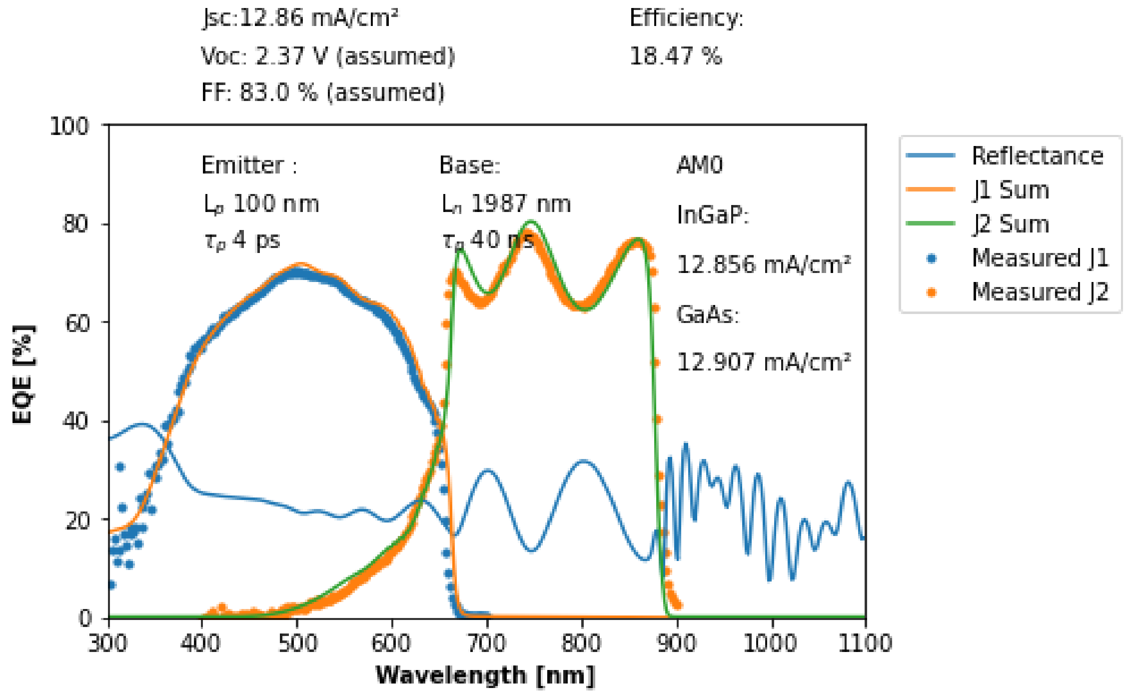

Figure 4.16: Hovel modeling fit of the fabricated 2J PV device before ARC [68].

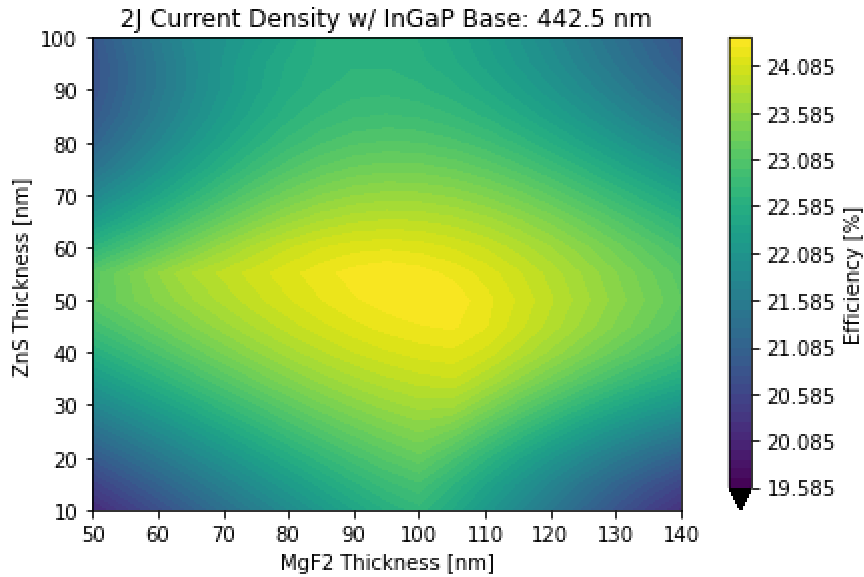

Figure 4.17: ARC thickness optimization based on non-ARC EQE results shown in Figure 4.16.

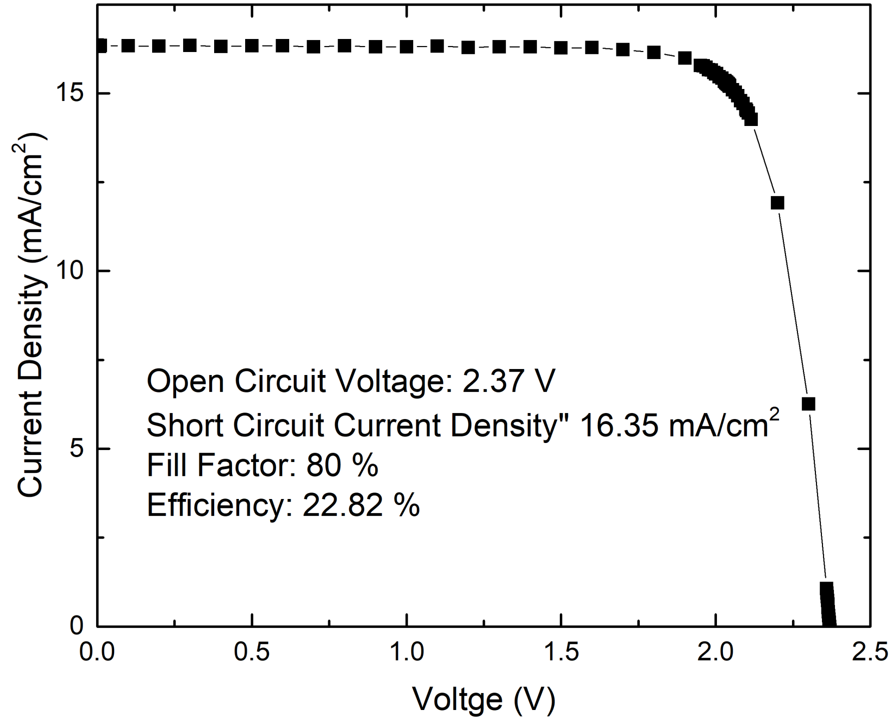

Figure 4.18: AM0 illuminated J-V curve for the 2J device after ARC deposition.

the expected modeled value, indicating high accuracy in the modeling. The difference in fill factor is due to the resistive loss in the lateral conduction layer, which is not modeled in the top-bottom design. This reduction in fill factor resulted in an absolute decrease of 1.96 %, which is close to the anticipated loss of 1.54 %.

Transmission loss as a function of wavelength was also measured through the 2J PV device, shown in Figure 4.19. The measured transmission loss through the 2J PV is approximately 4 %. The expected contribution of the GaAs LCL to this transmission loss is 1.5 %, the remaining 2.5 % transmission loss is likely from free carrier absorption in the absorber layers of the 2J PV device, and some non-zero loss in the 350 μm thick UID substrate.

Table 4.2: 2J JV figures of merit for the modeled top-bottom device and the measured top-top device.

Device	$\mathbf{V_{OC}}$ **(V)**	$\mathbf{J_{SC}}$**(mA/cm²)**	**Fill Factor (%)**	**Efficiency (%)**
Modeled Top-Bottom	2.37	16.25	88	24.78
Measured Top-Top	2.37	16.35	80	22.82

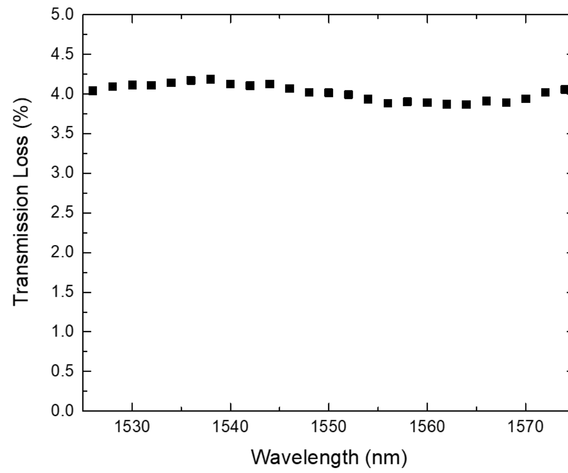

Figure 4.19: Measured transmission loss in the 2J PV device.

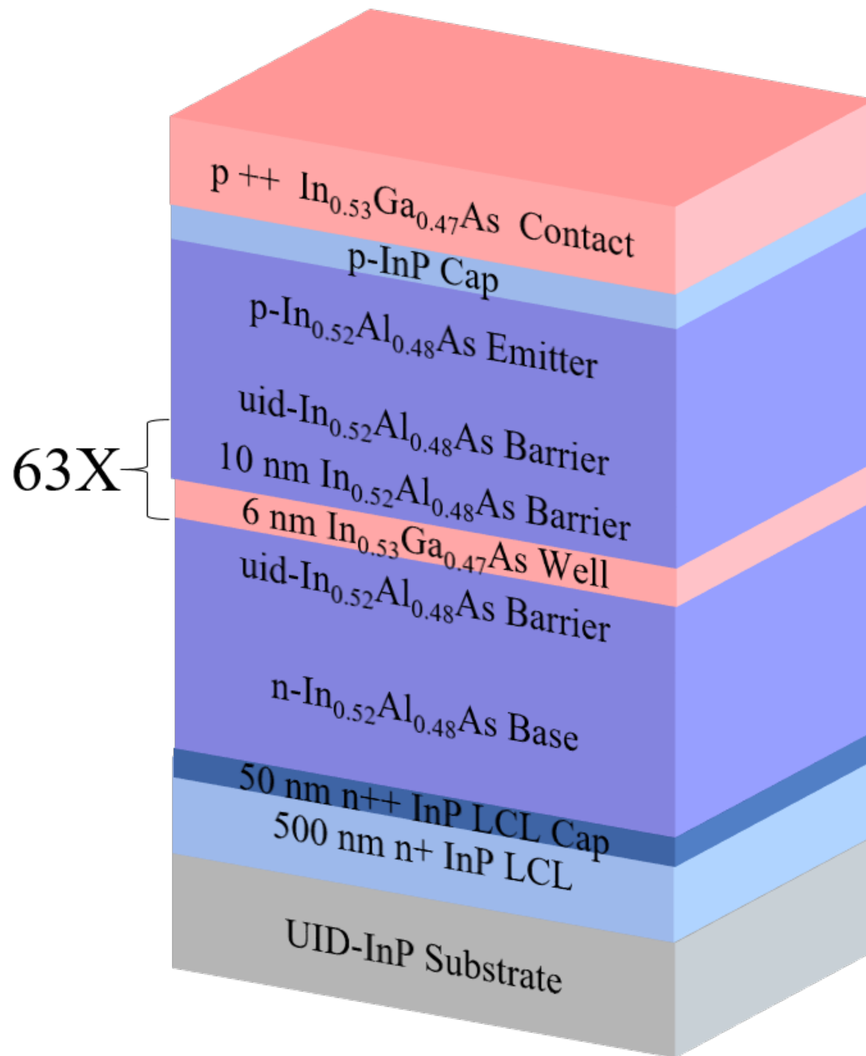

Figure 4.20: Epitaxial layer structure of the EAM for integration with the 2J PV device for the 0.5 U form factor.

4.2.3 EAM Design

An EAM for fabrication using the mask set described previously was designed, illustrated in Figure 4.20. This design was done in tandem with the development conducted in Chapter 3, and as a result the quantum wells of the EAM were only 6 nm thick, resulting in a peak ON/OFF ratio that would be closer to 1450 nm. This EAM was grown and fabricated using identical conditions as were described in Chapter 3.

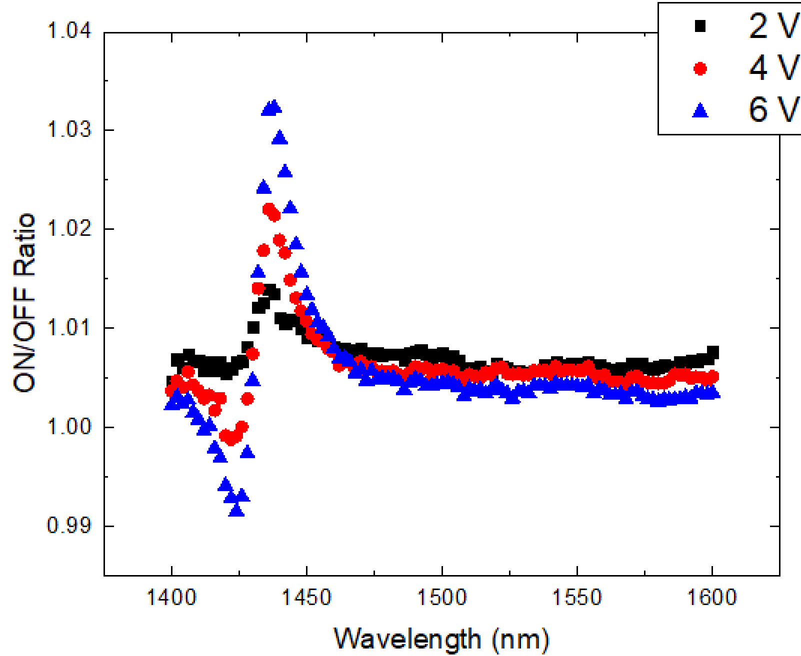

Figure 4.21: ON/OFF ratio measurements of the EAM for mechanical bonding.

4.2.3.1 EAM Results

Discrete device testing of the EAM was conducted. ON/OFF ratio measurements (Figure 4.21) reveal that the well was grown too thin for operation at 1550 nm. At a bias of -6 V, the peak ON/OFF ratio location is 1448 nm, not only blue-shifted from 1550 nm, but also completely out of the C-band. This, however, can easily be rectified by increasing the well thickness to closer to 10 nm. Using a 1450 nm laser, the cutoff frequency of the EAM was measured, shown in Figure 4.22. The half power point occurs at 1 MHz, which based on the segmented design of the EAM mask is on target. By the Shannon-Nyquist theorem, this correlates to an attainable data rate for this design of 0.5 Mbps. Although this device was severely blue-shifted due to an error in the design, this EAM was still used to mechanically bond to a 2J PV device for proof-of-concept and prototyping of the 0.5 U form factor PCB and retroreflector.

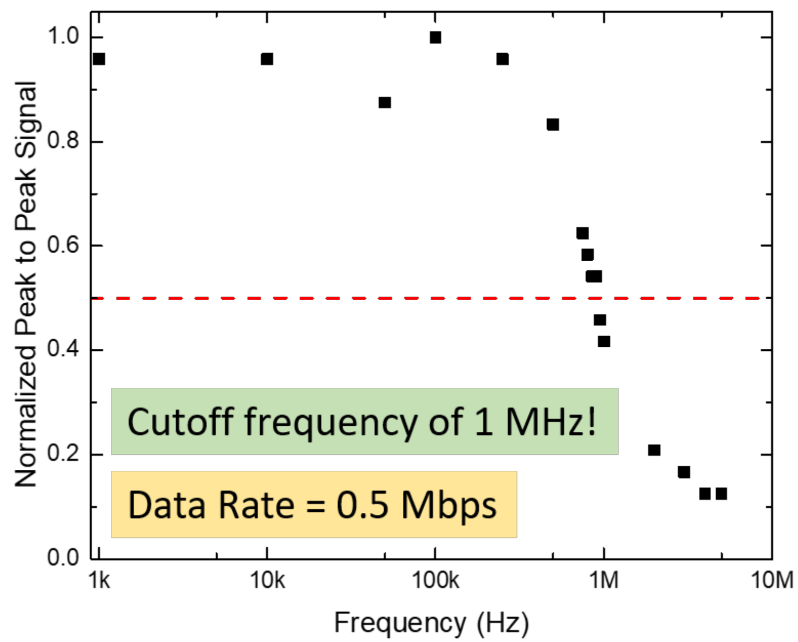

Figure 4.22: Cutoff frequency of the EAM for mechanical bonding.

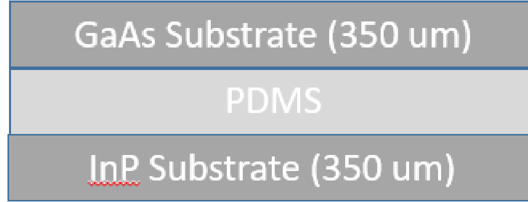

Figure 4.23: PDMS structure for modeling of transmittance in TFCalc

4.2.4 Device Bonding and Packaging

To mechanically integrate the PV device with the EAM, a bonding agent is required. This bonding agent needs to be optically transparent to 1.55 μm light. Additionally, it is desirable to use an already space-qualified epoxy for the bonding to make the 0.5 U package as flight ready as possible for the prototype design. Dow Corning 93-500 (DC 95-500), a polydimethylsiloxane (PDMS) based elastomer with low thermal vacuum outgassing, meets both of these requirements. Due to the refractive index change from a III-V wafer (n = 3.2 at 1.55 μm) to the polymer bonding layer (n = 1.4 at 1.55 μm) a reflective interface is created that reduces transmission of the data communication wavelength through the entire stack. To investigate the effects of a bonding layer on transmittance, the transmittance was modeled in Software Spectra, Inc.'s TFCalc^{TM}, a transmission matrix optical modeling and optimization software for the mechanically bonded device. Figure 4.26 shows the effect of thickness of the bonding layer on transmittance across the C-band (1525-1572 nm). As the bonding layer thickness increases, the oscillations in transmittance get closer and closer, resulting in relaxed engineering controls for interface thickness. As a result, having the thinnest, most uniform DC 93-500 is critical to ensuring high transmittance and minimizing insertion loss.

One option to minimize the effect of the bond layer's low index of refraction is to

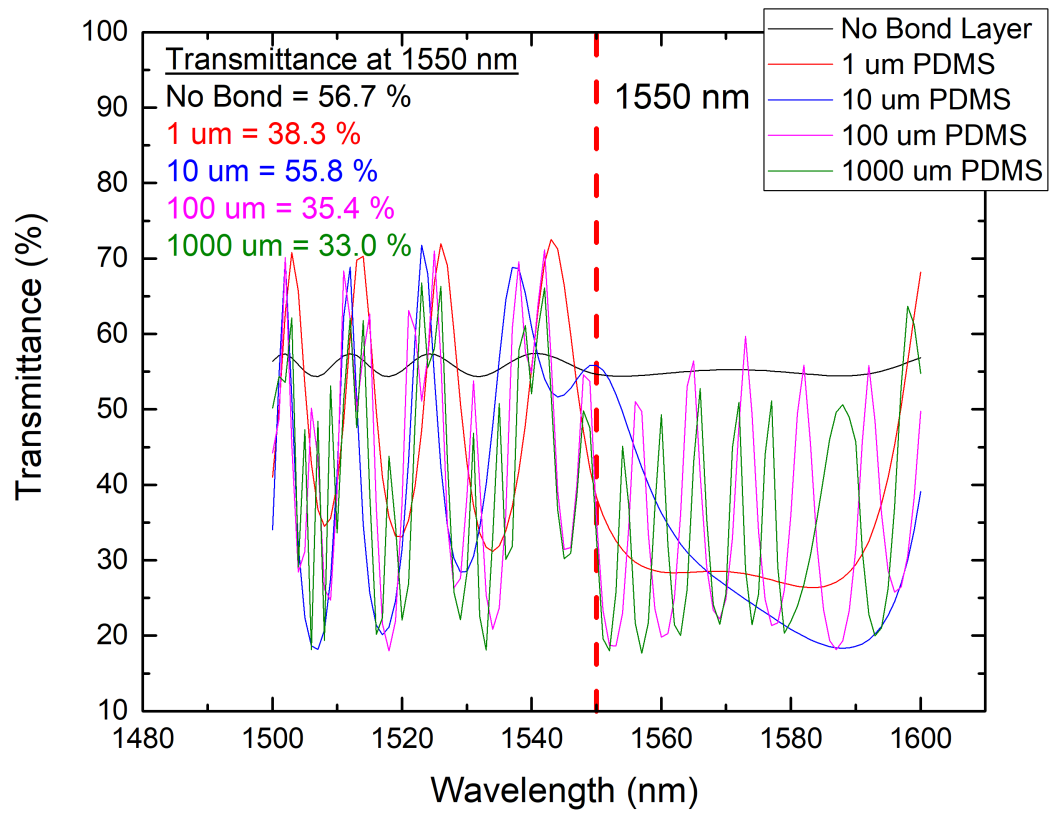

Figure 4.24: TFCalc modeling of C-Band transmittance through a GaAs substrate bonded to an InP substrate with PDMS.

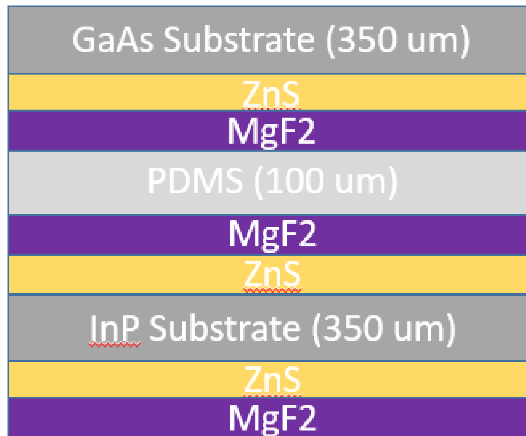

Figure 4.25: ZnS/MgF_2 structure for modeling of transmittance in TFCalc

grade the index in and out of the low index bond material. This can be realized by coating the interfacing side of both of the GaAs PV wafer and InP EAM wafer with ZnS (n = 2.3) and MgF2 (n = 1.4). Optimizations were performed at both specifically 1550 nm and the entire C-band. The bond layer thickness was set to 100 µm, and the structure is shown in Figure 4.25. When optimized for the entire C-band, the difference between the peak and the valley of transmittance is reduced, however the maximum values for transmittance are higher if optimized directly for 1550 nm. There is a trade off between engineering control if there is a slight change in bond layer thickness or drift in the thermal evaporation of the ZnS or MgF_2. As a result, no ZnS or MgF_2 backside coatings were applied. A thickness of 50 μm was selected for the PDMS layer as this was the thinnest, most consistent coating that was attained via Doctor Blading.

A thickness of 50 μm was selected for the PDMS layer as this was the thinnest, most consistent coating that was attained via Doctor blade coating. The bonded PV/EAM was then cured at 100 °C for one hour on a hot plate. The bonded wafers were then adhered to a printed circuit board designed for connecting with a retroreflector and driver

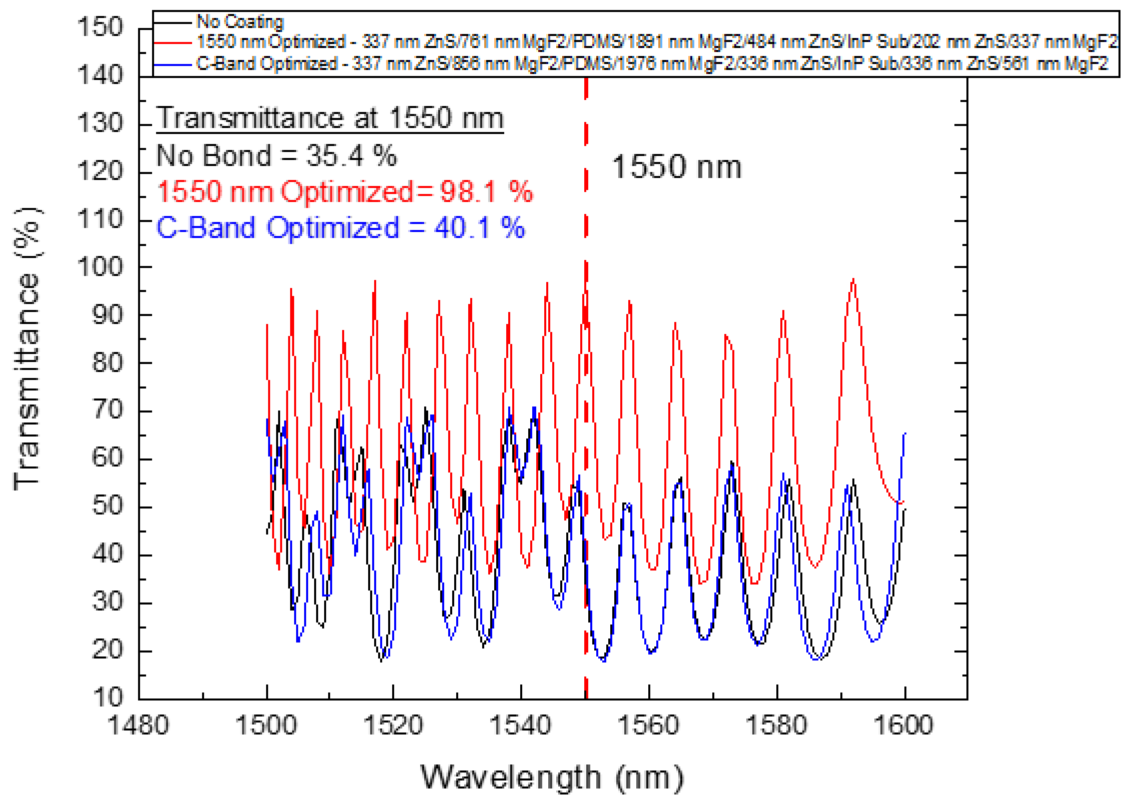

Figure 4.26: C-Band and 1550 nm optimized transmittance with various ZnS and MgF_2 coatings.

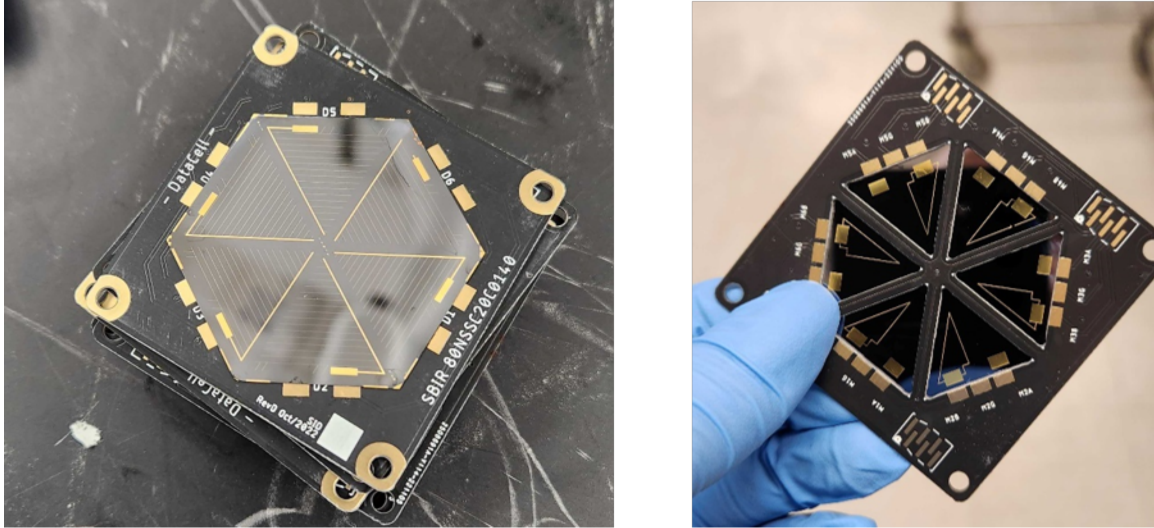

Figure 4.27: A picture of a test wafer for bonding to the PCB with the top metal design of the PV (left) and EAM (right) electroplated for placing and testing.

electronics in a 0.5 U form factor using the DC 93-500 as the glue for this bond. A test wafer bonded to the PCB is shown in Figure 4.27.

After bonding to the PCB, the contacts for the EAM and PV devices were wire bonded to the pads on the printed circuit board using an F&S 56i Wire Bonder. Since the PCB is dual sided, both sides need to be wire bonded. This raises an issue, however, as hard vacuum contact is required to a surface of the PCB in order to bond, and one side of the PCB has the PV device as the 'flat' face. If the PV side was placed faced down on the vacuum chuck, this would damage the PV device. As a result, a 3D printed chuck was constructed in order to wire bond to both sides of the device (Figure 4.28).

4.3 Summary of Section

Two different variations of a mechanically stacked device have been reported on. A single junction GaAs cell bonded to a single EAM as an initial prototype design was

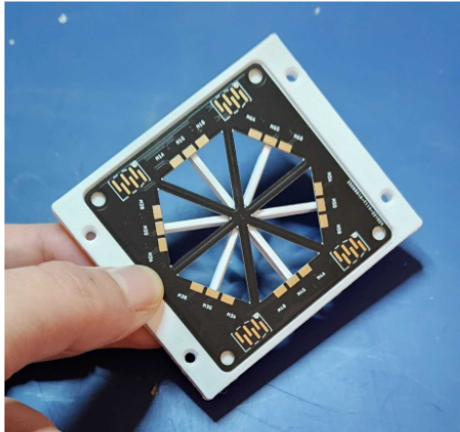

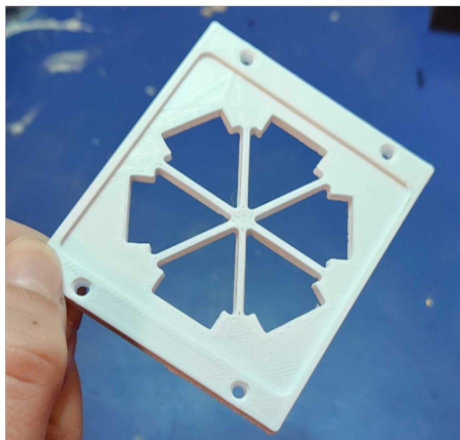

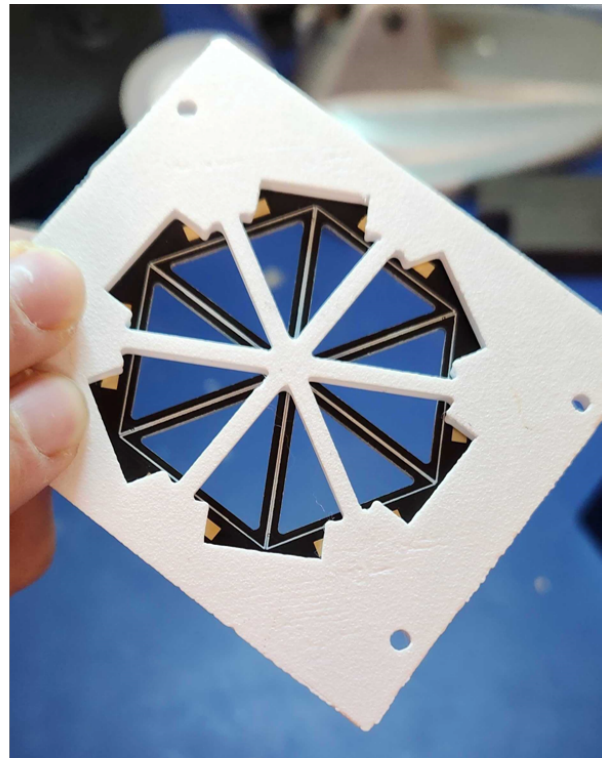

Figure 4.28: Photographs of the 3D printed chuck for wire bonding to both sides of the PCB.

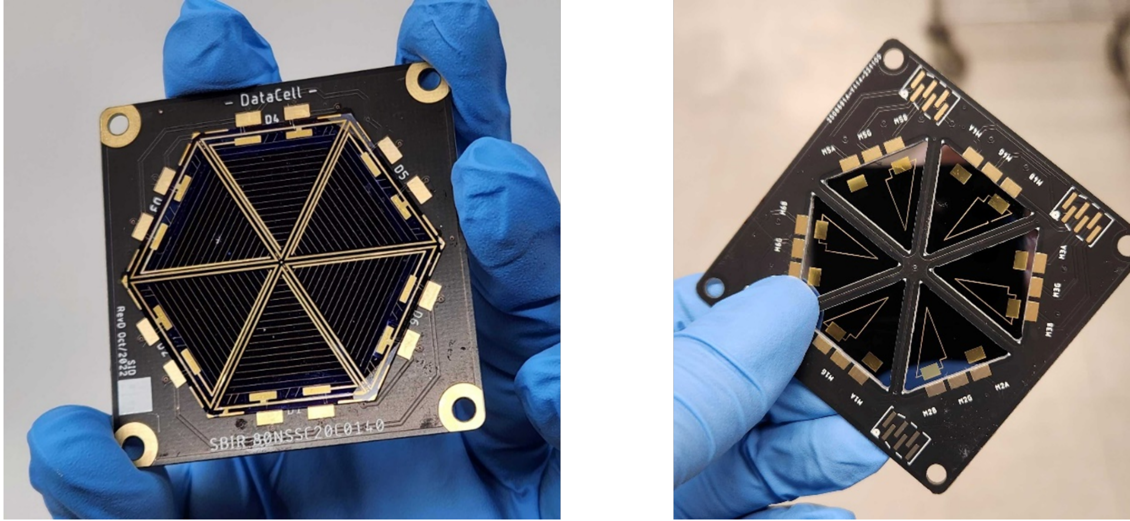

Figure 4.29: Final 0.5 U form factor mechanically stacked PV/EAM device.

constructed, with a power conversion efficiency of 19.53 % under AM0 illumination and an ON/OFF ratio of 1.04 near 1550 nm. As the EAM device was large (1.00 cm^2), the potential data rates for this device are less than 250 Kbps based on results in Chapter 3.

To expand on the capabilities of the mechanically stacked device, a 0.5 U form factor mini-module was developed, with the final product shown in Figure 4.29. A 2J PV device was designed, balancing both the transmission loss and fractional power loss in the LCL. This resulted in an efficiency of 23 %, with the loss in efficiency similar to the model's predicted valued. The EAM, while blue-shifted from the targeted ON/OFF ratio location of 1550 nm, attained a cutoff frequency of 1 MHz by segmenting the modulator design. Not only did this double the data rate of the initial, single cell design, this module encompassed a much larger overall area, resulting in a much larger effective modulation area while having a higher operating frequency. Small modifications to the QW region of the EAM will shift the ON/OFF ratio back to 1550 nm, and a fully functional device can be realized.

Chapter 5

Monolithically Integrated Device

5.1 Monolithic Design Advantages

In Chapter 4 a mechanically stacked, four-terminal hybrid PV/EAM device which utilized discrete components was discussed. An alternative approach is to monolithically integrate the PV component and EAM component by epitaxially growing the EAM and PV components on a single wafer. A monolithically integrated hybrid PV/EAM device has several key advantages over the mechanically stacked design.

The first advantage is the reduced manufacturing complexity. The mechanically stacked design required two separate growths, two separate fabrication procedures, and four different metallization. For a monolithic design, only a singular growth is required, and the fabrication procedure yields both the PV device and the EAM. Additionally, the PV and EAM can share a common contact, reducing the number of metallization steps to three. The epitaxial layer structure and fabrication procedure are discussed in Section 5.5.

Another advantage is the reduction in insertion loss, which in turn boosts EAM

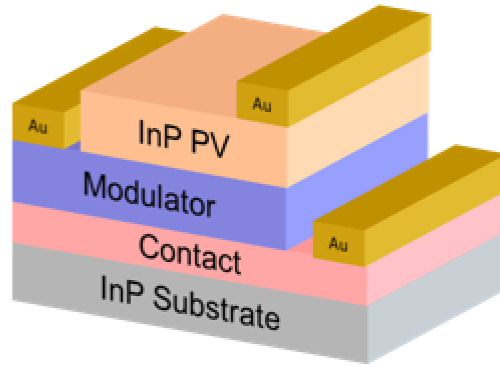

Figure 5.1: High level illustration of a three terminal monolithic device on InP.

performance. The bond material (DC-93500) used to mechanically stack the PV device and EAM is not index matched to either the GaAs substrate of the PV device (n = 3.3779 at 1.55 μm) or the InP substrate (n = 3.1649 at 1.55 μm) for the EAM, having a refractive index of approximately 1.58 at 1.55 μm. This results in reflective losses at the interface of the semiconductor material and bond material, which increases insertion loss. Additionally, only needing one substrate rather than two reduces further the overall SWaP of the hybrid device by 50 %.

Due to the severe lattice mismatch between GaAs and InP, a GaAs-based PV device is insufficient for a monolithically integrated device. As a result, it is more strategic to remain within the InP-based material system, and develop a PV device that is lattice matched to the host material for the EAM. A high level illustration of a proposed three terminal monolithic device on InP is shown in Figure 5.1.

Table 5.1: Literature results for MOVPE grown InP solar cells.

Author	V_{OC} (mv)	J_{SC} (mA/cm^2)	Efficiency (%)	Citation
Spitzer *et al.*,	868	33.88	17.9	[80]
Wanlass *et al.*,	882	33.06	17.6	[81]
Keavney *et al.*,	876	36.34	19.1	[75]
Wanlass *et al.*,	943	37.12	21.1	[76]

5.2 InP Solar Cell Development

InP solar cells have been heavily studied as a potential candidate for space-based photovoltaics due to its superior radiation tolerance compared to GaAs [69, 70, 71, 72, 73, 74]. Under AM0 illumination, a record single junction InP solar cell without a back surface reflector has attained a power conversion efficiency of 19.1 % [75], and 21.1 % with a back surface reflector [76]. Development of InP-based photovoltaics has recently been limited, largely due to the inability to grow a sufficient window layer. Lattice-matched InAlAs and AlAsSb, the most likely candidates for a window material, would in theory provide a significant boost to short-wavelength collection [77]. The interface between InP and most other adequate window materials suffers from a Type II band alignment [78, 79]. As a result the interface recombination velocity is very high at that interface, eliminating any benefit of having a window layer. The best literature reported values for MOVPE grown InP solar cells is shown in Table 5.1.

InP solar cells, prior to this work, have not been demonstrated at RIT. As a result, in-house development of an adequate InP solar cell with a target AM0 efficiency of 17 % for monolithic integration into a hybrid device was required. To simplify this process, development was conducted on single-junction, top-bottom contact InP solar cells. All structures were *np* structures, as *np* InP solar cells have demonstrated superior radiation

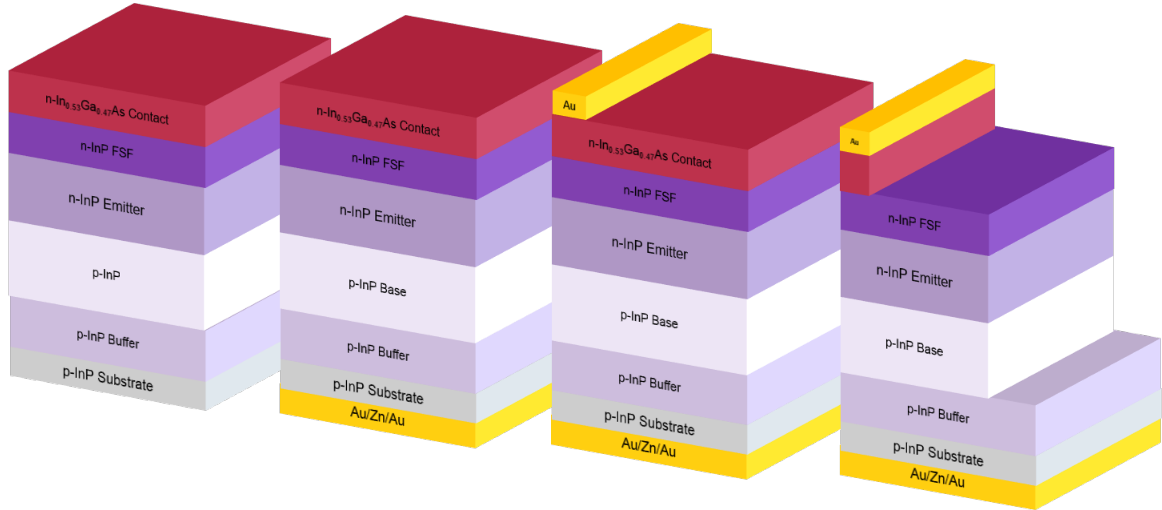

Figure 5.2: Illustration of the fabrication procedure for a single junction, top-bottom contact InP solar cell.

tolerance compared to *pn* InP solar cells at end-of-life (EOL) [70].

All cells described in this section were grown via MOVPE on an Aixtron 3 x 2" Close-Coupled Showerhead system. The indium and phosphorus precursors were trimethylindium and phosphine, respectively. Dopant sources used were disilane and diethyltelluride for n-type materials (layer dependent) and diethylzinc for p-type layers. Unless otherwise specified, the growth rate for InP was 2 μm/hr, and a V/III ratio of 158 was maintained.

5.2.1 Fabrication Procedure

The fabrication procedure developed for InP solar cells is shown in Figure 5.2. Au/Zn/Au is thermally evaporated with thicknesses of 20 nm/20 nm/500 nm to make ohmic contact to the p-type InP substrate. Au is thermally evaporated as the metal contact to the top InGaAs contact layer, defined via a standard liftoff procedure. Individual cells are then mesa isolated in a solution of 1:1:1 HCl:H_3PO_4:CH_3COOH, etching through the InP front surface field (FSF), the emitter, and the base. Finally, a self-aligned contact etch

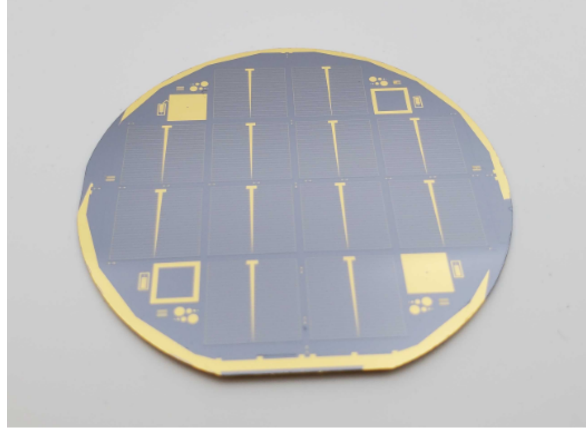

Figure 5.3: Picture of a completed InP solar cell with 12, 1 cm^2 cells on a 2" wafer.

is performed on the the InGaAs contact in a solution of 1:1:10 H_3PO_4:H_2O_2:H_2O. For all InP solar cells described in this section, no anti-reflection coating was applied. A picture of a completed InP solar cell after fabrication is shown in Figure 5.3.

5.2.2 Front Surface Field Thickness Study

Due to the limitation of suitable wide bandgap, heterointerface window materials, a very highly doped, thin InP front surface field (FSF) can be employed, taking advantage of the Moss-Burstein shift [82, 83]. The Moss-Burstein shift effectively blue-shifts the absorption edge of a degenerately doped semiconductor due to population of states close to the conduction band. This increases the observed bandgap of the semiconductors. Parasitic absorption due to the very high doping required to enact this effect, however, still occurs. As a result, it is imperative to find the optimal thickness that provides adequate surface passivation while minimizing parasitic loss.

Using the fabrication procedure outlined in Section 5.2.1, InP solar cells with FSF thicknesses of 5, 10, and 15 nm were grown and fabricated. Details of the layer structure

Table 5.2: InP solar cell layer structure for investigating the effect of the front surface field thickness .

Layer	**Thickness (nm)**	**Doping Level (cm^{-3})**	**Dopant**
Contact	500	1×10^{19}	Si
Front Surface Field	5/10/15	5×10^{19}	Te
Emitter	200	5×10^{16}	Si
Base	5000	1×10^{16}	Zn
Buffer	50	2×10^{18}	Zn

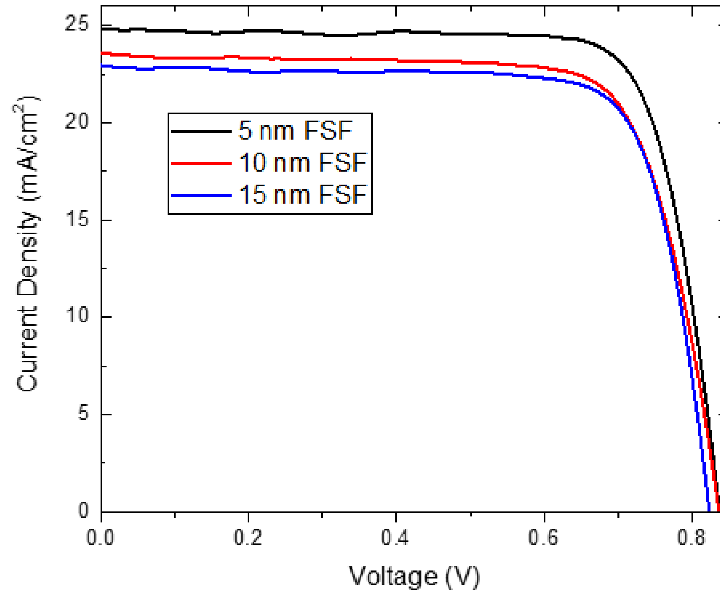

Figure 5.4: AM0 illuminated J-V curves of InP solar cells with varying FSF thickness.

are shown in Table 5.2. To maintain better control of the FSF growth, the growth rate was reduced to 0.35 μm/hr for the FSF growth. Additionally, tellurium (Te) was used as the dopant for the FSF as higher doping levels, into the 10^{19} cm^{-3} range, can be achieved, unlike with silicon (Si).

AM0 illuminated J-V curves for the InP solar cells with varying FSF thicknesses are shown in Figure 5.4. It is evident that as the thickness of the FSF increases, there is increased parasitic absorption, resulting in a sizeable loss in J_{SC}. This is the predominant

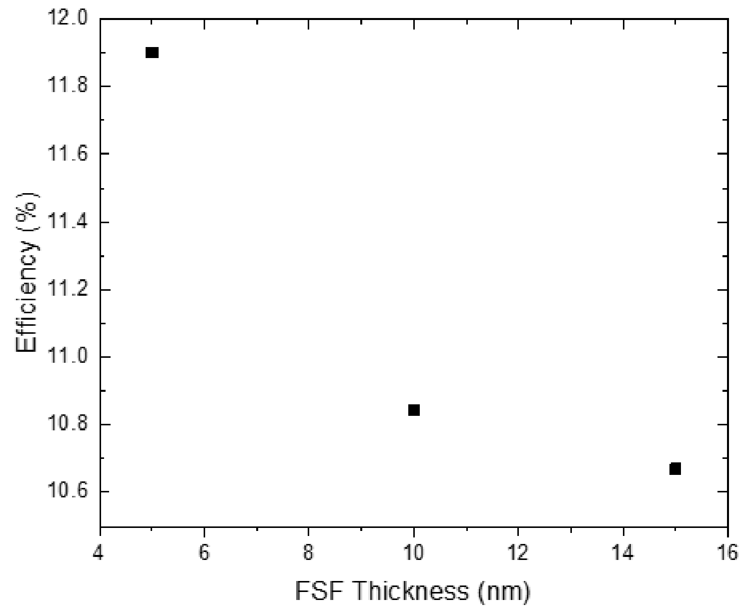

Figure 5.5: Efficiency versus FSF thickness for InP solar cells.

reason for the loss in efficiency as FSF thickness increases; the open circuit voltage for all FSF thicknesses are within 10 mV of each other, and the fill factor for each of the cells are very close, ranging from 75 to 78 %. Efficiency versus FSF thickness is plotted in Figure 5.5, which shows that as FSF thickness increases, efficiency drops. It is evident that a FSF of 5 nm is the best observed FSF thickness for this design.

5.2.3 Emitter Thickness Study

In addition to evaluating the effect of the front surface field, the effect of emitter thickness was also investigated. Using the same epitaxial layer structure as Table 5.2, with the FSF fixed to 10 nm, emitter thicknesses ranging from 50 to 200 nm were investigated. The open circuit voltage, short circuit current density, fill factor, and efficiency as a function of emitter thickness, is shown in Figure 5.6. From these results, it is evident that a 150

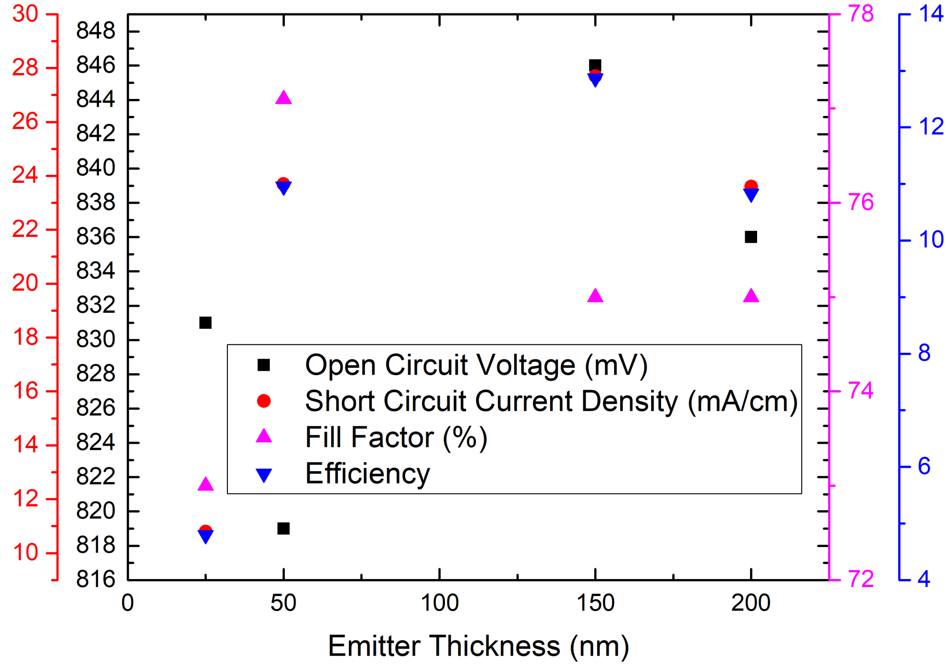

Figure 5.6: Open circuit voltage, short circuit current density, fill factor, and efficiency as a function of emitter thickness

nm has the best open circuit voltage, short circuit current density, and overall efficiency. This device also compared well to the best cell reported by Keavney *et al.*,, with the IQE shown in Figure 5.7.

5.3 Monolithic Device Mask Design

For the monolithically integrated device, a five-layer mask design was used. Devices of two different sizes were designed - one with a 1.00 cm^2 active PV area and a 1.22 cm^2 EAM area, and one with a 0.50 cm^2 PV area and a 0.35 cm^2 EAM area. Based on the best InP PV results from Keavney *et al.*, a 1.00 cm^2 device would result in 26.23 mW of power generated, whereas a 0.125 cm^2 device would generate 3.28 mW of power [75]. For the monolithic device, device areas of 1.00 cm^2 and 0.25 cm^2 were selected to look

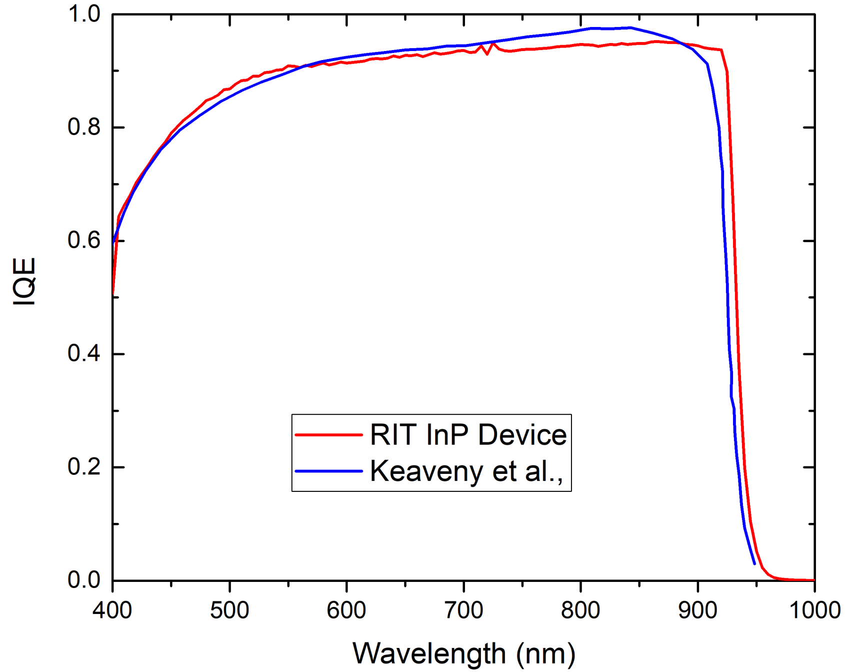

Figure 5.7: Internal quantum efficiency comparison of the best InP cell fabricated at RIT compared to the best reported literature value from Keavney *et al.,* [75]

at both higher power generation with larger PV apertures, and higher cutoff frequencies with smaller PV apertures.

5.4 p-Common Contact Development

A key layer is the common p-contact, which is shared between the InP solar cell and the EAM. For optimal solar cell performance and minimization of fractional power loss (defined by the percent of absolute power conversion efficiency lost in the solar cell) in the lateral conduction layer, this layer needs to be thick and highly doped. For optimal EAM performance, however, the goal is the minimization of free carrier absorption (FCA) and maximize transmittance. This requires a thin, lightly doped LCL. The requirements of the two devices are in tension with each other, and as a result need to be optimized.

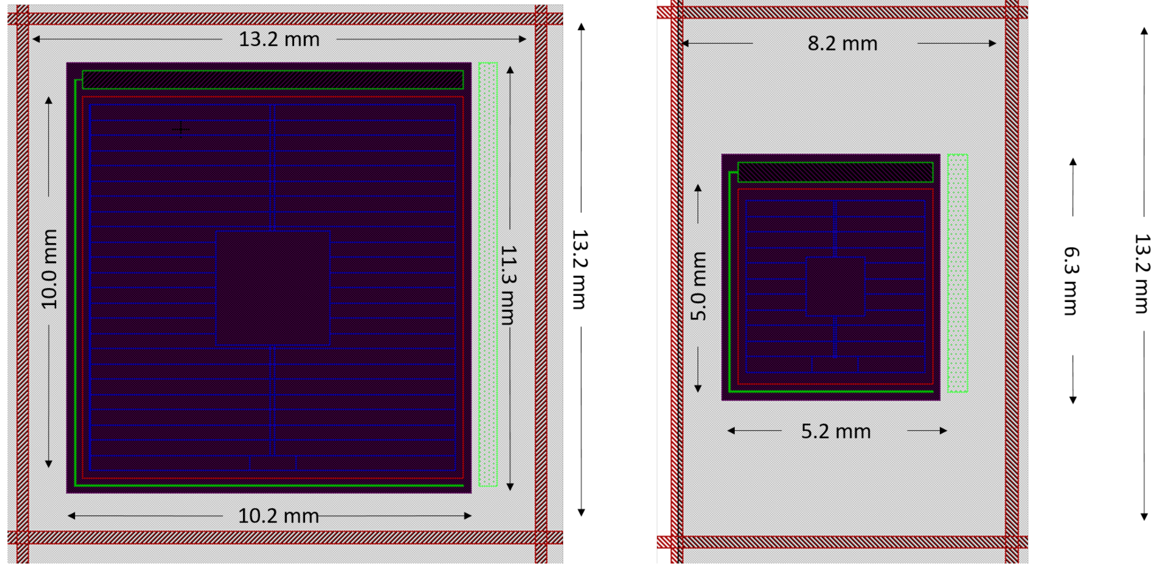

Figure 5.8: Mask design for the monolithic device with device areas of 1.00 cm^2 and 0.25 cm^2

The two materials that were considered were InP and InAlAs due to their transparency at 1550 nm. The fractional power loss in the cell was calculated assuming a 1 cm^2 cell, using the method described in Chapter 4 and Equation 4.1. To obtain good ohmic contact, a doping above 1 x 10^{19} cm^{-3} is preferred. Figure 5.9 and Figure 5.10 show the fractional power loss and two pass transmission for InP and InAlAs LCL, doped to 1 x 10^{19} cm^{-3} and 5 x 10^{19} cm^{-3}, respectively. Looking specifically in the range where fractional power loss begins to level off (between 2000 and 4000 nm) it is evident that, for equal doping levels and LCL thicknesses, InAlAs has significantly better two pass transmission, whereas InP demonstrates a slight advantage with fractional power loss, primarily driven by InP's superior hole mobility (hole mobility 45 cm^2/V-s for InP versus 7 cm^2/V-s for InAlAs, both measured via Hall Effect measurement). As a result, InAlAs is the preferred material choice for the p-common contact for the monolithic device if minimization of FCA is desired, but is power conversion efficiency in the InP solar cell

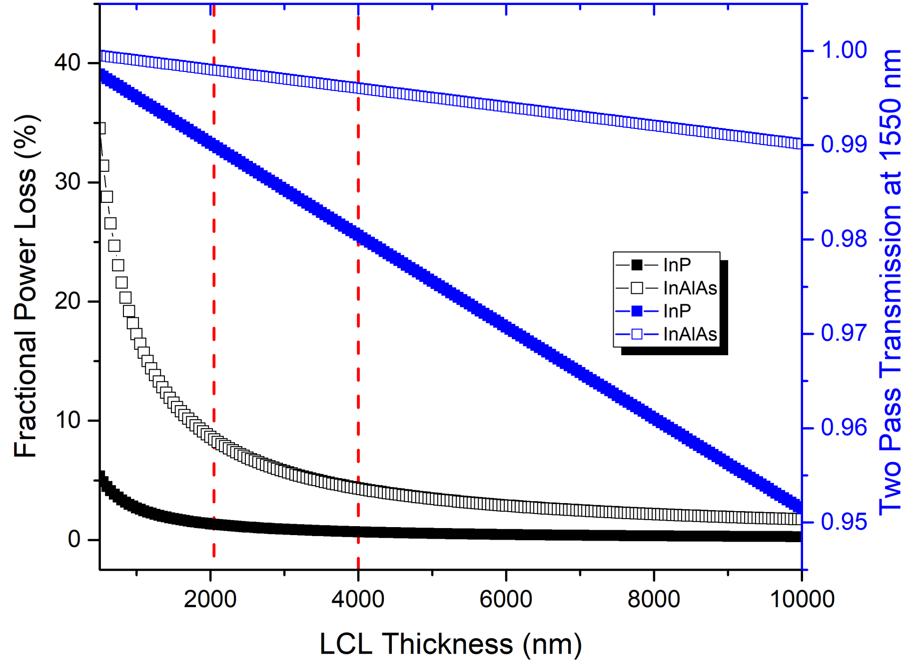

Figure 5.9: Fractional power loss and two pass transmission of an InP and InAlAs LCL layer doped to 1 x 10^{19} cm^{-3}.

is prioritized, then an InP LCL is preferred.

For the three terminal monolithically integrated device, a common contact between the InP PV device and the InGaAs/InAlAs EAM is required. This layer, however, requires careful design consideration. This layer needs to be transparent at 1550 nm to minimize parasitic absorption of the light used for data communication. For the *npn* monolithic device, p-type InP was selected as the material for this layer as it is transparent at 1550 nm.

For low series resistance and low fractional power loss in the PV device, a thick, highly doped lateral conduction layer is preferred. Fractional power loss for a lateral conduction layer can be calculated by [67], with the equation described previously in Chapter 4 (Equation 4.1). Assuming a 1.00 cm^2 device area and using the current density and voltage at the maximum power point from literature reported values for InP solar cells

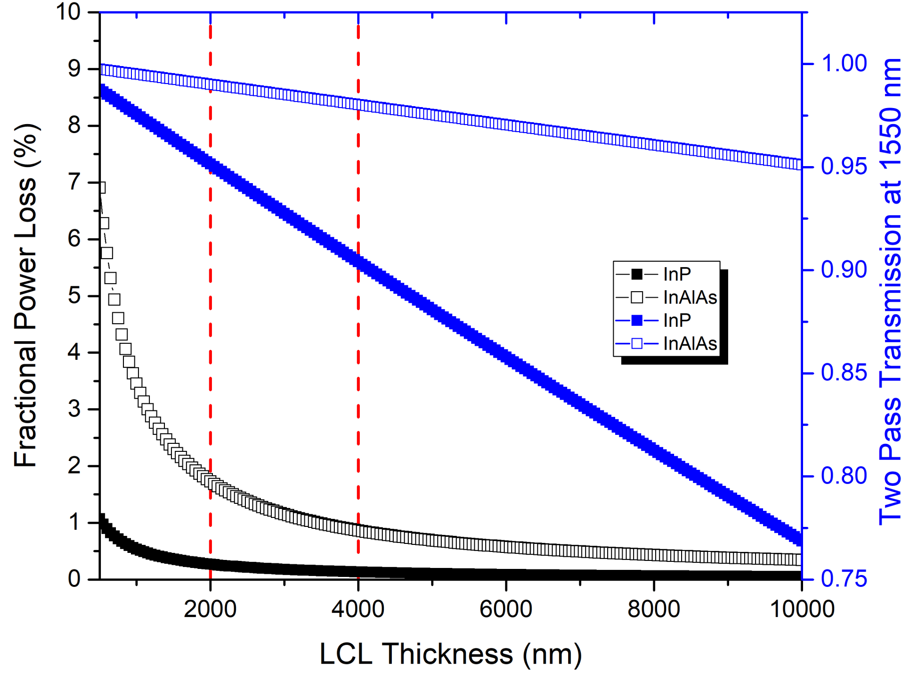

Figure 5.10: Fractional power loss and two pass transmission of an InP and InAlAs LCL layer doped to 5 x 10^{19} cm^{-3}.

measured under the AM0 spectrum [75], the doping and thickness of an LCL were varied from 2 x 10^{18} to 1 x 10^{20} cm^{-3} and from 500 nm to 10000 nm, respectively, and the FPL was calculated, as shown in Figure 5.11. Above doping concentrations of 2 x 10^{19} cm^{-3}, fractional power loss changes less than 1 % for thicker LCLs, and for LCL thicknesses above 5000 nm the doping concentration has a minimal impact on fractional power loss. To keep fractional power loss below 2 %, either the doping concentration needs to surpass 2 x 10^{19} cm^{-3}, or the LCL thickness needs to be a minimum of 5000 nm.

To minimize insertion loss at 1550 nm, that is, the signal power lost due to inherent device design, a thin, lightly doped common contact is preferred to minimize transmission loss due to free carrier absorption. Free carrier absorption as a function of layer thickness and doping has been described by Bulashevich *et al.,* [56], and the equations used have been mentioned in Chapter 3 (3.1 and 3.2).. Using the method outlined by Bulashevich

et al.,, LCL thickness and doping concentration were simulated from 2 x 10^{18} to 1 x 10^{20} cm^{-3} and from 500 nm to 10000 nm, respectively. The calculated transmission was then squared to give the transmission assuming two passes through the device (the case when integrated with a retroreflector). As both doping and LCL thickness increase, transmission loss increases due to loss via FCA. Thicknesses below 2000 nm are relatively doping concentration independent, and as the LCL becomes thicker an increase in doping concentration dependence arises. To keep transmission loss below 2 %, doping below 2 x 10^{18} cm^{-3} or a thickness of less than 800 nm is required.

To balance both the needs for the PV junction with respect to minimizing efficiency loss the need to minimize transmission loss, a 5 μm thick p-type InP LCL doped to 2 x 10^{18} was used for the monolithic device. This was designed to limit both fractional power loss in the InP PV junction and transmission loss to less than 2 %.

5.5 Monolithically Integrated Device Epitaxy and Fabrication

The monolithic device was grown using the same MOVPE reactor, wafer type, and precursors previously described for the EAM and PV growths. An illustration of the device is shown in Figure 5.14(left). For the InP PV device, a 1 x 10^{16} cm^{-3} doped 3 μm *p*-base and a 50 nm *n*-emitter with a 25 nm UID region were grown to form the junction of the InP PV cell. A 5 x 10^{19} cm^{-3} doped, 10 nm *n*-front surface field (FSF) was employed, taking advantage of the Moss-Burnstein shift [82] observed in InP to expand the bandgap

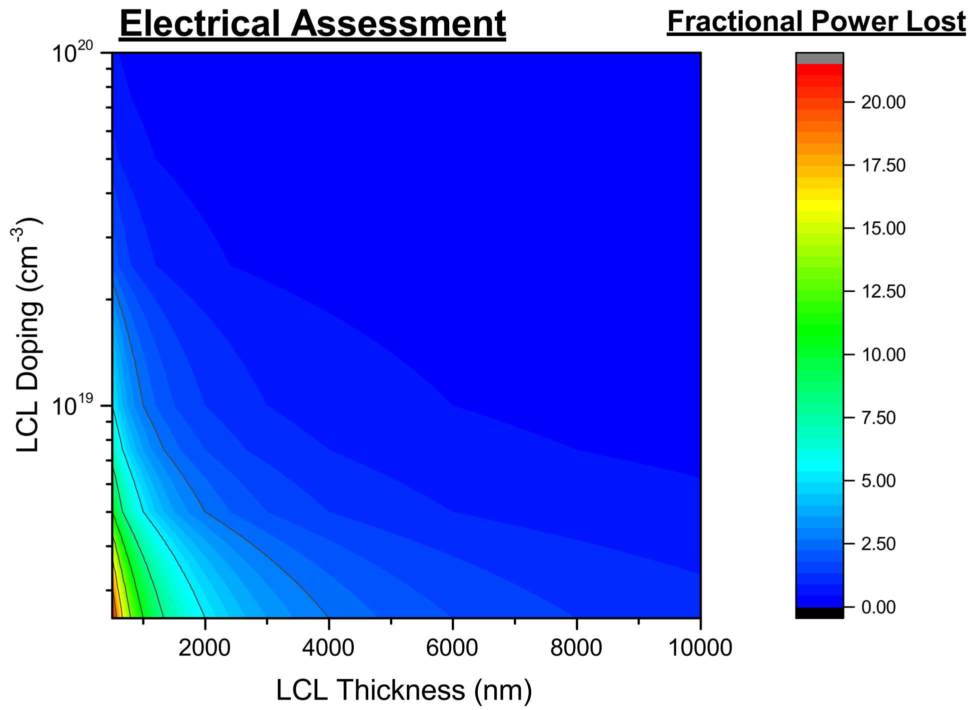

Figure 5.11: Fractional power loss in a 1.00 cm^2 InP PV device for varying LCL thicknesses and doping.

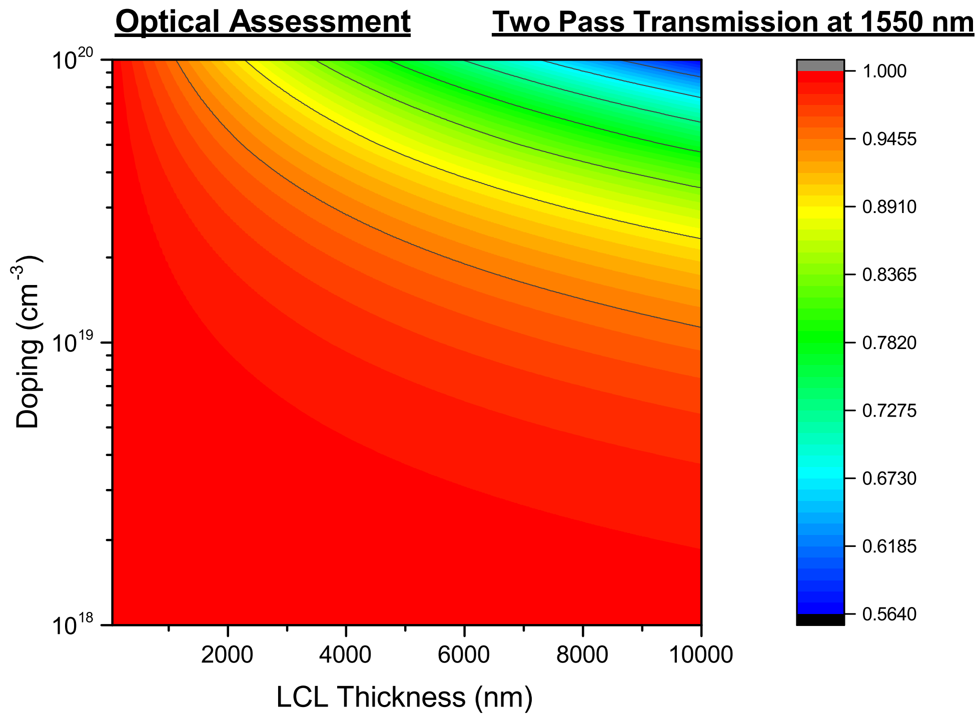

Figure 5.12: Two pass transmission at 1550 nm through a p-InP LCL varying thickness and doping.

Table 5.3: Proposed monolithic PV/EAM epitaxial layer structure.

Layer	Material	Thickness (nm)	Doping cm^{-3}	Doping Species
Solar Cell Contact	$In_{0.53}Ga_{0.47}As$	500	2 x 10^{19}	Si
Solar Cell FSF	InP	10	5 x 10^{19}	Te
Solar Cell Emitter	InP	50	1 x 10^{17}	Si
Solar Cell Base	InP	3000	5 x 10^{16}	Zn
Solar Cell Etch Stop	$In_{0.52}AlAs_{0.48}$	200	1 x 10^{18}	Zn
Common Contact	InP	5000	2 x 10^{18}	Zn
EAM Emitter	$In_{0.52}AlAs_{0.48}$	500	1 x 10^{18}	Zn
MQW Region	$In_{0.52}Al_{0.48}/In_{0.53}Ga_{0.47}As$	50 x [10/10]	UID	N/A
EAM Base	$In_{0.52}AlAs_{0.48}$	500	1 x 10^{18}	Si
EAM Contact Cap	InP	50	5 x 10^{19}	Te
EAM Contact Bulk	InP	500	6 x 10^{18}	Si

and provide front surface passivation. InGaAs doped 1 x 10^{19} cm^{-3} was used as the *n*-contact layer of the InP PV junction. Design considerations for the p-common contact have been described in the previous section. 50 nm of 1 x 10^{19} cm^{-3} p-InGaAs was used as a contact capping layer to minimize contact resistivity to the p-common contact.

For the EAM, 50 pairs of 10 nm InGaAs QWs and 10 nm InAlAs barriers were used to form the active region. *In-situ* monitoring of wafer curvature during growth returned less than 100 ppm strain in the MQW region, indicating excellent lattice matching of the QWs and barriers. The MQW region was grown between 500 nm of 1 x 10^{18} cm^{-3} doped *p* and *n* InAlAs regions to drive the built-in electric field. The *n*-contact for the EAM was 6 x 10^{18} cm^{-3} doped InP lateral conduction layer (LCL) with a thin, 7 x 10^{19} cm^{-3} doped InP contact layer.

The fabrication of a monolithic EAM/PV device is illustrated in Figure 5.14. Au was deposited on the n-InGaAs contact via electroplating to make ohmic contact to the *n*-terminal of the PV junction (Figure 5.14(a)). The InGaAs contact was then etched in 1:1:10 H_3PO_4:H_2O_2:H_2O, using the metal grid fingers as a self-aligned mask to remove the parasitically absorbing contact layer from the field of the device (Figure 5.14(b)).

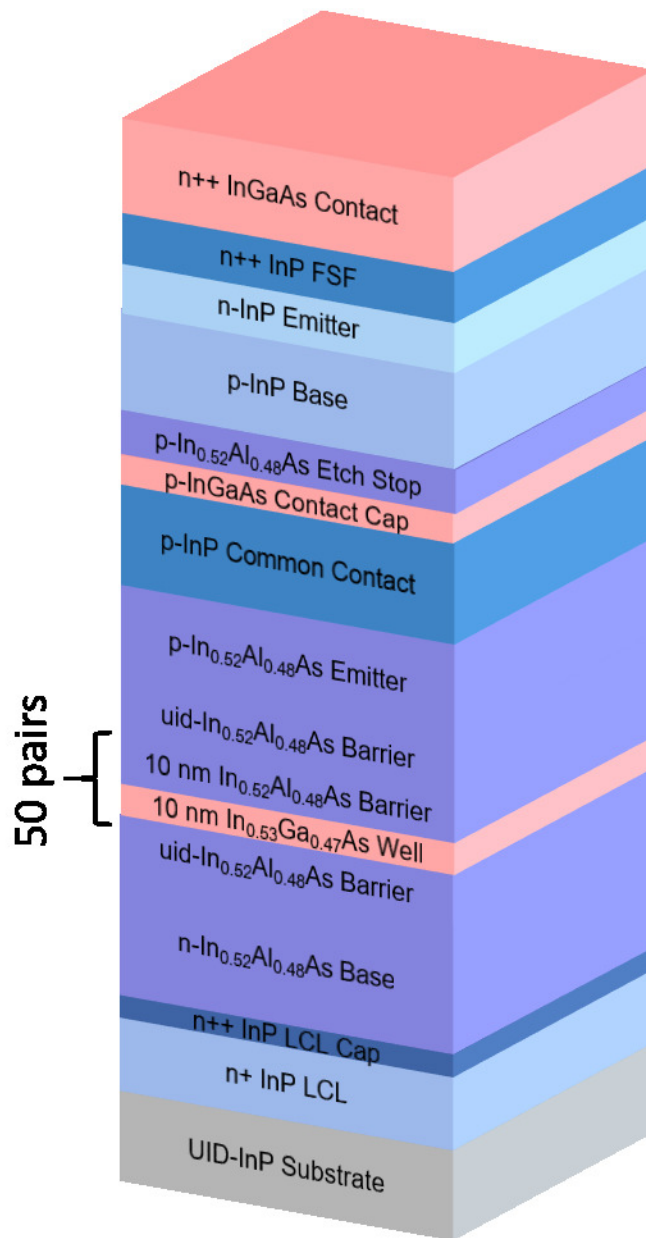

Figure 5.13: Illustration of a demonstrated epitaxial layer structure for a monolithically integrated EAM/PV device.

Next, the *np*-juncton of the InP PV device was mesa isolated in a solution of 1:1:1 HCl:H_3PO_4:CH_3COOH, which etches InP at a rate of 1.25 μm/min, and slows in the InAlAs etch stop to a rate of 162 nm/min, but does not etch the InGaAs contact cap. Then, Au was electroplated to form an ohmic contact to the p-InGaAs LCL contact cap (Figure 5.14(d)). Next, the *pn*-junction of the EAM required mesa isolation. The p-InGaAs contact cap was removed in 1:1:10 H_3PO_4:H_2O_2:H_2O, and the p-InP LCL was removed in 1:1:1 HCl:H_3PO_4:CH_3COOH, and the InAlAs p and n regions and the MQW region was etched in 1:1:10 H_3PO_4:H_2O_2:H_2O, which stops on the n-InP LCL capping layer (Figure 5.14(e)). Finally, ohmic contact was made to the n-InP LCL using a metal stack of AuGe/Au/Ni/Au, and annealing at 375 °C for 90 seconds (Figure 5.14(f)). A bilayer anti-reflection coat of zinc sulfide/magnesium fluoride was deposited via thermal evaporation to enhance absorption of the InP PV junction. A picture of the fully fabricated device under test is shown in Figure 5.15.

5.6 Discrete Junction Testing

5.6.1 InP PV Testing

After deposition of the ARC, illuminated current density-voltage measurements and quantum efficiency (QE) measurements were conducted on the InP PV junction of the monolithic device. The PV junction was tested for AM0 response as a solar cell. AM0 spectrum measurements were conducted using a two-zone TS Space Systems solar simulator calibrated with secondary standards composed of $In_{0.48}Ga_{0.52}P$ and GaAs BTJ

Figure 5.14: Fabrication procedure for a five level, monolithically integrated EAM/PV device.
a. Metal is deposited on the n-InGaAs contact.
b. The *np*-junction of the InP PV device is mesa isolated.
c. Metal is deposited on the p-InP common contact.
d. The n-InGaAs contact is etched from the field of the device.
e. The *pn*-junction of the EAM is mesa isolated.
f. Metal is deposited on the n-InP contact.

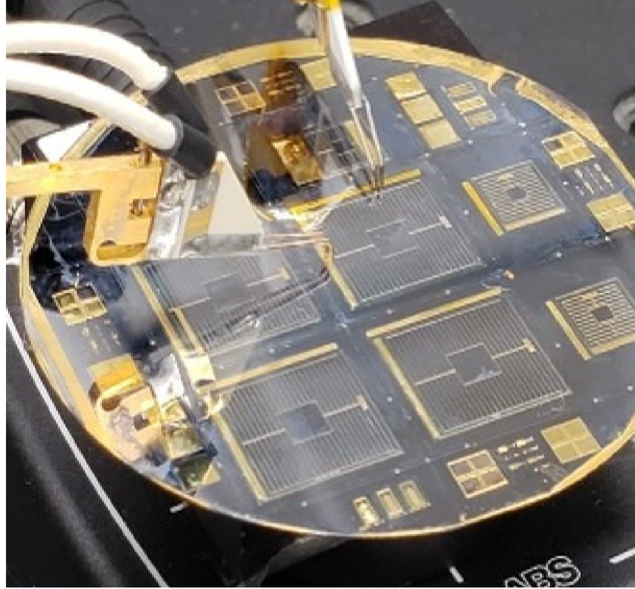

Figure 5.15: Photograph of the fully fabricated, monolithically integrated device under test.

isotypes. Devices were maintained at 23°C via a liquid cooled brass chuck. QE was measured on a Newport IQE-200 system. The system was calibrated using a Si (300-1100 nm) and Ge detector (1100-1800 nm) calibrated by Newport.

The resulting current density-voltage results for the 1.00 cm^2 area and 0.25 cm^2 area devices are shown in Figure 5.16, and the figures of merit are shown in Table 5.4. Under AM0 illumination, the open circuit voltage for the 0.25 cm^2 and 1.00 cm^2 devices were measured to be 867 and 868 mV, respectively. These are within 10 mV of the open circuit voltage reported by Keavney *et al.,* [75]. The measured short circuit current densities were found to be 31.2 mA/cm^2 and 31.6 mA/cm^2 for the 1.00 cm^2 and 0.25 cm^2 devices, respectively. This current density is lower than literature reported values of 34.9 mA/cm^2, and is due to the high reflectance measured from 400-500 nm, shown in Figure 5.17. With a better optimized ARC, collection can be recovered in this region and the EQE will better match the IQE. Based purely on current collection, this results

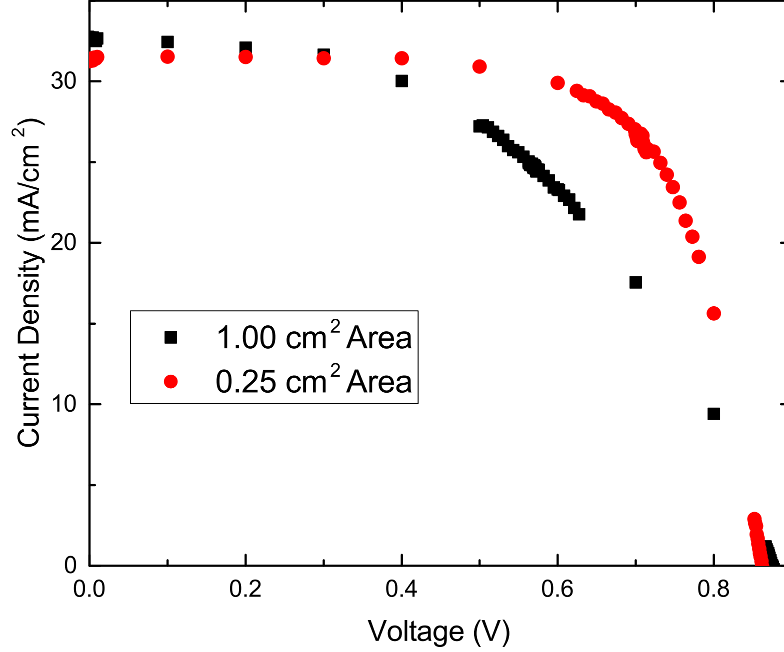

Figure 5.16: AM0 illuminated current density-voltage measurements of a 1.00 cm^2 and 0.25 cm^2 monolithic devices.

Device Area (cm^2)	V_{OC} (mV)	J_{SC} (mA/cm^2)	Fill Factor (%)	Efficiency (%)
1.00	868	31.2	60	11.2
0.25	867	31.6	70	14.1

Table 5.4: Figures of merit for the InP PV junction for AM0 and 808 nm.

in an efficiency drop of 2 %. The measured fill factor for the 1.00 cm^2 device was found to be 60 % and 70 % for the 0.25 cm^2 device. This drop in fill factor is responsible for a 3 % reduction and 5 % reduction in efficiency for the 0.25 cm^2 1.00 cm^2 and devices, respectively, more than was anticipated by the modeled results discussed previously.

5.6.2 EAM Testing

ON/OFF ratio measurements of the EAM junction were conducted in a voltage range from -2 V to -10 V, shown in Figure 5.18 using a tunable C-band (1525-1572 nm) laser. A peak ON/OFF ratio of 1.1 was observed at 1564 nm at an applied voltage of -8 V. While this value is on target for C-band operation, this peak can be further precisely

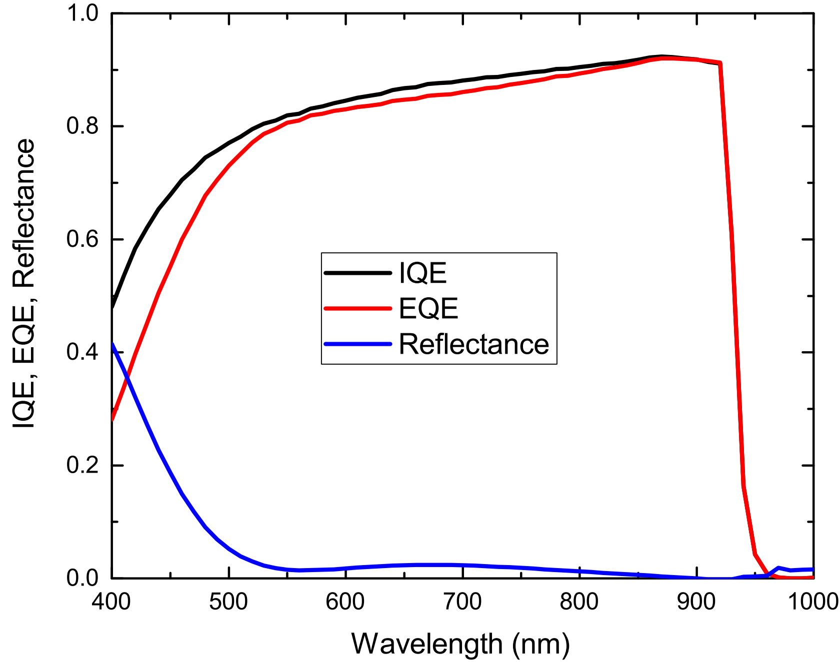

Figure 5.17: Internal and external quantum efficiency and reflectance of the InP PV junction of the monolithic device.

refined for intended 1550 nm target with slight changed to the MQW region, specifically small changes in composition to the InGaAs QW or by thinning the well to 9 nm based on results in the previous section discussing the discrete EAM development.

Cutoff frequency measurements for the EAM junction of the monolithic device for both the 120 mm^2 (PV area of 1.00 cm^2) and 35 mm^2 (PV area of 0.25 cm^2) devices were conducted. A 0 to -5 V square wave with varying frequencies was applied, and the modulated signal was measured on a ThorLabs Free Space InGaAs Adjustable Gain Photodiode (PDA20C2). To directly compare the two devices, the measured signal intensity was normalized, shown in Figure 5.19. The 120 mm^2 device demonstrated a cutoff frequency approaching 500 kHz, and the 35 mm^2 device measured a cutoff frequency approaching 1 MHz. This increase in cutoff frequency is due to a decrease in the RC time constant, driven by the capacitive component which is strongly dependent on device

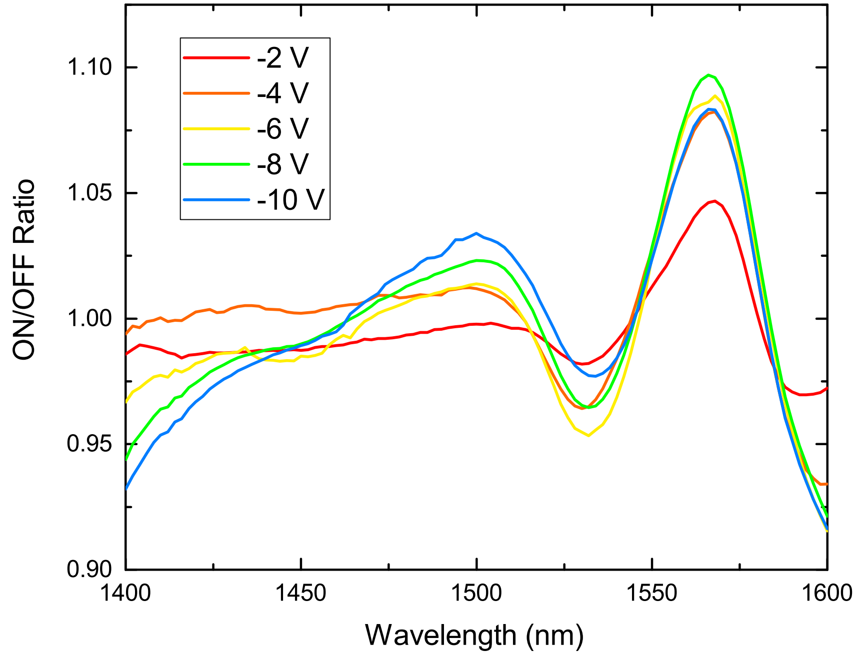

Figure 5.18: ON/OFF ratio measurements of the monolithic device, with the peak observed at 1564 nm.

area. These devices performed on target to their anticipate cutoff frequency based on the mask set design and epitaxial design. The 500 kHz cutoff frequency in the larger device corresponds to a data rate of 0.25 Mbps, and the 1 MHz cutoff frequency in the smaller device corresponds to a 0.50 Mbps data rate attainable with this design.

5.7 Simultaneous Power Generation and Data Transmission Testing

To demonstrate simultaneous power generation and data transmission, 750 nm LEDs were used to illuminate the 0.25 cm^2 monolithic device to approximately one sun power density. Use of LEDs was needed because of the limitation of the TSS Solar Simulator described previously, which does not allow for the integration of the detector required

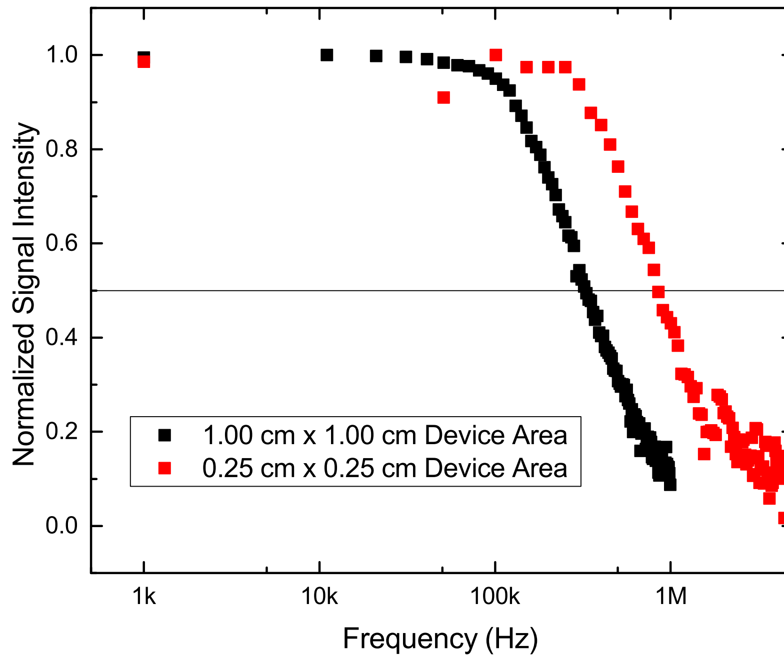

Figure 5.19: 1550 nm illuminated bandwidth measurements of the EAM junction of a 120 mm^2 area EAM and a 35 mm^2 area EAM, the 3 dB line indicated as a horizontal line. The applied voltage was 0 to -5 V with a square wave.

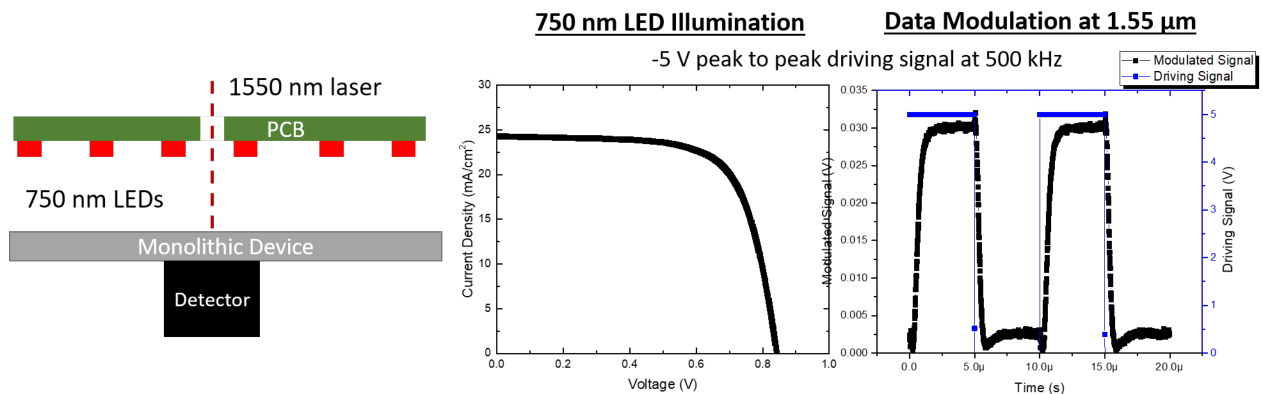

Figure 5.20: Illustration of simultaneous power generation and data communication testing (left), 750 nm LED illuminated current density-voltage curve (middle), and modulated data and driving signal (right).

for measuring 1550 nm modulated light. The LEDs were mounted on a printed circuit board (PCB), and an open aperture in the center of the PCB allowed the 1550 nm laser to pass through. LEDs were used to minimize heating effects during simultaneous PV/EAM testing. The EAM junction was driven with a 0 to -5 V square wave at 500 kHz, acting as alternating '1's and '0's. The modulated signal was then measured on the previously described InGaAs detector, with the setup illustrated in Figure5.20(left). The illuminated current density-voltage results from the 750 nm LEDs, with co-incident 1550 nm laser illumination for data modulation, is shown in Figure 5.20(center) and (right). The PV junction measured an open circuit voltage of 842 mV and a short-circuit current density of 24.29 mA/cm^2. Both of these figures of merit are lower than the 1-sun AM0 metrics described in Table 5.4 due to limitations of the 750 nm LEDs and the inability to bring the device up to 1 sun equivalent current density. The maximum power generated is 14.25 mW/cm^2. The modulated data is at a rate that is significantly lower than the cutoff frequency of the device, and as a result the modulated signal is very square, similar to the driving signal. The 500 kHz driving signal equates to a data rate of 0.25 Mbps by the Shannon-Nyquist theorem [42]. This represents the first demonstration of simultaneous power generation and data modulation for a three-terminal, monolithically integrated device.

5.8 Summary of Section

A three-terminal, monolithically integrated InP photovoltaic device with an InGaAs/InAlAs electroabsorption modulator has been designed and experimentally validated. A discrete

electroabsorption modulator was developed in order to appropriately design the quantum well region for operation near 1550 nm, and considerations regarding the effect of device area on cutoff frequency we taken. Additionally, the p-InP common contact shared by both the PV junction and the EAM junction was optimized to keep both fractional power loss and transmission loss near 2 % for a 1.00 cm^2 device. A monolithically integrated hybrid device was grown and fabricated, and the PV junction demonstrated an AM0 efficiency of 14.1 %. The EAM junction measured an ON/OFF ratio of 1.1 at 1564 nm with an applied voltage of -8 V, and a 35 mm^2 device exhibited a 3 dB cutoff frequency of 1 MHz, which correlates to a data rate of 0.5 Mbps. Simultaneous power generation using 750 nm LEDs and data modulation of 1550 nm light was demonstrated with a 500 kHz driving signal. This device has many potential applications for use in low SWaP-C satellites, debris tagging, medical applications, and high altitude, long endurance unmanned aerial systems.

Chapter 6

Conclusions

6.1 Conclusions and Outlook

6.1.1 EAM Development

Chapter 3 explored the development of surface normal EAMs for high speed operation at 1.55 μm. A fabrication procedure for a top-top design was made. The lateral conduction layer for the EAM was designed to minimize free carrier absorption and resistance, employing a two layer InP LCL that had a bulk transport region that was thicker, but more lightly doped, and a thinner, more highly doped capping layer to reduce contact resistance. The effect of device area on cutoff frequency was also investigated, demonstrating potential OOK data rates from 250 Kbps to 1 Mbps for devices ranging from 1.000 cm^2 to 0.125 cm^2. Smaller, segmented devices can push these data rates even higher. Additionally, alternative modulation schemes, such as orthogonal frequency-division multiplexing (OFDM), a more optimized modulation scheme, can increase these data rates.

For operation at 1.55 μm, the thickness of the InGaAs quantum well and InAlAs

barrier were investigated through simulation in Ansys Lumerical for their effect on the peak ON/OFF ratio location. The barrier thickness did not strongly influence the simulation results, but the thickness of the InGaAs quantum well had a large influence, and this effect was studied experimentally with quantum well thicknesses of 6, 8, and 10 nm. As the quantum well region increased in thickness, the peak ON/OFF ratio location red shifted from near 1400 nm (for a 6 nm well) to 1575 nm. Photoluminescence test structures without a *pn*-region with varied quantum well thicknesses were also grown, and the peak PL and ON/OFF ratios were compared. For peak ON/OFF ratio location at 1.55 μm in a low voltage (less than 10 V) range, a quantum well thickness of 8.5 nm would be ideal based on the growth parameters described in this dissertation.

In addition to the square quantum well design (quantum well regions with evenly spaced barriers), a coupled quantum well design was studied. With the coupled quantum well design, one barrier was made intentionally very thin (2.4 nm) to allow the wave functions from one well to overlap with another, possibly causing a larger change in transition energies, increasing the shift in the absorption coefficient observed for an equivalent voltage. Using voltage biased quantum efficiency, the shift in the observed band edge in the coupled quantum well design was nearly double what was observed in the square quantum well design. This feature is of particular interest for low voltage applications. These devices compared well to literature reported values, and further studies of the coupled well design could be fruitful.

6.1.2 Mechanically Stacked Device

Chapter 4 discussed the development of a four terminal, mechanically stacked hybrid PV/EAM device. An initial prototype using a single junction GaAs PV cell with an AM0 power conversion efficiency of 19.1 % was bonded to a 1.00 cm^2 EAM and demonstrated simultaneous data modulation and power generation. Further expanding on this design, a dual junction InGaP/GaAs PV device was designed for integration with an EAM for a 0.5 U form factor. The dual junction was designed to optimize AM0 power generation by designing the top InGaP subcell to be slightly current limiting, taking advantage of the higher fill factor attainable in the wider bandgap cell, with a potential efficiency of 24.8 %. Additionally, the lateral conduction layer of this dual junction was designed to balance fractional power loss and free carrier absorption. Using empirical models for fractional power loss and free carrier absorption, the GaAs lateral conduction layer was modeled to result in 1.5 % absolute power loss and 1.0 % transmission loss. The measured power loss was 2 % and transmission loss 4 %, with further optical modeling of all layers of the dual junction needed in order to further explain the increase transmission loss. This dual junction attained an AM0 power conversion efficiency of 22.8 %.

This dual junction was incorporated with an EAM that had a segmented design to keep the cutoff frequency above 1 MHz while still filling out a 0.5 U form factor. The EAMs were segmented into 51 mm^2 pieces, with 12 of them on the 2 inch wafer. The EAM and PV wafers were bonded together using a space grade encapsulant and then bonded to a custom printed circuit board for integration with a retroreflector and driver electronics. The EAM, while it attained a cutoff frequency of 1 MHz, had the quantum

well of the EAM designed too thin, with a peak ON/OFF ratio near 1450 nm. Simple modifications to the quantum well thickness will bring this back to 1550 nm.

6.1.3 Monolithically Integrated Device

Chapter 5 described the development of a three terminal, monolithically integrated PV/EAM device all grown on InP. Work was done to investigate the Moss-Burnstein effect in InP for use as a front surface field due to the lack of suitable materials for a window layer for an InP PV cell. Additionally, several emitter thicknesses of InP cells were grown to determine the optimal emitter thickness for an InP PV device and how that device compared to the best reported InP cells in literature.

The common contact between the InP PV cell and the EAM needed to balance fractional power loss, bandwidth reduction from resistive effects, and transmission loss. Due to the solid solubility limit of Zn in InP, the highest doping attainable is 2 x 10^{18} cm^{-3}, and to prevent severe series resistance losses in the InP PV cell, the thickness of this layer was 5 μm, which limits fractional power loss to 2 % absolute efficiency. Alternatives to needing to use a p-type LCL, which inherently has higher free carrier absorption loss and higher resistances, would be to develop a tunnel junction and use an n-type LCL.

Simultaneous power generation and data modulation was achieved using this monolithically integrated device. A possible extension of this work would be to design the InP PV cell into a multijunction laser power converter as opposed to design for AM0 operation. Use as a laser power converter would yield higher power generation, and there is interest in laser power converters combined with an EAM for technologies such as debris

tagging, medical implants, and passive sensors.

6.2 Accomplishments and Awards

6.2.1 Awards

- 50th IEEE Photovoltaics Specialist Conference Best Student Presentation Award Winner (2023)
- 49th IEEE Photovoltaics Specialist Conference Best Student Presentation Award Finalist (2022)
- Air Force Research Laboratory Summer Scholars program participant (2020 & 2021)

6.2.2 Service

- 50th IEEE Photovoltaics Specialist Conference Graduate Student Assistantship (2023)
- 49th IEEE Photovoltaics Specialist Conference Lead Graduate Student Assistantship (2023)

6.3 Curriculum Vitae

- Emily Kessler-Lewis, Stephen J. Polly, Elijah Sacchitella, Raymond Hoheisel, Seth M. Hubbard. "Demonstration of a Monolithically Integrated Hybrid Electroabsorptive Modulator/Photovoltaic Device for Bidirectional Free Space Optical Communication at 1.55 μm," *Under review in the IEEE Journal of Photovoltaics*

- Emily Kessler-Lewis, Stephen J. Polly, George T. Nelson, Michael A. Slocum, Nikhil Pokharel, Phil Ahrenkiel, Seth M. Hubbard "Development of MOVPE grown GaSb-on-GaAs interfacial misfit solar cells," *Journal of Applied Physics*, vol. 133, no. 24, p. 245002, Jun. 2023, doi: 10.1063/5.0141163.

- Emily Kessler-Lewis, Stephen J. Polly, Elijah Sacchitella, Raymond Hoheisel, and Seth M. Hubbard, "Simultaneous Solar Power Generation and Bidirectional Data Transmission," in *2023 IEEE 50th Photovoltaics Specialists Conference (PVSC)*, Jun. 2023 **Best Student Presentation Award Winner**

- Emily Kessler-Lewis, Stephen J. Polly, Elijah Sacchitella, Raymond Hoheisel, Seth M. Hubbard, "Demonstration of a Monolithically Integrated Hybrid Electroabsorptive Modulator/Photovoltaic Device for Bidirectional Free Space Optical Communication at 1.55 μm," in *2022 IEEE 49th Photovoltaics Specialists Conference (PVSC)*, Jun. 2022, pp. 0624–0624. doi: 10.1109/PVSC48317.2022.9938633. **Nominated for Best Student Presentation Award**

- Emily Kessler-Lewis, Stephen J. Polly, Seth M. Hubbard, and Raymond Hoheisel. "Design of a Hybrid Electroabsorptive Modulator/Photovoltaic Device for Free

Space Optical Communication at 1.55 μm." In *Nanoengineering: Fabrication, Properties, Optics, Thin Films, and Devices XVIII*, 11802:118020I. SPIE, 2021 https://doi.org/10.1117/12.2594704.

- Raymond Hoheisel, Emily Kessler-Lewis, Stephen J. Polly, Seth M. Hubbard, "DataCell - A Solar Cell Integrated Modulating Retroreflector," Co-talk presented at the 2020 IEEE 47th Photovoltaic Specialist Conference (PVSC), Jun. 2020.

- Stephen J. Polly, Emily Kessler-Lewis, George T. Nelson, and Seth M. Hubbard, "GaSb Solar Cells Grown by MOCVD via IMF on GaAs," in *2019 IEEE 46th Photovoltaic Specialists Conference (PVSC)*, Jun. 2019, pp. 2307–2309. doi: 10.1109/PVSC40753.2019.8981259.

- Michael A. Slocum, Alessandro Giussani, Emily Kessler, Phil Ahrenkiel, George T. Nelson, and Seth M. Hubbard, "Development of GaSb solar cells on GaAs by MOVPE via interface misfit technique," in *2017 IEEE 44th Photovoltaic Specialist Conference (PVSC)*, Jun. 2017, pp. 206–209. doi: 10.1109/PVSC.2017.8366501.

Appendix A

Modulator Testing

A.1 ON/OFF Ratio Testing

For ON/OFF ratio testing of the electroabsorption modulators, a Newport IQE200 system with a tungsten bulb was used to be the incident probe for the EAM. Chopped, monochromatic light of varied wavelength was transmitted through the EAM while the EAM was either unbiased or held at an applied voltage with a DC power supply. The transmission through the EAM was detected on a variable gain InGaAs detector (ThorLabs: PDA10CS2) and a lock-in amplifier (Stanford SR830) measured the output voltage of the detector. The measured voltage as a function of wavelength was measured on an external computer. A block diagram for the setup is shown in Figure A.1

A.2 Optical Cutoff Frequency Testing

A dedicated EAM test setup was implemented for optical cutoff frequency testing. The power density of the light from the Newport IQE200 described previously is very low,

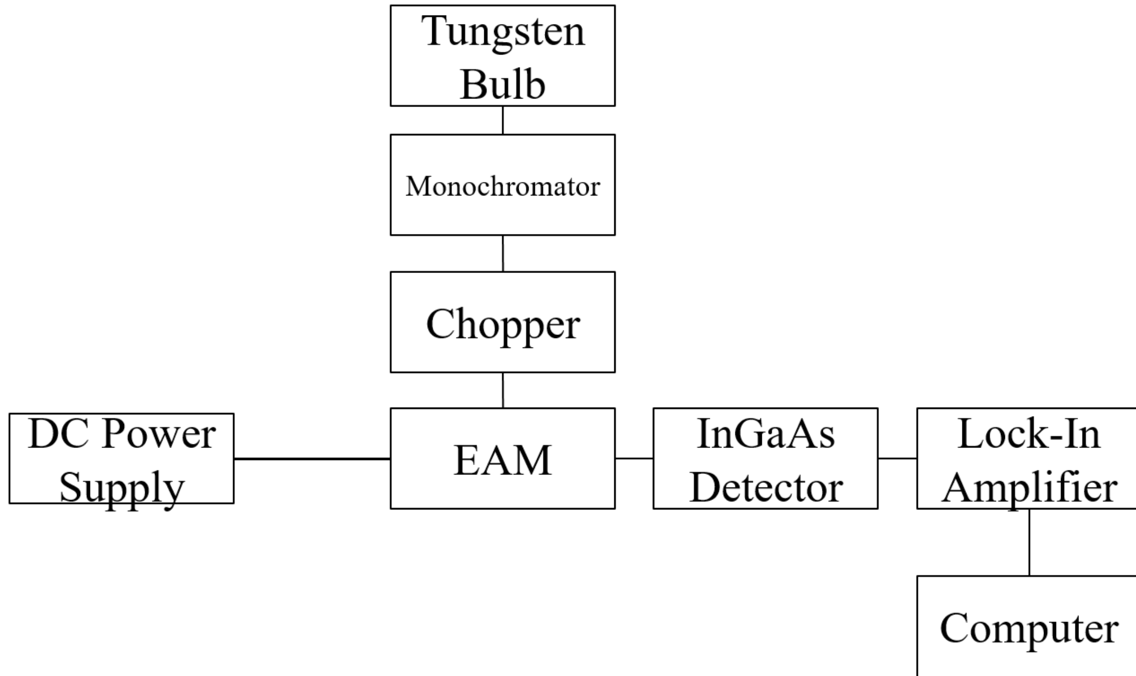

Figure A.1: Block diagram of ON/OFF ratio measurement testing.

and the InGaAs detector required a gain of 70 dB to read a signal below the noise floor. Increasing the gain quenched the bandwidth of the detector to 3 kHz. As a result, higher frequency optical measurements were not possible. To address this limitation, the light source was replaced with a 40 mW C-band tunable laser (1.525-1.572 μm range, Laser Diode Source:RLS/CBDX1-NC-FA), which passes through an adjustable collimator to focus the beam waist at a precise distance (ThorLabs: C40APC-C). The light then propagates through a linear polarizer (ThorLabs: LPIREA1-C) and a quarter wave plate (ThorLabs: WPQ10M-1550). These two components convert the unpolarized light to circularly polarized light and prevent back reflections. The power density of this light allowed a 0 dB gain setting on the InGaAs detector, which extended the bandwidth of the detector to its full capability of 11 MHz. A photograph and simplified diagram of this test setup is shown in Figure A.2.

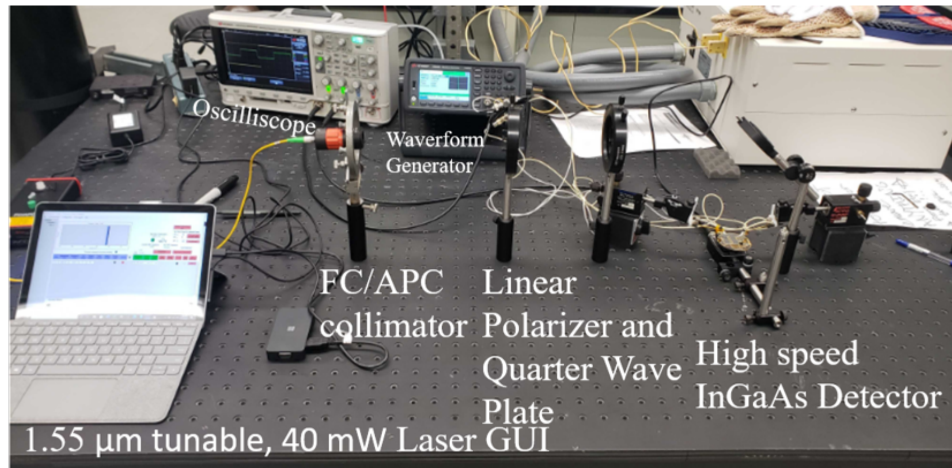

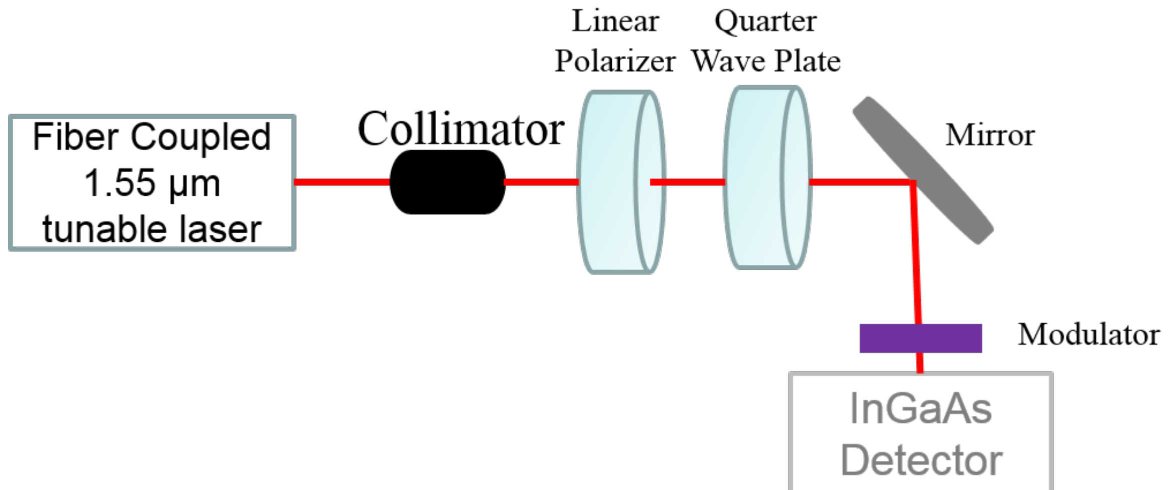

Figure A.2: Photograph (top) and simplified diagram (bottom) of the optical cutoff frequency test setup used for testing of EAMs.

References

[1] Harry W Jones. The Recent Large Reduction in Space Launch Cost. page 10, July 2018.

[2] Satellite Database | Union of Concerned Scientists.

[3] Aaron C. Boley and Michael Byers. Satellite mega-constellations create risks in Low Earth Orbit, the atmosphere and on Earth. *Scientific Reports*, 11(1):10642, May 2021. Number: 1 Publisher: Nature Publishing Group.

[4] Hank Heidt, Jordi Puig-Suari, Augustus Moore, Shinichi Nakasuka, and Robert Twiggs. CubeSat: A New Generation of Picosatellite for Education and Industry Low-Cost Space Experimentation. *Small Satellite Conference*, August 2000.

[5] John A Carr, Les Johnson, Darren Boyd, Brandon Phillips, Miria Finckenor, Brandon Farmer, and Joseph C Smith. The Lightweight Integrated Solar Array and anTenna: 3rd Generation Advancements, and Beyond. page 33.

[6] John A. Carr, Darren Boyd, Armando Martinez, Michael SanSoucie, Les Johnson, Greg Laue, Brandon Farmer, Joseph C. Smith, Barrett Robertson, and Mark Johnson. The Lightweight Integrated Solar Array and Transceiver (LISA-T): Second Generation Advancements and the Future of SmallSat Power Generation. August 2016.

[7] NASA Technology Roadmaps - TA 5: Communications, Navigation, and Orbital Debris Tracking and Characterization Systems. page 130, 2015.

[8] Zabih Ghassemlooy, Shlomi Arnon, Murat Uysal, Zhengyuan Xu, and Julian Cheng. Emerging Optical Wireless Communications-Advances and Challenges. *IEEE Journal on Selected Areas in Communications*, 33(9):1738–1749, September 2015. Conference Name: IEEE Journal on Selected Areas in Communications.

[9] W Dan Williams, Michael Collins, Don M Boroson, James Lesh, Abihijit Biswas, Richard Orr, Leonard Schuchman, and Satel Llc. RF and Optical Communications: A Comparison of High Data Rate Returns From Deep Space in the 2020 Timeframe. 2020.

[10] Hemani Kaushal and Georges Kaddoum. Optical Communication in Space: Challenges and Mitigation Techniques. *IEEE Communications Surveys Tutorials*, 19(1):57–96, 2017.

[11] Rayan Alsemmeari, Sheikh Bakhsh, and Hani Alsemmeari. Free Space Optics Vs Radio Frequency Wireless Communication. *International Journal of Information Technology and Computer Science*, 8:1–8, September 2016.

[12] Zdeněk Kolka, Zdeněk Kincl, Viera Biolkova, and Dalibor Biolek. Hybrid FSO/RF test link. In *2012 IV International Congress on Ultra Modern Telecommunications and Control Systems*, pages 502–505, October 2012. ISSN: 2157-023X.

[13] Hany Elgala, Raed Mesleh, and Harald Haas. Indoor optical wireless communication: potential and state-of-the-art. *IEEE Communications Magazine*, 49(9):56–62, September 2011. Conference Name: IEEE Communications Magazine.

[14] H. Helmers, D. Lackner, G. Siefer, E. Oliva, F. Dimroth, and A.W. Bett. Integrated Power and Data Transceiver Devices for Power-by-Light Systems – a Concept Study. *32nd European Photovoltaic Solar Energy Conference and Exhibition; 218-222*, pages 5 pages, 1935 kb, 2016. Artwork Size: 5 pages, 1935 kb Medium: application/pdf Publisher: WIP.

[15] Zixiong Wang, Dobroslav Tsonev, Stefan Videv, and Harald Haas. On the Design of a Solar-Panel Receiver for Optical Wireless Communications With Simultaneous Energy Harvesting. *IEEE Journal on Selected Areas in Communications*, 33(8):1612–1623, August 2015. Conference Name: IEEE Journal on Selected Areas in Communications.

[16] John Fakidis, Stefan Videv, Stepan Kucera, Holger Claussen, and Harald Haas. Indoor Optical Wireless Power Transfer to Small Cells at Nighttime. *Journal of Lightwave Technology*, 34(13):3236–3258, July 2016. Conference Name: Journal of Lightwave Technology.

[17] Sung-Man Kim, Ji-San Won, and Seung-Hoon Nahm. Simultaneous reception of solar power and visible light communication using a solar cell. *Optical Engineering*, 53(4):046103, April 2014. Publisher: SPIE.

[18] Dong-Soo Shin, Paul K. L. Yu, and S. A. Pappert. High-power electroabsorption modulator using intra-step-barrier quantum wells. *Journal of Applied Physics*, 89(2):1515–1517, January 2001.

[19] Shuyu Zhang, Dobroslav Tsonev, Stefan Videv, Sanjay Ghosh, Graham A. Turnbull, Ifor D. W. Samuel, and Harald Haas. Organic solar cells as high-speed data detectors for visible light communication. *Optica*, 2(7):607–610, July 2015. Publisher: Optica Publishing Group.

[20] John Fakidis, Stefan Videv, Henning Helmers, and Harald Haas. 0.5-Gb/s OFDM-Based Laser Data and Power Transfer using a GaAs Photovoltaic Cell. In *2018 IEEE Photonics Conference (IPC)*, pages 1–4, September 2018. ISSN: 2575-274X.

[21] J. F. Geisz, Sarah Kurtz, M. W. Wanlass, J. S. Ward, A. Duda, D. J. Friedman, J. M. Olson, W. E. McMahon, T. E. Moriarty, and J. T. Kiehl. High-efficiency GaInPGaAsInGaAs triple-junction solar cells grown inverted with a metamorphic bottom junction. *Applied Physics Letters*, 91(2):023502, July 2007.

[22] Jenny A. Nelson. *The Physics Of Solar Cells*. World Scientific Publishing Company, May 2003. Google-Books-ID: 4Ok7DQAAQBAJ.

[23] Martin A. Green, Ewan D. Dunlop, Masahiro Yoshita, Nikos Kopidakis, Karsten Bothe, Gerald Siefer, and Xiaojing Hao. Solar cell efficiency tables (version 62). *Progress in Photovoltaics: Research and Applications*, 31(7):651–663, 2023. _eprint: https://onlinelibrary.wiley.com/doi/pdf/10.1002/pip.3726.

[24] William Shockley and Hans J. Queisser. Detailed Balance Limit of Efficiency of p-n Junction Solar Cells. *Journal of Applied Physics*, 32(3):510–519, March 1961. Publisher: American Institute of Physics.

[25] Sven Rühle. Tabulated values of the Shockley–Queisser limit for single junction solar cells. *Solar Energy*, 130:139–147, June 2016.

[26] Ryan M. France, John F. Geisz, Tao Song, Waldo Olavarria, Michelle Young, Alan Kibbler, and Myles A. Steiner. Triple-junction solar cells with 39.5% terrestrial and 34.2% space efficiency enabled by thick quantum well superlattices. *Joule*, 6(5):1121–1135, May 2022.

[27] R.R. King, C.M. Fetzer, P.C. Colter, K.M. Edmondson, D.C. Law, A.P. Stavrides, H. Yoon, G.S. Kinsey, H.L. Cotal, J.H. Ermer, R.A. Sherif, K. Emery, W. Metzger, R.K. Ahrenkiel, and N.H. Karam. Lattice-matched and metamorphic GaInP/GaInAs/Ge concentrator solar cells. In *Proceedings of 3rd World Conference onPhotovoltaic Energy Conversion, 2003*, volume 1, pages 622–625 Vol.1, May 2003.

[28] R.R. King, C.M. Fetzer, P.C. Colter, K.M. Edmondson, J.H. Ermer, H.L. Cotal, Hojun Yoon, A.P. Stavrides, G. Kinsey, D.D. Krut, and N.H. Karam. High-efficiency space and terrestrial multijunction solar cells through bandgap control in cell structures. In *Conference Record of the Twenty-Ninth IEEE Photovoltaic Specialists Conference, 2002.*, pages 776–781, May 2002. ISSN: 1060-8371.

[29] Sarah R Kurtz, D Myers, and J M Olson. PROJECTED PERFORMANCE OF THREE- AND FOUR-JUNCTION DEVICES USING.

[30] Stephen Saltsman. The Silicon Solar Cell as an Optical Detector. *Retrospective Theses and Dissertations*, January 1977.

[31] Walter D. Leon-Salas and Xiaozhe Fan. Exploiting Luminescence Emissions of Solar Cells for Optical Frequency Identification (OFID). In *2018 IEEE International Symposium on Circuits and Systems (ISCAS)*, pages 1–5, May 2018. ISSN: 2379-447X.

[32] Walter Daniel Leon-Salas and Xiaozhe Fan. Solar Cell Photo-Luminescence Modulation for Optical Frequency Identification Devices. *IEEE Transactions on Circuits and Systems I: Regular Papers*, 66(5):1981–1992, May 2019. Conference Name: IEEE Transactions on Circuits and Systems I: Regular Papers.

[33] Walter D. Leon-Salas, Xiaozhe Fan, Miguel Vizcardo, and Mauricio Postigo-Malaga. A Solar Cell Photo-Luminescence Modulator for Optical Communications. *IEEE Transactions on Circuits and Systems II: Express Briefs*, 69(6):2757–2761, June 2022. Conference Name: IEEE Transactions on Circuits and Systems II: Express Briefs.

[34] F. Pockels. *Lehrbuch der Kristalloptik.* January 1906. Publication Title: B.G. Teubner Lehrbuecher der mathematischen Wissenschaften ADS Bibcode: 1906lekr.book.....P.

[35] Dr Rüdiger Paschotta. Pockels Effect.

[36] Qianfan Xu, Bradley Schmidt, Sameer Pradhan, and Michal Lipson. Micrometre-scale silicon electro-optic modulator. *Nature*, 435(7040):325–327, May 2005. Number: 7040 Publisher: Nature Publishing Group.

[37] José Mora, Beatriz Ortega, Antonio Díez, José Luis Cruz, Miguel V. Andrés, José Capmany, and Daniel Pastor. Photonic Microwave Tunable Single-Bandpass Filter Based on a Mach-Zehnder Interferometer. *Journal of Lightwave Technology*, 24(7):2500, July 2006. Publisher: IEEE.

[38] Walter Franz. Einfluß eines elektrischen Feldes auf eine optische Absorptionskante. *Zeitschrift für Naturforschung A*, 13(6):484–489, June 1958. Publisher: De Gruyter.

[39] D. A. B. Miller, D. S. Chemla, T. C. Damen, A. C. Gossard, W. Wiegmann, T. H. Wood, and C. A. Burrus. Band-Edge Electroabsorption in Quantum Well Structures: The Quantum-Confined Stark Effect. *Physical Review Letters*, 53(22):2173–2176, November 1984. Publisher: American Physical Society.

[40] R. Schwedler, H. Mikkelsen, K. Wolter, D. Laschet, J. Hergeth, and H. Kurz. InGaAs/InP multiple quantum well modulators in experiment and theory. *Journal de Physique III*, 4(12):2341–2359, 1994. Publisher: EDP Sciences.

[41] T.H. Wood. Multiple quantum well (MQW) waveguide modulators. *Journal of Lightwave Technology*, 6(6):743–757, June 1988. Conference Name: Journal of Lightwave Technology.

[42] C.E. Shannon. Communication in the Presence of Noise. *Proceedings of the IRE*, 37(1):10–21, January 1949. Conference Name: Proceedings of the IRE.

[43] H.C. Neitzert, C. Cacciatore, D. Campi, C. Rigo, C. Coriasso, and A. Stano. InGaAs-InP superlattice electroabsorption waveguide modulator. *IEEE Photonics Technology Letters*, 7(8):875–877, August 1995. Conference Name: IEEE Photonics Technology Letters.

[44] K. Yoshino, K. Wakita, I. Kotaka, S. Kondo, Y. Noguchi, S. Kuwano, N. Takachio, T. Otsuji, Y. Imai, and T. Enoki. 40-Gbit/s operation of InGaAs/InAlAs MQW electroabsorption modulator module with very low driving-voltage. In *Proceedings of European Conference on Optical Communication*, volume 3, pages 203–206 vol.3, September 1996.

[45] Dazeng Feng, Shirong Liao, Hong Liang, Joan Fong, Bhavin Bijlani, Roshanak Shafiiha, B. Jonathan Luff, Ying Luo, Jack Cunningham, Ashok V. Krishnamoorthy, and Mehdi Asghari. High speed GeSi electro-absorption modulator at 1550 nm wavelength on SOI waveguide. *Optics Express*, 20(20):22224–22232, September 2012. Publisher: Optical Society of America.

[46] K. Wakita, I. Kotaka, H. Asai, S. Nojima, and O. Mikami. High-efficiency electroabsorption in quaternary AlGaInAs quantum-well optical modulators. *Electronics Letters*, 24(21):1324–1325, 1988. Publisher: IEE.

[47] T. Ido, H. Sano, D.J. Moss, S. Tanaka, and A. Takai. Strained InGaAs/InAlAs MQW electroabsorption modulators with large bandwidth and low driving voltage.

IEEE Photonics Technology Letters, 6(10):1207–1209, October 1994. Conference Name: IEEE Photonics Technology Letters.

[48] Peter G. Goetz, Rita Mahon, Todd H. Stievater, William S. Rabinovich, and Steven C. Binari. High-speed large-area surface-normal multiple quantum well modulators. In *Free-Space Laser Communication and Active Laser Illumination III*, volume 5160, pages 346–354. International Society for Optics and Photonics, January 2004.

[49] D.R.P. Guy, D.D. Besgrove, L.L. Taylor, N. Apsley, and S.J. Bass. InGaAs-InP MQW electro-absorption modulators. In *IEE Colloquium on Heterojunction and Quantym Well Devices: Physics, Engineering and Applications*, pages 5/1–5/4, October 1988.

[50] H. Mohseni, W. K. Chan, H. An, A. Ulmer, and D. Capewell. High-performance surface-normal modulators based on stepped quantum wells. In *Enabling Photonics Technologies for Defense, Security, and Aerospace Applications*, volume 5814, pages 191–198. International Society for Optics and Photonics, May 2005.

[51] R. N. Pathak, K. W. Goossen, J. E. Cunningham, and W. Y. Jan. InGaAs-InP P-I (MQW)-N surface-normal electroabsorption modulators exhibiting better than 8:1 contrast ratio for 1.55-m applications grown by gas-source MBE. *IEEE Photonics Technology Letters*, 6(12):1439–1441, December 1994. Conference Name: IEEE Photonics Technology Letters.

[52] T. H. Stievater, W. S. Rabinovich, P. G. Goetz, R. Mahon, and S. C. Binari. A surface-normal coupled-quantum-well modulator at 1.55 m. *IEEE Photonics Technology Letters*, 16(9):2036–2038, September 2004. Conference Name: IEEE Photonics Technology Letters.

[53] Jean Decobert and Gilles Patriarche. Transmission electron microscopy study of the InP/InGaAs and InGaAs/InP heterointerfaces grown by metalorganic vapor-phase epitaxy. *Journal of Applied Physics*, 92(10):5749–5755, October 2002. Publisher: American Institute of Physics.

[54] A.R Clawson. Guide to references on III–V semiconductor chemical etching. *Materials Science and Engineering: R: Reports*, 31(1-6):1–438, January 2001.

[55] F. G. Kellert, K. T. Chan, J. E. Turner, and V. M. Robbins. Tellurium induced lattice dilation in OMVPE grown InP. *Journal of Electronic Materials*, 19(12):1425–1428, December 1990.

[56] K. A. Bulashevich, V. F. Mymrin, S. Yu Karpov, D. M. Demidov, and A. L. Ter-Martirosyan. Effect of free-carrier absorption on performance of 808 nm AlGaAs-based high-power laser diodes. *Semiconductor Science and Technology*, 22(5):502–510, March 2007. Publisher: IOP Publishing.

[57] J. W. Matthews and A. E. Blakeslee. Defects in epitaxial multilayers: I. Misfit dislocations. *Journal of Crystal Growth*, 27:118–125, December 1974.

[58] David J. Israel, Bernard L. Edwards, Richard L. Butler, John D. Moores, Sabino Piazzolla, Nic du Toit, and Lena Braatz. Early results from NASA's laser communications relay demonstration (LCRD) experiment program. In *Free-Space Laser Communications XXXV*, volume 12413, pages 10–24. SPIE, March 2023.

[59] R. J. Walters, M. González, J. G. Tischler, M. P. Lumb, J. R. Meyer, I. Vurgaftman, J. Abell, M. K. Yakes, N. Ekins-Daukes, J G. J. Adams, N. Chan, P. Stavrinou, and P. P. Jenkins. Design of an achievable, all lattice-matched multijunction solar cell using InGaAlAsSb. In *2011 37th IEEE Photovoltaic Specialists Conference*, pages 000122–000126, June 2011. ISSN: 0160-8371.

[60] Marina S. Leite, Robyn L. Woo, William D. Hong, Daniel C. Law, and Harry A. Atwater. Wide-band-gap InAlAs solar cell for an alternative multijunction approach. *Applied Physics Letters*, 98(9):093502, February 2011.

[61] Robyn L. Woo, William D. Hong, Shoghig Mesropian, Marina S. Leite, Harry A. Atwater, and Daniel C. Law. First demonstration of monolithic InP-based InAlAs/InGaAsP/InGaAs triple junction solar cells. In *2011 37th IEEE Photovoltaic Specialists Conference*, pages 000295–000298, June 2011. ISSN: 0160-8371.

[62] Matthew P. Lumb, Maria Gonzalez, Igor Vurgaftman, Jerry R. Meyer, Joshua Abell, Michael Yakes, Raymond Hoheisel, Joseph G. Tischler, Phillip P. Jenkins, Paul N. Stavrinou, Markus Fuhrer, Ned J. Ekins-Daukes, and Robert J. Walters. Simulation of novel InAlAsSb solar cells. In *Physics, Simulation, and Photonic Engineering of Photovoltaic Devices*, volume 8256, pages 136–148. SPIE, February 2012.

[63] Brittany L. Smith, Zachary S. Bittner, Staffan D. Hellstroem, George T. Nelson, Michael A. Slocum, Andrew G. Norman, David V. Forbes, and Seth M. Hubbard. InAlAs photovoltaic cell design for high device efficiency. *Progress in Photovoltaics: Research and Applications*, 25(8):706–713, 2017. _eprint: https://onlinelibrary.wiley.com/doi/pdf/10.1002/pip.2895.

[64] Michael Slocum, David V. Forbes, Glen C. Hillier, Brittany L. Smith, Jessica G. J. Adams, and Seth M. Hubbard. Development of InAlAsSb growth by MOVPE. *Journal of Crystal Growth*, 471:15–20, August 2017.

[65] Martin A. Green. *Solar Cells : Operating Principles, Technology and System Applications*. University of New South Wales, Kensington, NSW, January 1986.

[66] Stephen Polly, Brandon Bogner, Anastasiia Fedorenko, Nikhil Pokharel, Phil Ahrenkiel, Subhra Chowdhury, Dhrubes Biswas, and Seth Hubbard. Growth optimization of quantum-well-enhanced multijunction photovoltaics. *Cell Reports Physical Science*, 4(6):101432, June 2023.

[67] Martin A. Green. Solar cell fill factors: General graph and empirical expressions. *Solid-State Electronics*, 24(8):788–789, August 1981.

[68] HJ Hovel. The effect of depletion region recombination currents on the efficiencies of Si and GaAs solar cells. *Photovoltaic Specialists Conference*, 10 th, Palo Alto, Calif:34–39, 1974. 29.

[69] Masafumi Yamaguchi, Chikao Uemura, and Akio Yamamoto. Radiation damage in InP single crystals and solar cells. *Journal of Applied Physics*, 55(6):1429–1436, March 1984.

[70] Masafumi Yamaguchi and Koushi Ando. Mechanism for radiation resistance of InP solar cells. *Journal of Applied Physics*, 63(11):5555–5562, June 1988.

[71] Masafumi Yamaguchi. Effects of irradiation temperature on radiation damage in InP solar cells. *Journal of Applied Physics*, 77(8):3679–3683, April 1995.

[72] Koushi Ando and Masafumi Yamaguchi. Radiation resistance of InP solar cells under light illumination. *Applied Physics Letters*, 47(8):846–848, October 1985.

[73] R.J. Walters. A review of radiation effects in InP solar cells. In *Proceedings of 1994 IEEE 6th International Conference on Indium Phosphide and Related Materials (IPRM)*, pages 275–279, March 1994.

[74] Robert J. Walters, S. R. Messenger, G. P. Summers, M. J. Romero, M. M. Al-Jassim, D. Araújo, and R. Garcia. Radiation response of n -type base InP solar cells. *Journal of Applied Physics*, 90(7):3558–3565, October 2001.

[75] C.J. Keavney, V.E. Haven, and S.M. Vernon. Emitter structures in MOCVD InP solar cells. In *IEEE Conference on Photovoltaic Specialists*, pages 141–144 vol.1, May 1990. ISSN: null.

[76] Mark Wanlass. Systems and methods for advanced ultra-high-performance InP solar cells, July 2018.

[77] R.K. Jain and G.A. Landis. Effect of InAlAs window layer on the efficiency of indium phosphide solar cells. In *The Conference Record of the Twenty-Second IEEE Photovoltaic Specialists Conference - 1991*, pages 341–346, Las Vegas, NV, USA, 1991. IEEE.

[78] J. Lammasniemi, K. Tappura, and K. Smekalin. Recombination mechanisms at window/emitter interface in InP and other III-V semiconductor based solar cells. In *Proceedings of 1994 IEEE 1st World Conference on Photovoltaic Energy Conversion - WCPEC (A Joint Conference of PVSC, PVSEC and PSEC)*, volume 2, pages 1771–1774 vol.2, December 1994.

[79] J. Lammasniemi, K. Tappura, and K. Smekalin. High interface recombination velocity caused by spatially indirect quantum well transition in Al $_{0.55}$ In $_{0.45}$ As/InP heteroface solar cells. *Journal of Applied Physics*, 77(9):4801–4803, May 1995.

[80] M. B. Spitzer, C. J. Keavney, S. M. Vernon, and V. E. Haven. Indium phosphide shallow homojunction solar cells made by metalorganic chemical vapor deposition. *Applied Physics Letters*, 51(5):364–366, August 1987.

[81] M W Wanlass, T A Gessert, K A Emery, and T J Coutts. An Empirical Study of the Performance of APMOVPE AM0 InP Homojunction Solar Cells as a Function of Emitter Thickness and Doping, and Base Doping. page 17.

[82] T. S. Moss. The Interpretation of the Properties of Indium Antimonide. 67(10):775–782, October 1954. Publisher: IOP Publishing.

[83] Elias Burstein. Anomalous Optical Absorption Limit in InSb. *Physical Review*, 93(3):632–633, February 1954. Publisher: American Physical Society.